Non-Equilibrium Dynamics with Quantum Monte Carlo

by

Qiaoyuan Dong

A dissertation submitted in partial fulfillment
of the requirements for the degree of
Doctor of Philosophy
(Physics and Scientific Computing)
in the University of Michigan
2017

Doctoral Committee:

Assistant Professor Emanuel Gull, Chair
Professor Eitan Geva
Associate Professor Lu Li
Professor Roberto D. Merlin
Assistant Professor Kai Sun

Qiaoyuan Dong

dongqy@umich.edu

ORCID iD: 0000-0002-8296-1977

To my parents.

Acknowledgements

First and foremost I would like to express my sincere gratitude to my advisor Prof. Emanuel Gull. He was always keen to know how I was doing and frequently asked if I had any questions. The door to Prof. Gull's office was always open whenever I ran into a trouble spot. He was always more than patient to guide me through and helped me to overcome numerous obstacles I have been facing during the past five years. His continuing support helped me in all the time of research and writing of this thesis.

The members of the Gull group have contributed immensely to my personal and professional time at Michigan. The group has been a source of friendships as well as good advice and collaboration. From our research group, a very special gratitude goes out to Dr. Andrey Antipov. Upon myself joining the group as a fresh graduate student, he has been the most instrumental in helping me advance through the various difficulties that I have encountered and taught how good theoretical physics is done. I miss the sleepless nights we were working together before deadlines, and all the fun we have had during that time. Without his guidance, patience and encouragement, this work would not have happened, especially during tough times in the Ph.D. pursuit. I would also like to acknowledge Dr. Igor Krivenko as the second reader of this thesis, and I am gratefully indebted to him for his very valuable comments on this thesis. His scrupulous attention to detail was contagious and motivational, and will remain as a beneficent influence on the rest of my life. In addition, the discussions I had with Dr. James LeBlanc, Dr. Hanna Terletska, Dr. Sergei Iskakov and Dr. Markus Wallerberger during the last four years have been extremely helpful and fruitful. I am also grateful to Dr. Alexander Gaenko who provided the whole group with help regarding to computing questions and kept us organized in terms of coding resources. There is also my collaboration with Joseph Kleinhenz. He has contributed a very tangible mark on this work and I am grateful for his patience when I had questions regarding to writing. Last but not the least, I appreciate my fellow graduate students of the group, Xi Chen, Joseph Paki and Jia Li for the stimulating discussions and their companionship.

iii

Abstract

This work is motivated by the fact that the investigation of non-equilibrium phenomena in strongly correlated electron systems has developed into one of the most active and exciting branches of condensed matter physics as it provides rich new insights that could not be obtained from the study of equilibrium situations. However, a theoretical description of those phenomena is missing. Therefore, in this thesis, we develop a numerical method that can be used to study two minimal models – the Hubbard model and the Anderson impurity model with general parameter range and time dependence.

We begin by introducing the theoretical framework and the general features of the Hubbard model. We then describe the dynamical mean field theory (DMFT), which was first invented by Georges *et al* [1] in 1992. It provides a feasible way to approach strongly correlated electron systems and reduces the complexity of the calculations via a mapping of lattice models onto quantum impurity models subject to a self-consistency condition. We employ the non-equilibrium extension of DMFT and map the Hubbard model to the single impurity Anderson model (SIAM).

Since the fundamental component of the DMFT method is a solver of the single impurity Anderson model, we continue with a description of the formalism to study the real-time dynamics of the impurity model staring at its thermal equilibrium state. We utilize the non-equilibrium strong-coupling perturbation theory and derive semi-analytical approximation methods such as the non-crossing approximation (NCA) and the one-crossing approximation (OCA). We then use the Quantum Monte-Carlo method (QMC) as a numerically exact method and present proper measurements of local observables, current and Green's functions. We perform simulations of the current after a quantum quench from equilibrium by rapidly applying a bias voltage in a wide range of initial temperatures. The current exhibits short equilibrium times and saturates upon the decrease of temperature at all times, indicating Kondo behavior both in the transient regime and in the steady state.

However, this bare QMC solver suffers from a dynamical sign problem for long time propagations. To overcome the limitations of this bare treatment, we introduce the "Inchworm algorithm", based on iteratively reusing the information obtained in previous steps to extend the propagation to longer times and stabilize the calculations. We show that this algorithm greatly reduces the required order for each simulation and re-scales the exponential challenge to quadratic in time. We introduce a method to compute Green's functions, spectral functions, and currents for inchworm Monte Carlo and show how systematic error assessments in real time can be obtained. We illustrate the capabilities of the algorithm with a study of the behavior of quantum impurities after an instantaneous voltage quench from a thermal equilibrium state.

We conclude with the applications of the unbiased inchworm impurity solver to DMFT calculations. We employ the methods for a study of the one-band paramagnetic Hubbard model on the Bethe lattice in equilibrium, where the DMFT approximation becomes exact. We begin with a brief introduction of the Mott metal insulator phase diagram. We present the results of both real time Green's functions and spectral functions from our nonequilibrium calculations. We observe the metal-insulator crossover as the on-site interaction is increased and the formation of a quasi-particle peak as the temperature is lowered. We also illustrate the convergence of our algorithms in different aspects.

Contents

List of Figures

List of Abbreviations

DMFT   **D**ynamical **M**ean **F**ield **T**heory

AIM   **A**ndersonl **I**mpurity **M**odel

ED   **E**xact **D**iagonalization

QMC   **Q**uantum **M**onte **C**arlo

CT-QMC   **C**ontinuous **T**ime **Q**uantum Monte Carlo

CT-HYB   **C**ontinuous **T**ime **HYB**ridization expansion

NRG   **N**umerical **R**enormalization **G**roup

DMRG   **D**ensity **M**atrix **R**enormalization **G**roup

NCA   **N**on-**C**rossing Approximation

OCA   **O**ne-**C**rossing Approximation

Introduction

The collective behavior of non-equilibrium systems is poorly understood compared to systems in thermal equilibrium, for which statistical mechanics provides a well established theory. By non-equilibrium systems we refer both to systems held far from thermal equilibrium by an external driving force, and the complementary situation of systems relaxing towards thermal equilibrium after a perturbation of their states. Such systems display a broad range of phenomena, such as nonequilibrium phase transitions and slow collective dynamics, which one would like to understand at a deeper level. The study of non-equilibrium systems has arisen in many different contexts such as interacting many-particle systems out of equilibrium [8], driven diffusive systems [9], and the slow dynamics of glassy systems [10].

In quantum mechanics, due to the macroscopically large number of degrees of freedom, an exact many-body theory has be be ruled out. The simplest successful theory of solids is based on the approximate model of non-interacting or weakly interacting electrons moving in a background lattice of ions. The addition of electronic interaction makes the picture more interesting, and it leads to complex material properties, such as metal-insulator transitions, high temperature superconductivity, and various magnetic phenomena. When such interacting many-particle systems are driven out of equilibrium, a multitude of interesting phenomena can be found. For example, photoinduced phase transitions [11] are able to access electronic states that may differ greatly from states produced with excitations close to equilibrium and can be used to change complex macroscopic material properties on the ultra-fast timescales. Also the dynamics of a correlated system reveals fundamental questions of statistical mechanics such as

the relaxation pathways and thermalization conditions, that are inaccessible via traditional equilibrium physics.

On the other hand, experiments on strongly correlated quantum many-body systems out of equilibrium have reached a high level of precision and control. One can excite complex materials with femtosecond laser pulses and record their subsequent time evolution on the timescale of the electronic motion [12–14]. These ultrafast "pump-probe" spectroscopies enable studies of excitation and relaxation phenomena in correlated fermionic systems. Additionally, in systems of ultracold atoms in optical lattices, interactions and bandwidths can be controlled in a precise manner, and external fields can be mimicked by shaking or tilting the optical lattice [15]. It provides a new way to control and measure the time evolution of interacting lattice systems with a vastly different characteristic time scale compared to electron systems.

The understanding of those nonequilibrium phenomena is challenging for theoretical physics, and completely new theoretical tools have to be developed to guide the experimental progress. And the numerical investigation of non-equilibrium phenomena in quantum many-body systems is a fundamental active and exciting branch of modern computational condensed matter physics. One of the simplest fermionic non-equilibrium quantum problems is the Anderson impurity problem [16]. It contains localized impurity states coupled to a non-interacting bath and appears in a wide range of contexts, including impurities embedded into a host material [16], confined nanostructures [17] and molecules adsorbed on surfaces [18, 19]. It is a basic model of nano-science as representations of quantum dots and molecular conductors.

Impurity models also appear as auxillary models in the non-equilibrium formulation of dynamical mean field theory (DMFT), which is a method that is well suited to capture strong local correlation effects in higher-dimensional systems. DMFT has the advantage of being non-perturbative and applicable to large systems [8, 20]. This method generalizes the mean-field approximations by neglecting spatial variations and treating exactly the temporal quantum fluctuations.

Thus it relies on solving not the actual lattice model, but an equivalent quantum impurity self-consistently embedded in an effective medium. And this approximation becomes exact in the limit of lattices with infinite coordination number. And the Hubbard model, which is believed to contain the main ingredients to describe the qualitative features present in certain classes of strongly correlated materials, can be mapped into an Anderson impurity model supplemented with a self-consistency condition.

Our work studies the single impurity Anderson models out of equilibrium. We use Monte Carlo algorithms to solve the impurity model that captures the initial correlations and treats general time-dependent setups. We also use the DMFT approach to study the Hubbard model in equilibrium on the infinite dimensional Bethe lattice. The non-equilibrium treatment of the Hubbard model in an equilibrium phase enables the access to two-time quantities such as Green's functions and spectral functions in a numerical exact manner, and yields a solution that is independent of ill-posed analytical continuation techniques, such as the maximum entropy method [21].

In Chapter 1 we introduce the Hubbard model and the Anderson impurity model, which are the basic models that are discussed in the thesis. We also present the mathematical framework for nonequilibrium DMFT and derive the exact self-consistency condition for a Bethe lattice. The notions and formalism of time-dependent problems are outlined in Chapter 2. We perform the strong coupling perturbation theory on a single impurity Anderson model explicitly up to the second and fourth orders. Semi-analytic self-consistent approximate methods, NCA and OCA, are also explained. In Chapter 3, the numerical algorithm used in the work - quantum Monte Carlo with hybridization expansion is developed. The simulation processes and measurements are explained. And this bare method can be used to study the transient behavior of a Kondo system after a voltage quench. It manages to capture the short-time dynamics, however, the bare method suffers from a dynamical sign problem and efforts of obtaining accurate results grow exponentially with time propagation. In Chapter 4, an improved algorithm - the

"Inchworm algorithm" is adapted into the Monte Carlo calculations and it rescales the exponential challenge to quadratic. In this way, the solver significantly overcomes the dynamical sign problem and its result can be used in the non-equilibrium DMFT loop to produce reasonable outcomes. So in Chapter 5, the exact results of real-time Green's functions and spectral functions are shown and the signature of a metal-insulator crossover is observed.

Chapter 1

Theoretical Models of Strongly Correlated Electron Systems

In this chapter, we set the framework for the main part of this thesis by introducing the models under investigation and the approximations and methods employed.

The typical application of quantum mechanics to the study of electrons in solids uses a model of non-interacting or weakly interacting fermions to establish the band theory and the Fermi liquid theory, and it has successfully described a large portion of experimental observations, particularly for cases when metallicity was generated by electrons in s and p orbitals. However, the behavior of the transition metal monoxides (FeO, NiO, CoO) compounds, which are antiferromagnetic insulators, yet had been predicted to be metallic because the strong interactions between their d-shell electrons were neglected (cf. de Boer and Verwey (1937)). The accounting of strong Coulomb interactions between these electrons would significantly suppress the mobility at very low temperatures when the average filling is of one electron per atom. Because any one electron attempting to move through the lattice would have to spend most of the time on already occupied atoms and double occupancy of the same orbital is energetically unfavored by the Coulomb repulsion [22]. This insulating state is called the *Mott insulator*. These classes of materials include transition metals and transition metal oxides.
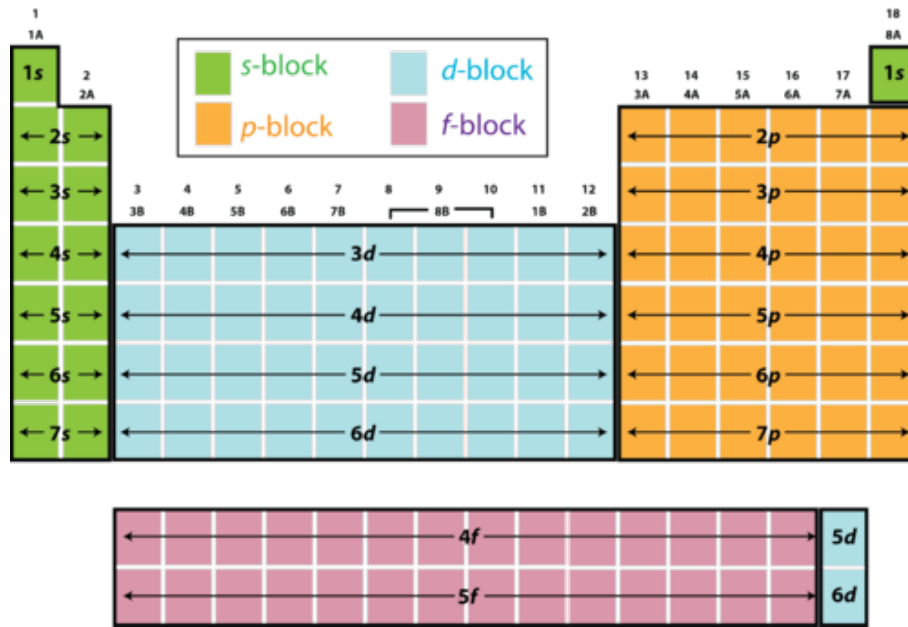
FIGURE 1.1: The electron configurations in the periodic table. The transition metals are the first three rows in the blue area and their properties are strongly dominated by the d-electrons.

Transition elements occupy three rows of the periodic table, extending from the right of the alkali earths (Ca, Sr, Ba) to the poor metals (Zn, Cd, Hg), as shown in Fig. 1.1. The electronic d-shell is completely empty in the alkali earths and completely filled in the noble metals.

In addition to the Mott insulating phase, J. G. Bednorz and K. A. Müller (1986) announced the discovery of superconductivity in a ceramic copper oxide material at a temperature of about 30K. These compounds are poor conductors, and thus their result was unexpected and beyond the scope of the BCS theory. After that, dozens of "high-T_c" compounds have been discovered in the last few decades. Until the discovery of the Fe-based superconductors in 2008, the high-T_c materials all have one or more CuO_2 planes in their structure, which are separated by layers of other atoms (Ba, O, La, etc), as illustrated in Fig. 1.1. Most researchers in this field strongly believe that superconductivity is related to processes occurring in the CuO_2 planes, with the other atoms simply providing the charge carriers. Thus the strong correlations between electrons in transition metal compounds constitute the rich physics in magnetic and non-magnetic Mott insulators, high
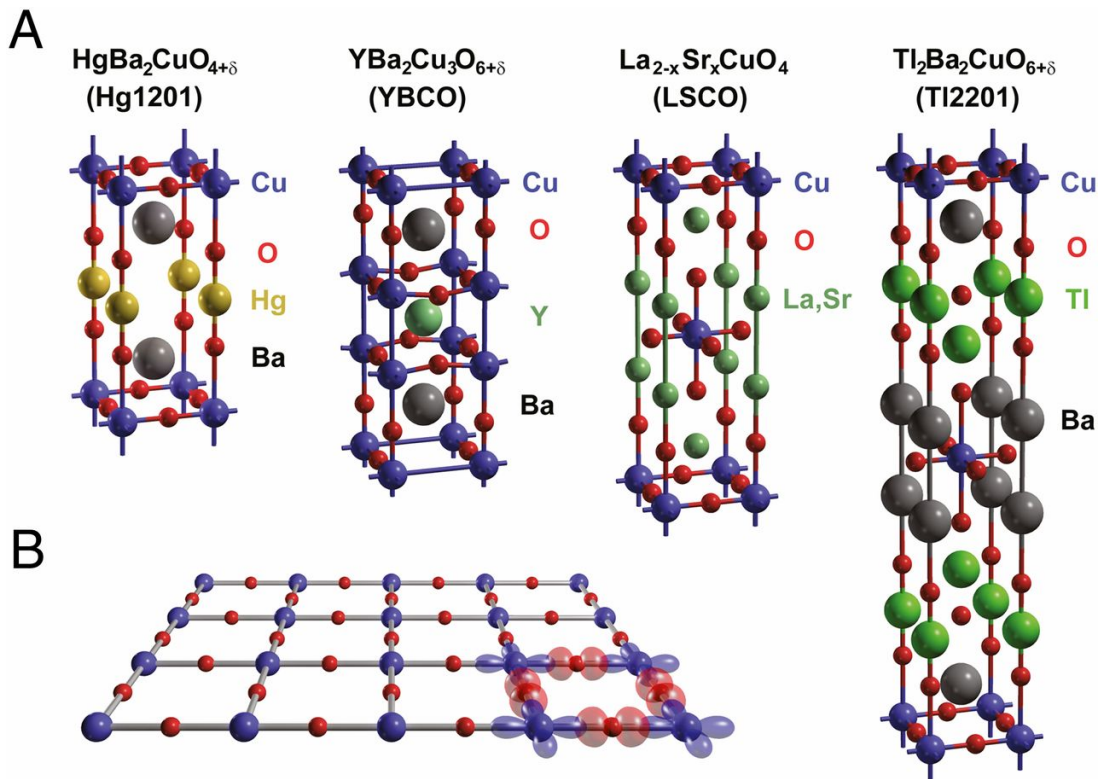
FIGURE 1.2: Crystal structures of four cuprates. (A) The unit cells. (B) The universal building block of the high-T_c cuprates is the CuO_2 sheet. The most important electronic orbitals, Cu $d_{x^2-y^2}$ and O p_σ, are shown [2].

temperature superconductors. And these observations launched the long and continuing history of the field of strongly correlated electrons [23, 24].

Already in equilibrium, strong electronic correlations bring about a tantalizing variety of novel phenomena. If such a system is driven out of equilibrium, we can expect even richer physics, of which only a small fraction has been discovered so far, and of which even less can be considered as being "understood". On the experimental side, ultrafast pump-probe spectroscopies enable studies of excitation and relaxation phenomena in correlated fermionic systems [25], while ultracold atoms in optical lattices provide a new way to control and measure the time evolution of interacting lattice systems with a vastly different characteristic time scale compared to electron systems [26].

The model that is believed to be capable of capturing these features and is most

successful and most widely studied for the interactions present in correlated electron systems is the Hubbard model, which was independently conceived by Martin Gutzwiller [27], Junjiro Kanamori [28] and John Hubbard [29]. It is one of the simplest models of interacting fermions, but despite its simplicity, it exhibits a wide range of correlated electron behavior including interaction-driven metal-insulator transitions, superconductivity, and magnetism. The precise behavior depends delicately on parameters, creating an interesting challenge for theory and computation. It is exactly solvable for the case of a 1-dimensional system [30]. However, it is not the case in general lattices, and the simple perturbative approach is not possible because of the lack of a weak-coupling parameter. And the numerical solutions for the lattice Hamiltonian using non-perturbative algorithms such as exact diagonalization (ED) or quantum Monte Carlo (QMC) are severely restricted by certain problems. The exponential growth of the Hilbert space with system size is the crucial problem for ED. And the fermionic sign problem limits QMC calculations only for temperatures too high to be relevant for physically interesting situations [24].

A new approach to these problems started with the observation by W. Metzner and D. Vollhardt [31] that significant simplifications occur in the limit of infinite coordination number where the self-energy becomes independent of momentum [32]. Then A. Georges and G. Kotliar [1] presented an exact mapping of the Hubbard model in infinite dimensions onto a single-impurity Anderson model supplemented by a self-consistency condition. This provides a mean-field picture of strongly correlated systems with neglecting the spatial correlations, which becomes exact as $Z \to \infty$. The method is called the dynamical mean field theory (DMFT) and it has greatly contributed to our present understanding of strongly correlated systems in equilibrium, in particular, of Mott physics [20, 33]. Then in 2002, P. Schmidt and H. Monien proposed a generalized DMFT for the nonequilibrium physics in the presence of a time-dependent external field [34] and a general formulation of the nonequilibrium DMFT and its application was given in 2006 by J. K. Freericks *et al.* [35]. Nonequilibrium DMFT can be combined with several numerical implementations as the solver of the effective Anderson

impurity model (AIM), such as quantum Monte Carlo [36] and density matrix renormalization group (DMRG) [37] techniques and has the advantage that it is nonperturbative and can capture both short-time and long-time evolutions for any parameter regimes.

In the following, we will first discuss the Hubbard model in a general context in Sec. 1.1, and the Anderson impurity model that describes local moments embedded in a metallic host as an effective model for solving the Hubbard model in Sec. 1.2. Then we will introduce the nonperturbative treatment within the nonequilibrium dynamical mean field theory (DMFT) in Sec. 1.3 and we state the self-consistency condition in the case of a $Z \to \infty$ Bethe lattice, which will be a main focus for the purpose of this thesis because DMFT becomes exact in this limit.

1.1   Hubbard Model

The nonequilibrium experiments with ultracold atoms in optical lattices [15], pump-probe spectroscopy with femtosecond time resolution [13, 25] can access the real-time dynamics in materials with strong correlation effects. They are capable of measuring quantities on their intrinsic microscopic time scale, defined by the electron hopping between crystal lattice sites and reveal striking phenomena such as photoinduced insulator-to-metal transitions in correlated Mott and charge transfer insulators [25, 38] and pump-induced melting and recovery of charge density waves [39].

The ongoing experimental progress inspires the study of the Hubbard model driven out of equilibrium [40]. The Hubbard model, although being highly oversimplified, is believed to contain the main ingredients to describe interacting quantum mechanical particles, originally fermions, in certain types of materials such as the cuprates and organics. Its basis is a tight binding description of electrons in materials. The idea is that only one or few energy bands close to the Fermi energy contribute to the spectrum. When electrons on the Fermi surface

originate from the d orbitals, the bandwidth is determined by the amount of over-lap between d orbitals on adjacent sites, and the typically small extent of these orbitals compared to the lattice constant suggests a narrow-band feature and the strongly localized character of d electrons. Thus the tight-binding approximation provides a better model of the kinetic energy of electrons. This also implies that interactions between electrons on the same ion are much larger than interactions of electrons on different ions and the screening effects make the longer-range Coulomb interactions exponentially weak. Although nearest-neighbor interactions can sometimes be strong enough to generate specific physics, for example the charge-ordering effect, they will be neglected and only taken in consideration when using the extended Hubbard model instead [41, 42]. Therefore in the simplest Hubbard model, the interaction taken into account is just an on-site interaction. The Hamiltonian of the single-band Hubbard model then contains two parts:

$$H = - \sum_{\langle i,j \rangle, \sigma} v_{ij} c_{i\sigma}^{\dagger} c_{j\sigma} + U \sum_{i} n_{i\uparrow} n_{i\downarrow} \tag{1.1}$$

where $c_{i\sigma}^{\dagger}$ $(c_{i\sigma})$ creates (annihilates) an electron with spin $\sigma = \uparrow, \downarrow$ on site i, $n_{i\sigma} = c_{i\sigma}^{\dagger} c_{i\sigma}$ is the number operator, v_{ij} denotes the hopping amplitude, $\langle i, j \rangle$ means the hopping is restricted to purely nearest neighbor hopping and U is the repulsive on-site Coulomb interaction strength. The first part in the Hamiltonian is the single-particle part, often called kinetic energy, describes particles hopping on a lattice which originates from the tight binding model and the second part is the additional two-particle on-site interaction term.

1.2   Anderson Impurity Model

The Anderson impurity model was originally introduced in the 60's to explain the behavior of magnetic impurities (Fe, Mn, Cr) diluted into non magnetic metals [16].

Besides being auxiliary models in nonequilibrium DMFT, quantum impurity models are basic to nanoscience as representations of quantum dots and molecular conductors [17] and have been used to understand the absorption of atoms on surfaces [19, 43]. Also transport measurements on quantum dots [44] enable the study of the basic question that how localized electrons interact with delocalized electrons and reveal non-equilibrium Kondo phenomena [45, 46].

The Hamiltonian contains the electron band that consists of a collection of un-correlated states, the energy of the impurity orbital (designed to describe the impurity atoms of the system) together with a Coulomb repulsive interaction U when two electrons are located on the impurity site, and a hybridization between the band states and the impurity state, i.e. for electrons to hop from the impurity to the bath and back. In this thesis, we present the single impurity Anderson model as

$$H = H_D + H_{\text{bath}} + H_{\text{hyb}}, \tag{1.2a}$$

$$H_D = \sum_\sigma \varepsilon_d n_\sigma + U n_\uparrow n_\downarrow, \tag{1.2b}$$

$$H_{\text{bath}} = \sum_{\alpha k \sigma} \left(\varepsilon_k + \frac{\alpha V(t)}{2} \right) n_{\alpha k \sigma}, \tag{1.2c}$$

$$H_{\text{hyb}} = \sum_{\alpha k \sigma} (\mathcal{V}_k^\alpha c_{\alpha k \sigma}^\dagger d_\sigma + \mathcal{V}_k^{\alpha*} d_\sigma^\dagger c_{\alpha k \sigma}). \tag{1.2d}$$

where H describes an interacting dot (H_D) coupled to non-interacting leads (H_{bath}) by tunneling processes (H_{hyb}). The dot Hamiltonian H_D spans a Hilbert space generated by $d_\uparrow^\dagger$ and $d_\downarrow^\dagger$ with four "atomic states" $|\phi\rangle = |0\rangle, |\uparrow\rangle, |\downarrow\rangle$, and $|\uparrow\downarrow\rangle$, which follows from the Pauli exclusion principle because one impurity site can hold up to two electrons with different spins, and dot occupation is given by $n_\sigma = d_\sigma^\dagger d_\sigma$. ε_d is the impurity level spacing, and U is the electronic repulsion strength. Lead electrons are characterized by a spin index $\sigma = \uparrow\downarrow$, a momentum quantum number k, and a lead index $\alpha = \pm 1$, and are annihilated by the operator $c_{\alpha k \sigma}$. Lead densities are $n_{\alpha k \sigma} = c_{\alpha k \sigma}^\dagger c_{\alpha k \sigma}$ and ε_k is the lead dispersion. $\alpha = \pm 1$ labels the left (+) and right (−) leads, but in general, the system can

have any number of leads. $\mathcal{V}_k^\alpha$ is the tunneling matrix element describing hopping processes between the impurity and the leads.

In this thesis, we consider two cases for the impurity model: the equilibrium case, where none of the parameters are time-dependent and $V(t) = 0$; and the case of a symmetric voltage quench $V(t) = V\theta(t)$, with $\theta(t)$ being a Heaviside step function. In the second case, the system is in equilibrium for $t < 0$, and for $t > 0$ the lead levels ε_k are instantaneously moved to $\varepsilon_k \pm \frac{V}{2}$, with the sign depending on the lead index α.

1.3   Nonequilibrium Dynamical Mean Field Theory

As in the classic cases, the goal of a mean-field theory is to approximate a lattice problem with many degrees of freedom by a single-site effective problem with fewer degrees of freedom. The underlying idea is that the dynamics at a given site can be thought of as the interaction of the degrees of freedom at this site with an external bath created by all other degrees of freedom on other sites in the system. An example of this is the Ising model with ferromagnetic couplings solved by the Weiss mean-field theory. This idea can be directly extended to quantum many-body systems. The dynamical mean field theory (DMFT) aims to approximate the full quantum many-body problem by a single impurity problem, where the dynamics of the rest of the system is expressed as a mean field that needs to be determined self consistently.

The difference between the DMFT and the static mean-field theory is the single site (impurity) in DMFT can dynamically exchange particles with the environment which represents local quantum fluctuations in the lattice system. Besides this, a formal analogy to the classical mean-field theory remains: the local Green's function $G(t, t')$ is obtained from an effective model that involves only one site of the lattice. This site is coupled to a fluctuating mean-field $\Delta(t, t')$ that resembles
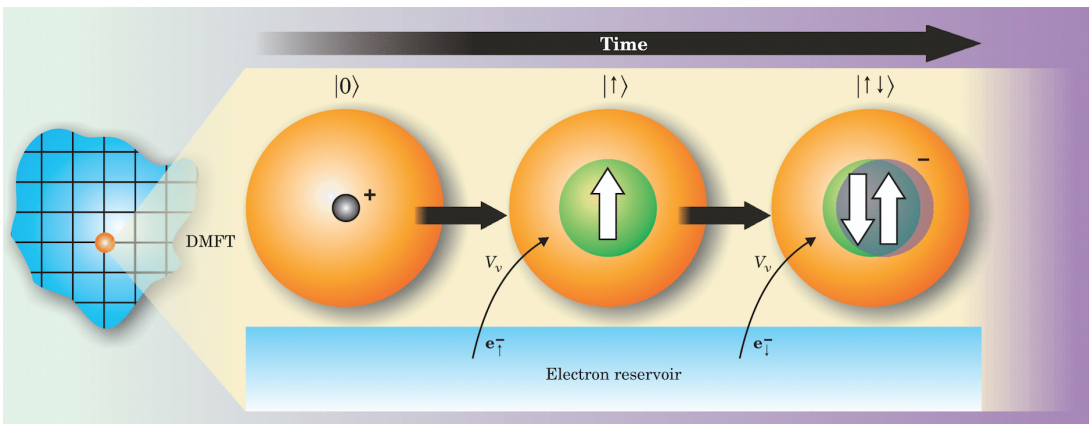
FIGURE 1.3: Dynamical mean field theory (DMFT) of correlated-electron solids replaces the full lattice of atoms and electrons with a single impurity atom imagined to exist in a bath of electrons. The approximation captures the dynamics of electrons on a central atom (in orange) as it fluctuates among different atomic configurations, shown here as snapshots in time. In this illustration of one possible sequence involving two transitions, an atom in an empty state absorbs an electron from the surrounding reservoir in each transition [3].

the exchange of particles with the rest of the lattice and is to be determined self consistently as a function of $G(t, t')$ because we do not know the right mean field prior to the procedure [8, 20].

In this section, we will present a simplified derivation and discussion of the nonequilibrium DMFT. We formulate the mapping from the single band Hubbard model to a single site Anderson impurity model in Sec. 1.3.1 and we state the self-consistency equations in detail in Sec. 1.3.2.

1.3.1 Mapping of the models

To start, we rewrite the Hamiltonian of the single band Hubbard model in Eq. (1.1) as

$$H = - \sum_{\langle i,j \rangle, \sigma} v_{ij} c_{i\sigma}^\dagger c_{j\sigma} + \sum_i H_{\text{loc}}^{(i)} \tag{1.3}$$

where

$$H_{\text{loc}}^{(i)} = U \sum_i c_{i\uparrow}^\dagger c_{i\uparrow} c_{i\downarrow}^\dagger c_{i\downarrow} \tag{1.4}$$

so the action of the Hubbard model is

$$S_{\text{hub}} = \int dt \int dt' \left(\sum_{i\sigma} c_{i\sigma}^*(t)(i\partial_t + \mu)c_{i\sigma}(t') + \sum_{\langle i,j \rangle,\sigma} v_{ij}c_{i\sigma}^*(t)c_{j\sigma}(t') \right) - \sum_i \int dt H_{\text{loc}}^{(i)}(t) \tag{1.5}$$

where μ is the chemical potential of the lattice electrons. We adapt the "*effective medium interpretation*" [47] and replace the interacting lattice model by a non-interacting medium with a propagator $G_{\text{med}}(\mathbf{k}; t, t')$ specified by a local self-energy $\Sigma(\mathbf{k}; t, t') = \Sigma(t, t')$ to be determined self-consistently. The action of the effective medium thus reads

$$S_{\text{med}} = \int dt \int dt' \sum_{\mathbf{k}\sigma} c_{\mathbf{k}\sigma}^*(t)G_{\text{med}}^{-1}(\mathbf{k}; t, t')c_{\mathbf{k}\sigma}(t') \tag{1.6}$$

and

$$G_{\text{med}}^{-1}(\mathbf{k}; t, t') = i\partial_t + \mu - \epsilon_{\mathbf{k}} - \Sigma(t, t'). \tag{1.7}$$

One then imagines that a local interaction $Un_{0\uparrow}n_{0\downarrow}$ is introduced at a single site 0 of this effective medium, and that the self energy Σ has simultaneously been removed at this single site. The action of this new resulting lattice model with a single-site embedding thus reads

$$S_{\text{emb}} = S_{\text{med}} - U \int dt n_{0\uparrow}(t)n_{0\downarrow}(t) + \int dt \int dt' \sum_{\sigma} c_{0\sigma}^*(t)\Sigma(t, t')c_{0\sigma}(t'). \tag{1.8}$$

This can be turned into an effective action for site 0 only, by integrating out all other sites. And because the sites $i \neq 0$ enter only quadratically S_{emb}, it can be performed exactly. Now we omit the subscript $i = 0$ and obtain

$$S_{\text{eff}} = \int dt \int dt' \sum_{\sigma} c_{\sigma}^*(t)G_{0,\text{hyb}}^{-1}(t, t')c_{\sigma}(t') - U \int dt n_{\uparrow}(t)n_{\downarrow}(t) \tag{1.9}$$

with

$$G_{0,\text{hyb}}^{-1}(t, t') = i\partial_t + \mu - \Delta(t, t') \tag{1.10}$$

where $\Delta(t, t')$ is the auxiliary mean field. Using Eq. (2.42), one can show that this effective action is exactly the action of the Anderson impurity model after

14

integrating out the bath degrees of freedom. And to be consistent with the effective medium approximation, one requires that the interacting Green's function obtained from the S_{eff} coincides with the on-site (local) Green's function of the medium

$$G_{\text{latt}}(t, t') = \sum_{\mathbf{k}} G_{\text{med}}(\mathbf{k}; t, t') \tag{1.11}$$

$$= \sum_{\mathbf{k}} (i\partial_t + \mu - \epsilon_{\mathbf{k}} - \Sigma(t, t'))^{-1} \tag{1.12}$$

$$= \int d\epsilon \ D(\epsilon) \left[i\partial_t + \mu - \epsilon - \Sigma(t, t') \right]^{-1} \tag{1.13}$$

where $D(\epsilon)$ is the non-interacting density of states of the lattice. And we can see the transition from $\sum_k$ to $\int_\epsilon$ is only possible for the local self-energy $\Sigma(t, t')$.

1.3.2   The self-consistency equations

Equations (1.9), (1.10) and (1.13) along with the Dyson equations form a set of identities that can be employed to obtain a self-consistent solution of the effective action in Eq. (1.9), as illustrated in Fig. 1.4.

This is an iterative procedure: we start with an initial guess for the bare Green's function $G_{0,\text{hyb}}(t, t')$ of the impurity model. Note that this is the Green's function that is non-interacting but contains the hybridization between the bath and the impurity in the Anderson impurity model. Often, the Green's function for the non-interacting lattice problem is one good starting point. Then using Eq. (1.10) one gets the initial auxiliary mean field $\Delta(t, t')$. Having obtaining such an initial input, we need to solve the Anderson impurity model, i.e. obtain $G(t, t')$ that is the fully interacting Green's function of the impurity out of the initial $\Delta(t, t')$. This part is called an impurity solver and will be discussed in Chapters 3 and 4. The impurity (local) self-energy can be computed by Dyson equation,

$$\Sigma_{\text{imp}}(t, t') = G_{0,\text{hyb}}^{-1}(t, t') - G^{-1}(t, t') \tag{1.14}$$

$$\Delta(t,t')$$

$$G_{0,\text{hyb}}^{-1}(t,t')$$

EOM

$$\Delta(t,t') = i\partial_t + \mu - G_{0,\text{hyb}}^{-1}(t,t')$$

Impurity solver

$$G_{0,\text{hyb}}(t,t')$$

$$G(t,t')$$

Dyson equation

$$G_{0,\text{hyb}}^{-1}(t,t') = \Sigma_{\text{imp}}(t,t') + G_{\text{latt}}^{-1}(t,t')$$

Dyson equation

$$\Sigma_{\text{imp}}(t,t') = G_{0,\text{hyb}}^{-1}(t,t') - G^{-1}(t,t')$$

$$G_{\text{latt}}(t,t')$$

$$\Sigma_{\text{imp}}(t,t')$$

On-site projection

$$G_{\text{latt}}(t,t') = \int d\epsilon \, D(\epsilon) \left[i\partial_t + \mu - \epsilon - \Sigma_{\text{imp}}(t,t') \right]^{-1}$$
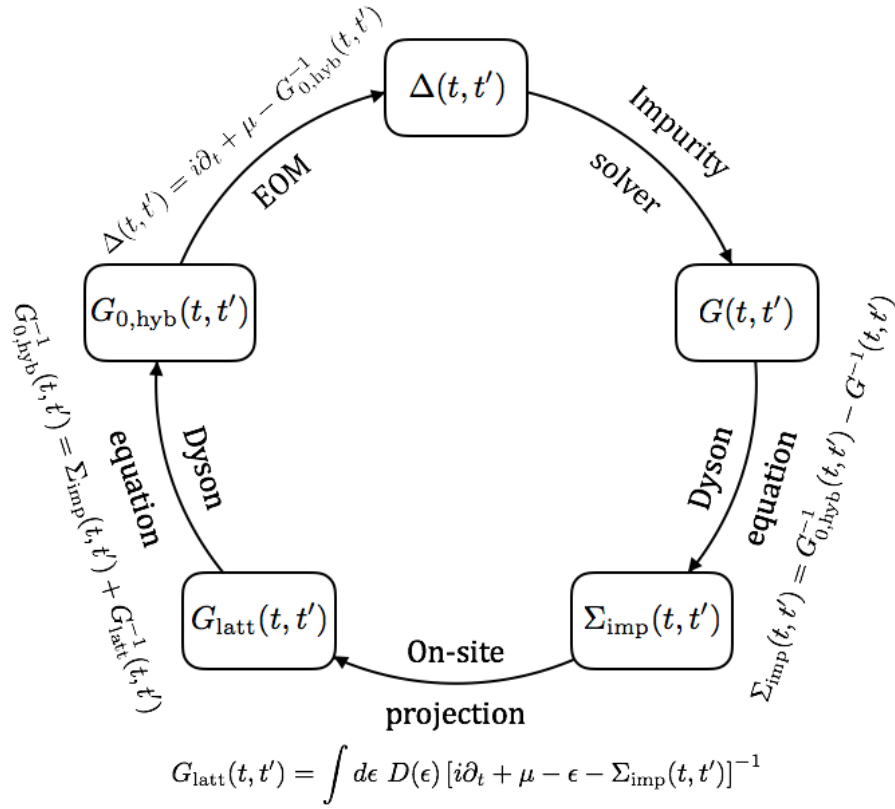
FIGURE 1.4: The iterative self-consistency procedure of the nonequilibrium DMFT in the most general case.

where the inverse $\cdot^{-1}$ is a symbolic form and if

$$\int d\bar{t} \, A(t,\bar{t}) \cdot B(\bar{t},t') = \delta(t,t') \tag{1.15}$$

we denote $B = A^{-1}$ and it associates with the matrix inverses in numerical evaluations. Then we employ the self-consistent condition Eq. (1.13) and do the on-site projection using the impurity (local) self-energy to get the local lattice Green's function

$$G_{\text{latt}}(t,t') = \int d\epsilon \, D(\epsilon) \left[i\partial_t + \mu - \epsilon - \Sigma_{\text{imp}}(t,t') \right]^{-1} \tag{1.16}$$

Note that this step illustrates the mean-field character of the DMFT equations particularly clearly: the local Green function of the interacting system is given by the non-interacting Green function with a shift of $\Sigma_{\text{imp}}(t,t')$. After this, using

16

$\Delta(t-t')$

Fourier transform

Impurity solver

$\Delta(\omega)$

$G(t-t')$

$\Delta(\omega) = \omega + \mu - G_{0,\text{hyb}}^{-1}(\omega)$

EOM

Fourier transform

$G_{0,\text{hyb}}(\omega)$

$G(\omega)$

$G_{0,\text{hyb}}^{-1}(\omega) = \Sigma_{\text{imp}}(\omega) + G_{\text{latt}}^{-1}(\omega)$

Dyson equation

Dyson equation

$\Sigma_{\text{imp}}(\omega) = G_{0,\text{hyb}}^{-1}(\omega) - G^{-1}(\omega)$

$G_{\text{latt}}(\omega) = \int d\epsilon \dfrac{D(\epsilon)}{\omega + \mu - \epsilon - \Sigma_{\text{imp}}(\omega)}$

$G_{\text{latt}}(\omega)$

$\Sigma_{\text{imp}}(\omega)$

On-site projection
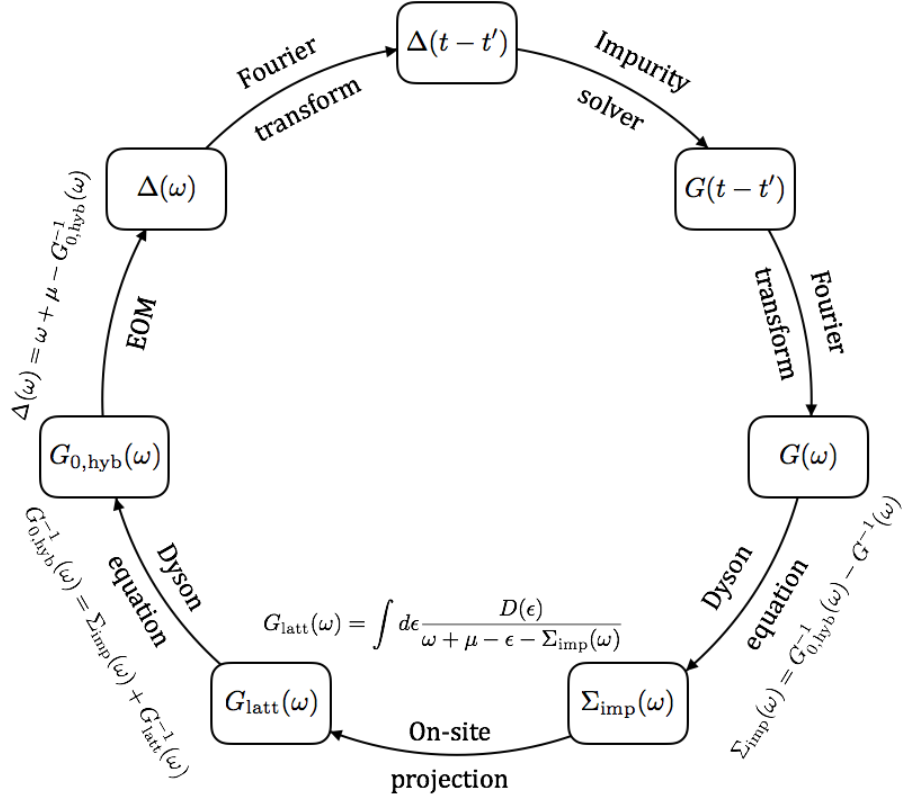
FIGURE 1.5: The iterative self-consistency procedure of the nonequilibrium DMFT in the equilibrium case. Then the quantities are translational invariant, so it is possible to work in the frequency space and save time from calculating the inverse of matrices in the time space.

the Dyson equation,

$$G_{0,\text{hyb}}^{-1}(t,t') = \Sigma_{\text{imp}}(t,t') + G_{\text{latt}}^{-1}(t,t') \qquad (1.17)$$

we get a new guess for the bare Green's function $G_{0,\text{hyb}}(t,t')$ and therefore a new input $\Delta(t,t')$ for the impurity solver. In time-independent cases, one can switch to the frequency space and avoid the explicit matrix inverses. And a similar self-consistent procedure is illustrated in Fig. 1.5.

The self-consistency is remarkably stable: starting from an initial guess that has approximately the right short-time behavior the loop converges after a few iterations to a self-consistent solution on a $Z \to \infty$ Bethe lattice. Far away from phase transitions this convergence is rather quick and is achieved within about 2–5 iterations. In the vicinity of phase transitions the convergence slows down

considerably, but is usually achieved within at most 10 iterations. We did not observe cases in which this self consistency did not converge or oscillate between various (meta-) stable solutions.

1.4 The Bethe lattice

As we noted in the beginning of this chapter, the only case when the DMFT approach yields an exact solution of the lattice properties is in the infinite coordination limit. One of the common choices is the Bette lattice [48]. It has the advantages that the band edges are well-defined and the bandwidth is finite. Also, as we will see in this section, the self-consistent equations of DMFT can be analytically inverted, allowing for a simple closed form expression of the lattice self-energy from the impurity Green's function.

A Bethe lattice or Cayley tree, introduced by Hans Bethe in 1935 [49], is an infinite connected cycle-free graph where each node is connected to Z neighbours, where Z is called the coordination number. Fig. 1.6 shows the Bethe lattice for $Z = 4$, where a site is at each vertex. Starting from the central point, there are four neighbors. Each of those four neighbors also has four neighbors. Thus each point has the same symmetry.

Strictly speaking the Bethe lattice is a pseudolattice because it does not possess the property of discrete translational symmetries in finite dimensions of Bravais lattices. Nevertheless, it plays an important role in statistical and condensed-matter physics because some problems involving disorder and/or interactions can be solved exactly when defined on a Bethe lattice, for example, Ising models [49, 50], percolation [51, 52], and Anderson localization [53]. There are two special properties that make the Bethe lattice particularly suited for theoretical investigations. One is its self-similar structure which may lead to recursive solutions. The other is the absence of closed loops which restricts interference
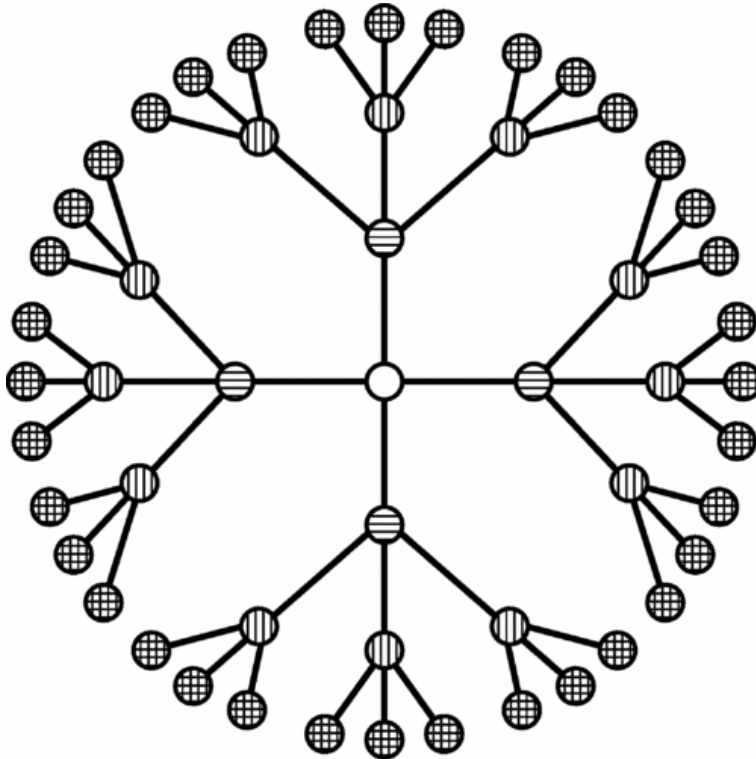
FIGURE 1.6: Part of the Bethe lattice with coordination number $Z = 4$. Any two sites are connected by a unique shortest path of bonds. Starting from the site marked by the open circle, horizontally shaded circles can be reached by one lattice step (NN), vertically shaded circles by two lattice steps (NNN), and doubly shaded circles by three lattice steps. Note that the lattice is infinite and that all sites are equivalent; the shading appears only for visualization of hopping processes [4].

effects of quantum-mechanical particles in the case of nearest-neighbor (NN) coupling [4, 54]. In the following, we will see that the Green's function of the non-interacting Hubbard model (tight-binding Hamiltonian) with an uniform nearest neighbor hopping v can be computed analytically on the Bethe lattice. Then we take the $Z \to \infty$ limit and obtain a simple closed form relation of $\Delta[G]$ for the DMFT self-consistency condition in the case of a Bethe lattice with infinite neighbors. The Hamiltonian with a chemical potential term reads

$$H = -v \sum_{j,\delta} c_j^\dagger c_{j+\delta} - \mu \sum_j c_j^\dagger c_j \tag{1.18}$$

where the summation over δ runs over the Z neighbors. Spin plays no role in the calculation and therefore can be omitted. Then we write the Hamiltonian as

$$H = H_0 + K \tag{1.19}$$

where $H_0 = -\mu N$ is considered as the non-interacting Hamiltonian and the hopping kinetic energy K is considered as an interaction. The local non-interacting Green's function is then known as

$$G^{(0)}(\omega) = -i \int dt e^{i\omega t} \left\langle \mathcal{T} c_j(t) c_j^\dagger(0) \right\rangle = \frac{1}{\omega + \mu} \tag{1.20}$$

Every site has the same Green's function, so there is no need to put on a label such as "j" in the expression. In order to obtain the full Green's function we need to determine the expression for the proper self-energy part $\Sigma(\omega)$ so that

$$G(\omega) = \frac{1}{\omega + \mu - \Sigma(\omega)} \tag{1.21}$$

And the self-energy $\Sigma(\omega)$ is found using perturbation theory on K. Since the interactions are simple and quadratic, it is possible to find the exact result. The self-energy consists of the processes where electrons hop to their neighbors and then hop back and each hop has an amplitude factor v. From the perturbation expansion on K, we know that the total number of hops in each self-energy term must be an even number $2n$ where $n = 1, 2, 3 \ldots$. For $2n$ hops of electrons returning back to the original site, we denote its contribution in the self-energy as $\Sigma^{(n)}$.

The lowest order self-energy $\Sigma^{(1)}$, as shown in Fig. 1.7, originates from the process where an electron hops to its neighboring sites and then hops back to its original site. There are totally Z neighbors, and the intermediate propagator is given by the local non-interacting Green's function $G^{(0)}(\omega)$. Thus, the lowest order self-energy is given by

$$\Sigma^{(1)}(\omega) = \frac{Zv^2}{\omega + \mu} \tag{1.22}$$
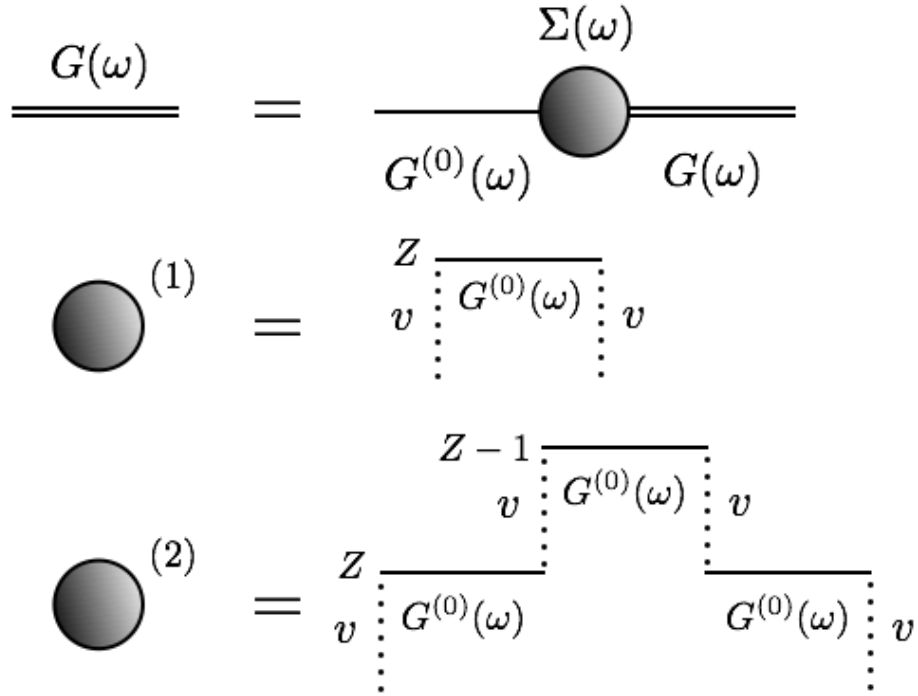
FIGURE 1.7: Diagrammatic expansion of the self-energy on the Bethe lattice. The second order and the fourth order are shown. The lowest order self-energy $\Sigma^{(1)}$ consists of the process where an electron hops to its Z neighboring sites and then hops back to its original site. The next order self-energy $\Sigma^{(2)}$ includes terms where electrons hop twice to a second-nearest neighbor, and then hop back. The first hop has Z choices and the second one has only $Z-1$ since the hop back to the starting point has already been included in $\Sigma^{(1)}$.

The next order self-energy $\Sigma^{(2)}$ comes from the fourth order of perturbation theory, and includes terms where electrons hop twice to a second-nearest neighbor, and then hop back. The first hop has Z choices as before, whereas the second one has only $Z-1$ since the hop back to the starting point has already been included in the lowest order contribution. Thus the next order self-energy has the form

$$\Sigma^{(1)}(\omega) = \frac{Z(Z-1)v^4}{(\omega+\mu)^3} \tag{1.23}$$

We can rewrite these two terms of the self-energy as

$$\Sigma^{(1+2)}(\omega) = \frac{Zv^2}{\omega+\mu}\left[1+\frac{(Z-1)v^2}{(\omega+\mu)^2}\right] \tag{1.24}$$

$$= \frac{Zv^2}{\omega+\mu-\frac{(Z-1)v^2}{\omega+\mu}} - O(v^6) \tag{1.25}$$

21

The terms in brackets [·] describe processes where, after hopping from the starting point to the first neighbor, the electron hops to-and-from its neighbors multiple times before returning back to the original site. It can only hop back to the original site once, because when it hops away from the original site the second time, it is counted as another self-energy contribution. Then we realize the pattern of this "hopping away" self-energy in the denominator and define it as $\Sigma_D(\omega)$. We have

$$\Sigma_D(\omega) = \frac{(Z-1)v^2}{\omega + \mu - \Sigma_D(\omega)} \tag{1.26}$$

and

$$\Sigma(\omega) = \frac{Zv^2}{\omega + \mu - \Sigma_D(\omega)} \tag{1.27}$$

The quadratic equation can be solved exactly and yields

$$\Sigma_D(\omega) = \frac{1}{2}\left[(\omega+\mu) - \text{sign}(\omega)\sqrt{(\omega+\mu)^2 - 4(Z-1)v^2}\right] \tag{1.28}$$

and the full self-energy is

$$\Sigma(\omega) = \frac{2Zv^2}{\omega + \mu + \text{sign}(\omega)\sqrt{(\omega+\mu)^2 - 4(Z-1)v^2}} \tag{1.29}$$

$$= \frac{Z}{2(Z-1)}\left[\omega + \mu - \text{sign}(\omega)\sqrt{(\omega+\mu)^2 - 4(Z-1)v^2}\right] \tag{1.30}$$

And this yields the full Green's function

$$G(\omega) = \frac{1}{\omega + \mu - \Sigma(\omega)} \tag{1.31}$$

$$= \frac{2(Z-1)}{(Z-2)(\omega+\mu) + \text{sign}(\omega)Z\sqrt{(\omega+\mu)^2 - 4(Z-1)v^2}} \tag{1.32}$$

We can then compute the density of states

$$D(\epsilon) = -\frac{1}{\pi}\Im G(\epsilon + i0) = \frac{1}{2\pi}\frac{\sqrt{4(Z-1)v^2 - \epsilon^2}}{Zv^2 - \epsilon/Z}\Theta\left(4(Z-1)v^2 - \epsilon^2\right) \tag{1.33}$$

where $\Theta(\cdot)$ is the heaviside step function. We see from this expression that the bandwidth of the Bethe lattice scales with the coordination number as $\sqrt{Z-1}$.

Therefore, in order to maintain a finite bandwidth in the limit of $Z \to \infty$, one has to alter the definition of the hopping amplitude by scaling it as $v \to v/\sqrt{Z}$. With this new definition, the density of states becomes semielliptic in the limit of infinite coordination $Z \to \infty$:

$$D(\epsilon) = \frac{1}{2\pi v^2}\sqrt{4v^2 - \epsilon^2}\,\Theta\left(2v - |\epsilon|\right) \tag{1.34}$$

Now, we will show that the DMFT self-consistency equations have a simple form in the case of a Bethe lattice with infinite coordination number. The requirement that the lattice self-energy of the interacting problem is momentum-independent allows us to write the local Green's function as the equation at the bottom of Fig. 1.5:

$$G_{\text{latt}}(\omega) = \int d\epsilon \frac{D(\epsilon)}{\omega + \mu - \epsilon - \Sigma_{\text{imp}}(\omega)} \tag{1.35}$$

Since we know that

$$G(\omega) = \int d\epsilon \frac{D(\epsilon)}{\omega - \epsilon} \tag{1.36}$$

we can write that

$$G_{\text{latt}}(\omega) = G(\omega + \mu - \Sigma_{\text{imp}}(\omega)) \tag{1.37}$$

where $G(\omega)$ is the local non-interacting lattice Green's function, for example, Eq. (1.32) for the Bethe lattice. And from Eq. 1.32, we can derive that $G_B(\omega)$, the local non-interacting Bethe lattice Green's function, obeys the following relation:

$$\frac{Zv^2 - \omega^2}{Z - 1}\,G_B(\omega) + \frac{1}{G_B(\omega)} = \frac{Z - 2}{Z - 1}\omega \tag{1.38}$$

where we have done the scaling $v \to v/\sqrt{Z}$ for finite bandwidth. We then obtain the following relation for the $G_{\text{latt}}(\omega)$

$$\left[\frac{Zv^2 - (\omega + \mu - \Sigma_{\text{imp}}(\omega))^2}{Z - 1}\right]G_{\text{latt}}(\omega) + \frac{1}{G_{\text{latt}}(\omega)} = \frac{Z - 2}{Z - 1}(\omega + \mu - \Sigma_{\text{imp}}(\omega)) \tag{1.39}$$

And in the infinite coordination limit $Z \to \infty$ this simplifies to

$$v^2 G_{\text{latt}}(\omega) + \frac{1}{G_{\text{latt}}(\omega)} = \omega + \mu - \Sigma_{\text{imp}}(\omega) \tag{1.40}$$

Connecting the Dyson equation Eq. (1.14) written as

$$G_{0,\text{hyb}}^{-1}(\omega) = \Sigma_{\text{imp}}(\omega) + G_{\text{latt}}^{-1}(\omega) \tag{1.41}$$

we have

$$G_{0,\text{hyb}}^{-1}(\omega) = \omega + \mu - v^2 G_{\text{latt}}(\omega) \tag{1.42}$$

There we obtain a closed form self-consistency equation $\Delta[G]$:

$$\Delta(\omega) = \omega + \mu - G_{0,\text{hyb}}^{-1}(\omega) = v^2 G_{\text{latt}}(\omega) = v^2 G(\omega) \tag{1.43}$$

where $G(\omega)$ is the full Green's function for the impurity model and comes directly from the impurity solver. Even though the derivation is formulated in the equilibrium case, it can be easily generalized to the nonequilibrium case and reads

$$\Delta(t,t') = v^2 G(t,t') \tag{1.44}$$

This relation is valid when the paramagnetic spin rotational symmetry holds. It can be shown [20] that for antiferromagnetic cases, we can partition the Bethe lattice into two sublattices with ferromagnetic ordering and obtain a similar closed form relation

$$\Delta_\sigma(t,t') = v^2 G_{\bar\sigma}(t,t') \tag{1.45}$$

where $\bar\sigma$ denotes the opposite spin orientation.

Chapter 2

Non-Equilibrium Strong Coupling Perturbation Theory

As we discussed in the previous chapter, the Hubbard model provides a simplified description of local electronic interactions that is generally accepted as describing the qualitative features present in certain classes of strongly correlated materials. However, this simplified version is still complicated enough that exact analytic approach is impossible. Therefore, further simplifications are necessary. The Dynamical Mean Field Theory, which was first developed for equilibrium computations and was extended to calculate time-dependent correlation functions, is one such simplification. This method solves the problem exactly when the on-site self-energy is purely local, which is the case for infinite-dimensional lattices. The solution can then be obtained by considering the mapping of the lattice model to an equivalent Anderson impurity model, with the fermionic impurity self-consistently embedded in an infinite conduction band. The resulting effective Hamiltonian [1] reads:

$$H = \sum_{k\sigma} \varepsilon_k c_{k\sigma}^\dagger c_{k\sigma} + \sum_{k\sigma} (\mathcal{V}_k c_{k\sigma}^\dagger d_\sigma + \mathcal{V}_k^* d_\sigma^\dagger c_{k\sigma}) + \sum_\sigma \varepsilon_d d_\sigma^\dagger d_\sigma + U n_\uparrow n_\downarrow \qquad (2.1)$$

---

[1] Omit the applied voltage and additional bath term in Eq. (1.2a) for simplicity. The result can be easily generalized to those cases with $\varepsilon_k \to \varepsilon_k + \alpha V(t)/2$ and $\Delta = \sum_\alpha \Delta_\alpha$ [55].

The goal of this chapter is to construct the perturbation expansion in powers of the dot-lead hybridization term $\sum_{k\sigma}(\mathcal{V}_k c^\dagger_{k\sigma} d_\sigma + \mathcal{V}^*_k d^\dagger_\sigma c_{k\sigma})$. In the following, we will first introduce the contour formalism, mainly following the one outlined in [56], in Sec. 2.1 that unifies the equilibrium and nonequilibrium problems to the same framework. We perform explicitly the perturbation theory in case of strong coupling in Sec. 2.2 and discuss semi-analytical approximations (NCA and OCA) to the system in Sec. 2.3.

2.1 Time-dependent problems and the contour idea

The time evolution of a system is governed by the Schrödinger equation:

$$i\frac{d}{dt}\left|\Psi(t)\right\rangle = \hat{H}(t)\left|\Psi(t)\right\rangle \tag{2.2}$$

with $\left|\Psi(t)\right\rangle$ the ket of the system at time t and $\hbar = 1$ in Planck units. The Schrödinger equation is a first-order differential equation in time, and therefore, $\left|\Psi(t)\right\rangle$ is uniquely determined once the initial condition - ket $\left|\Psi(t_0)\right\rangle$ is given. For time-independent Hamiltonians $\hat{H}(t_0) = \hat{H}(t)$ for all times t and the Schrödinger equation is solved by

$$\left|\Psi(t)\right\rangle = e^{-i\hat{H}(t_0)(t-t_0)}\left|\Psi(t_0)\right\rangle \tag{2.3}$$

To generalize Eq. (2.3), we write the general unitary evolution of the ket state as

$$\left|\Psi(t)\right\rangle = \hat{U}(t,t_0)\left|\Psi(t_0)\right\rangle \tag{2.4}$$

In the case of $t > t_0$, with the introduction of *time ordering operator T*, the evolution operator has a compact form:

$$\hat{U}(t, t_0) = T\left\{e^{-i\int_{t_0}^{t} d\bar{t}\ \hat{H}(\bar{t})}\right\} \tag{2.5}$$

$$= \sum_{k=0}^{\infty} \frac{(-1)^k}{k!} \int_{t_0}^{t} dt_1 \int_{t_0}^{t} dt_2 \ldots \int_{t_0}^{t} dt_k\ T\left\{\hat{H}(t_1)\hat{H}(t_2)\ldots\hat{H}(t_k)\right\} \tag{2.6}$$

Similarly, if we introduce the *anti-time ordering operator $\tilde{T}$*, then for $t < t_0$, we have

$$\hat{U}(t, t_0) = \tilde{T}\left\{e^{+i\int_{t}^{t_0} d\bar{t}\ \hat{H}(\bar{t})}\right\} \tag{2.7}$$

The definitions and notations follow from [56].

2.1.1   Forward-Backward Keldysh contour

With the generalized evolution operator, the time-dependent quantum average of an operator $\hat{O}(t)$ at any time t, when the system is prepared in the state $|\Psi(t_0)\rangle \equiv |\Psi_0\rangle$ at time t_0, is given by

$$\langle\hat{O}(t)\rangle = \langle\Psi(t)|\hat{O}(t)|\Psi(t)\rangle = \langle\Psi_0|\hat{U}(t_0, t)\hat{O}(t)\hat{U}(t, t_0)|\Psi_0\rangle \tag{2.8}$$

Inserting the explicit expressions in $\langle\hat{O}(t)\rangle$, we find that

$$\langle\hat{O}(t)\rangle = \langle\Psi_0|\tilde{T}\left\{e^{-i\int_{t}^{t_0} d\bar{t}\ \hat{H}(\bar{t})}\right\}\hat{O}(t)T\left\{e^{-i\int_{t_0}^{t} d\bar{t}\ \hat{H}(\bar{t})}\right\}|\Psi_0\rangle \tag{2.9}$$

If we use Eq. (2.6) and expand the exponentials in powers of the Hamiltonian then a generic term of the expansion consists of integrals over operators at different times looks like

$$\tilde{T}\left\{\hat{H}(t_1')\ldots\hat{H}(t_m')\right\}\hat{O}(t)T\left\{\hat{H}(t_1)\ldots\hat{H}(t_n)\right\} \tag{2.10}$$

where all times $\{t_1\ldots t_n\}$ and $\{t_1'\ldots t_m'\}$ are between t_0 and t. Reading the expression from right to left, we note that $\langle\hat{O}(t)\rangle$ is the overlap between the
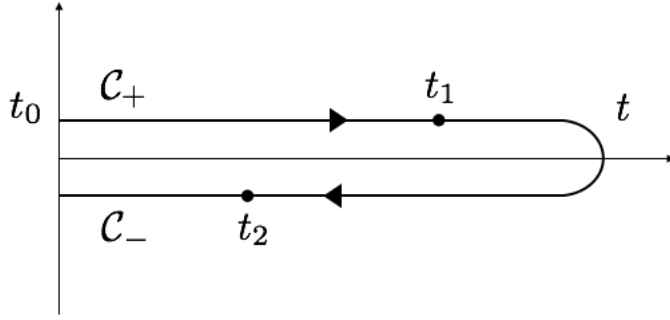
FIGURE 2.1: The forward-backward Keldysh contour in the complex time plane. The contour consists of a forward and a backward branch along the real axis between t_0 and t. According to the orientation the points $t_2 >_{\mathcal{C}} t_1$.

initial bra state $\langle\Psi_0|$ and a ket state obtained by evolving $|\Psi_0\rangle$ from t_0 to t, after which the operator $\hat{O}(t)$ acts and then evolving the ket backward from t to t_0, where the evolution consists of a number of projections of the Hamiltonian $\hat{H}$ at different times in a time-ordered manner along the forward-backward direction. With this general mathematical structure, we can introduce a few new definitions to write the quantity in a more convenient way. First, we define the oriented contour, also known as the forward-backward Keldysh contour, which goes from t_0 to t and then back to t_0. The contour consists of two paths: a forward branch $\mathcal{C}_+$ and a backward branch $\mathcal{C}_-$, as shown in Fig. 2.1. A generic point t_1 can be either on $\mathcal{C}_+$ or on $\mathcal{C}_-$ and once the branch is specified, it can assume any value between t_0 and t. We say that t_2 is later than t_1 or $t_2 >_{\mathcal{C}} t_1$ if t_2 occurs later than t_1 as we walk along the forward-backward direction of the contour. We further define the contour time ordering operator $\mathcal{T}_{\mathcal{C}}$ which moves operators with later contour arguments to the left:

$$\mathcal{T}_{\mathcal{C}}\left\{\hat{A}(t_1)\hat{B}(t_2)\right\} = \begin{cases} \hat{A}(t_1)\hat{B}(t_2) & \text{if } t_1 >_{\mathcal{C}} t_2 \\ \pm\hat{B}(t_2)\hat{A}(t_1) & \text{if } t_1 <_{\mathcal{C}} t_2 \end{cases} \tag{2.11}$$

with the "+" sign is for the case of bosons and "−" sign is for fermions.

With the definition, we can rewrite Eq. (2.10) as

$$\mathcal{T}_{\mathcal{C}}\left\{\hat{H}(t'_1)\dots\hat{H}(t'_m)\hat{O}(t)\hat{H}(t_1)\dots\hat{H}(t_n)\right\} \tag{2.12}$$

28

We can proceed further by introducing the contour integral between two points t_1 and t_2 on the forward-backward Keldysh contour in the same way as the standard integral along any contour [56]. If t_2 is later than t_1 as in Fig. 2.1, then we have

$$\int_{t_1}^{t_2} d\bar{t}\ \hat{A}(\bar{t}) = \int_{t_1}^{t^+} d\bar{t}\ \hat{A}(\bar{t}) + \int_{t^-}^{t_2} d\bar{t}\ \hat{A}(\bar{t}) \tag{2.13}$$

Then Eq. (2.9) takes the elegant form:

$$\langle \hat{O}(t) \rangle = \langle \Psi_0 | \, \mathcal{T}_{\mathcal{C}} \left\{ e^{-i \int_{\mathcal{C}} d\bar{t}\ \hat{H}(\bar{t})} \hat{O}(t) \right\} | \Psi_0 \rangle \tag{2.14}$$

where $\int_{\mathcal{C}}$ denotes the contour integration $\int_{\mathcal{C}_+ \oplus\ \mathcal{C}_-} \equiv \int_{t_0^+}^{t^+} + \int_{t^-}^{t_0^-}$.

2.1.2 Full Keldysh contour

So far we have assumed that the system we are interested in is an isolated system of particles that can be represented by a pure initial state $|\Psi_0\rangle$. In reality, the isolated system is an idealization and it is not possible to completely isolate the system from the surrounding environment. In this way, we need to use the language of quantum statistical physics and assign a probability $w_n \in [0, 1]$ of finding the system at time t_0 in state $|\psi_n\rangle$, the $\sum_n w_n = 0$. The states $|\psi_n\rangle$ may have different energies, momentum, spin and also different numbers of particles. For simplicity, we assume the states $|\psi_n\rangle$ are orthonormal, i.e. $\langle \psi_m | \psi_n \rangle = \delta_{m,n}$, where $\delta_{m,n}$ is the Kronecker delta function. The idea of this approach is to describe the system+environment in terms of the isolated system only and to account for the interaction with the environment through the probability distribution w_n that depends on the features of the environment itself. Then the ensemble average of an operator $\hat{O}(t)$ at the initial time t_0 is defined as

$$\langle \hat{O}(t_0) \rangle = \sum_n w_n \langle \psi_n | \, \hat{O}(t_0) \, | \psi_n \rangle \tag{2.15}$$

and reduces to the quantum average Eq. (2.8) introduced in the case of pure states. This means that if we imagine an ensemble of identical and isolated

systems each in a different pure state $|\psi_n\rangle$, then the quantum average is the result of calculating the weighted sum of the each system $\langle\psi_n|\hat{O}(t_0)|\psi_n\rangle$ with wights w_n. This leads us to introduce a useful quantity called the initial *density matrix operator* $\hat{\rho}_0$ which contains all the statistical information of the initial system at t_0

$$\hat{\rho}_0 = \sum_n w_n |\psi_n\rangle\langle\psi_n| \tag{2.16}$$

Then the ensemble average Eq. (2.15) can be rewritten in terms of $\hat{\rho}_0$ as

$$\langle\hat{O}(t_0)\rangle = \sum_n \left\langle \psi_n \left| \sum_k w_k |\psi_k\rangle\langle\psi_k| \hat{O}(t_0) \right| \psi_n \right\rangle \tag{2.17}$$

$$= \sum_n \left\langle \psi_n \left| \hat{\rho}_0\hat{O}(t_0) \right| \psi_n \right\rangle \tag{2.18}$$

$$= \mathrm{Tr}\left[\hat{\rho}_0\hat{O}(t_0) \right] \tag{2.19}$$

where the symbol Tr denotes a trace over all many-body states. From quantum statistical mechanics, we know that the initial density matrix operator in a canonical ensemble can be written as

$$\hat{\rho}_0 = \sum_n \frac{e^{-\beta E_n}}{Z} |\psi_n\rangle\langle\psi_n| = \frac{e^{-\beta\hat{H}_0}}{Z} \tag{2.20}$$

with $\hat{H}_0 \equiv \hat{H}(t_0)$ and the *partition function*

$$Z \equiv \sum_n e^{-\beta E_n} = \mathrm{Tr}\left[e^{-\beta\hat{H}_0} \right] \tag{2.21}$$

For grand canonical ensembles, just replace $\hat{H}_0$ with $\hat{H}_0 - \mu\hat{N}$ where μ is the chemical potential and $\hat{N}$ is the total number operator for the system. And now we let the system evolve and the quantum average $\langle O(t)\rangle$ at any time t, analogy to Eq. (2.8) reads as

$$\langle\hat{O}(t)\rangle = \sum_n w_n \langle\psi_n| \hat{U}(t_0,t)\hat{O}(t)\hat{U}(t,t_0) |\psi_n\rangle = \mathrm{Tr}\left[\hat{\rho}_0\hat{U}(t_0,t)\hat{O}(t)\hat{U}(t,t_0) \right] \tag{2.22}$$
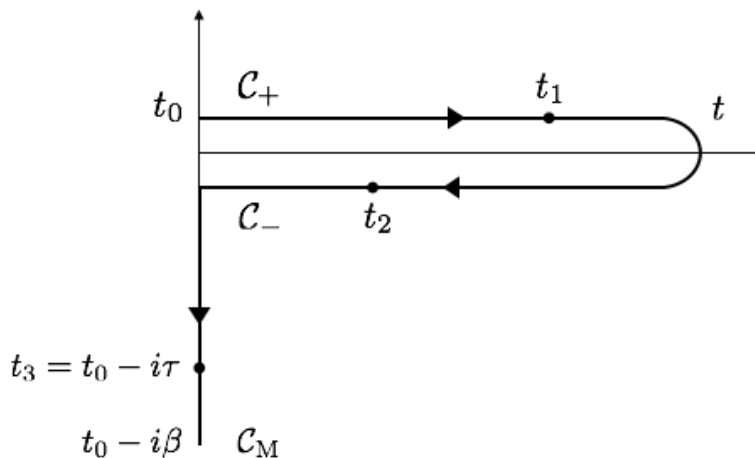
FIGURE 2.2: The full Keldysh contour in the complex time plane. The contour consists of a forward and a backward branch along the real axis between t_0 and t, and an imaginary branch from t_0 to $t_0 - i\beta$ along the imaginary axis . According to the orientation the points $t_3 >_{\mathcal{C}} t_2 >_{\mathcal{C}} t_1$.

We notice the similarity of the exponential form between the time-independent evolution operator Eq. (2.3) and the initial density matrix operator Eq. (2.20), so we unify these two expressions by defining the temperature term $\beta = 1/T$ in the Boltzmann factor (in the Planck units, Boltzmann constant $k_B = 1$) as an imaginary time component $t = t_0 - i\beta$. Then $e^{-\beta \hat{H}_0} = e^{-i\hat{H}_0(t_0 - i\beta - t_0)}$ can be seen as a time propagation from imaginary time t_0 to $t_0 - i\beta$. With this new propagation along the complex path, we add a new imaginary branch $\mathcal{C}_{\mathcal{M}}$ to the forward-backward Keldysh contour and introduce the resulting full (or "L"-shaped) Keldysh contour $\mathcal{C} = \mathcal{C}_+ \oplus \mathcal{C}_- \oplus \mathcal{C}_{\mathrm{M}}$. The full Keldysh contour goes from t_0 to t and then back to t_0 then along imaginary axis to $t_0 - i\beta$. The contour consists of three paths: a forward branch $\mathcal{C}_+$, a backward branch $\mathcal{C}_-$ and a imaginary branch $\mathcal{C}_{\mathrm{M}}$, as shown in Fig. 2.2.

A generic point t_1 can be either on $\mathcal{C}_+$, $\mathcal{C}_-$ or $\mathcal{C}_{\mathrm{M}}$ and once the branch is specified, it can assume any value between t_0 and t, or $t_0 - i\tau$ where $\tau \in [0, \beta]$. Again, we say that t_2 is later than t_1 or $t_2 >_{\mathcal{C}} t_1$ if t_2 occurs later than t_1 as we walk along the forward-backward-imaginary direction of the contour. Similarly, we define

the contour time ordering operator $\mathcal{T}_\mathcal{C}$

$$\mathcal{T}_\mathcal{C}\left\{\hat{A}(t_1)\hat{B}(t_2)\right\} = \begin{cases} \hat{A}(t_1)\hat{B}(t_2) & \text{if } t_1 >_\mathcal{C} t_2 \\ \pm\hat{B}(t_2)\hat{A}(t_1) & \text{if } t_1 <_\mathcal{C} t_2 \end{cases} \tag{2.23}$$

with the "+" sign is for the case of bosons and "−" sign is for fermions, and the additional contour integral along the imaginary branch

$$e^{-\beta\hat{H}_0} = e^{-i\int_{\mathcal{C}_{\mathrm{M}}} d\bar{t}\ \hat{H}(\bar{t})} \tag{2.24}$$

with $\hat{H}(t_0 - i\tau) \equiv \hat{H}(t_0)$. So if t_3 is later than t_1 as in Fig. 2.2, then we have

$$\int_{t_1}^{t_3} d\bar{t}\ \hat{A}(\bar{t}) = \int_{t_1}^{t^+} d\bar{t}\ \hat{A}(\bar{t}) + \int_{t^-}^{t_0^-} d\bar{t}\ \hat{A}(\bar{t}) + \int_{t_0^M}^{t_3} d\bar{t}\ \hat{A}(\bar{t}) \tag{2.25}$$

Then quantum average can be written as the unified form

$$\langle\hat{O}(t)\rangle = \frac{1}{Z}\text{Tr}\left[e^{-\beta\hat{H}_0}\mathcal{T}_\mathcal{C}\left\{e^{-i\int_{\mathcal{C}_+ \oplus \mathcal{C}_-} d\bar{t}\ \hat{H}(\bar{t})}\ \hat{O}(t)\right\}\right] \tag{2.26}$$

$$= \frac{\text{Tr}\left[e^{-\beta\hat{H}_0}\mathcal{T}_\mathcal{C}\left\{e^{-i\int_{\mathcal{C}_+ \oplus \mathcal{C}_-} d\bar{t}\ \hat{H}(\bar{t})}\ \hat{O}(t)\right\}\right]}{\text{Tr}\left[e^{-\beta\hat{H}_0}\right]} \tag{2.27}$$

$$= \frac{\text{Tr}\left[e^{-\beta\hat{H}_0}\mathcal{T}_\mathcal{C}\left\{e^{-i\int_{\mathcal{C}_+ \oplus \mathcal{C}_-} d\bar{t}\ \hat{H}(\bar{t})}\ \hat{O}(t)\right\}\right]}{\text{Tr}\left[e^{-\beta\hat{H}_0}\cdot\mathcal{T}_\mathcal{C}\left\{e^{-i\int_{\mathcal{C}_+ \oplus \mathcal{C}_-} d\bar{t}\ \hat{H}(\bar{t})}\right\}\right]} \tag{2.28}$$

$$= \frac{\text{Tr}\left[\mathcal{T}_\mathcal{C}\left\{e^{-i\int_{\mathcal{C}} d\bar{t}\ \hat{H}(\bar{t})}\ \hat{O}(t)\right\}\right]}{\text{Tr}\left[\mathcal{T}_\mathcal{C}\left\{e^{-i\int_{\mathcal{C}} d\bar{t}\ \hat{H}(\bar{t})}\right\}\right]} \tag{2.29}$$

where from line 2 to line 3 is because of the property of unitary evolution. Now $\int_\mathcal{C}$ includes the contour integration on three branches: $\int_{\mathcal{C}_+} + \int_{\mathcal{C}_-} + \int_{\mathcal{C}_{\mathrm{M}}} \equiv \int_{t_0^+}^{t^+} + \int_{t^-}^{t_0^-} + \int_{t_0^M}^{t_0-i\beta}$. Since in the scope of this thesis, we only care the ordering on the full Keldysh contour, we omit the "full" and call it the Keldysh contour, and omit the subscript $\mathcal{C}$ in $\lessgtr_\mathcal{C}$. In addition, with no loss of generality, we assume $t_0 = 0$. Furthermore, due to the cyclic property of traces, contours $\mathcal{C}_+ \oplus \mathcal{C}_- \oplus \mathcal{C}_M$, $\mathcal{C}_M \oplus \mathcal{C}_+ \oplus \mathcal{C}_-$ and $\mathcal{C}_- \oplus \mathcal{C}_M \oplus \mathcal{C}_+$ are essentially equivalent. For simplicity of

representing the orderings, we use the first one (*Keldysh contour*) and the last one (*twisted Keldysh contour* emerged in Sec. 2.2) for different contexts in this thesis.

2.2 Strong coupling perturbation theory on the Anderson Impurity Model

In this section, we apply the strong coupling perturbation theory explicitly on the Anderson Impurity Model. Again, the Hamiltonian of a dot coupled to the environment reads

$$H = \sum_{k\sigma} \varepsilon_k c_{k\sigma}^\dagger c_{k\sigma} + \sum_{k\sigma} (\mathcal{V}_k c_{k\sigma}^\dagger d_\sigma + \mathcal{V}_k^* d_\sigma^\dagger c_{k\sigma}) + \sum_\sigma \varepsilon_d d_\sigma^\dagger d_\sigma + U n_\uparrow n_\downarrow \qquad (2.30)$$

And we split the Hamiltonian into three parts

$$H = H_{\text{bath}} + H_{\text{hyb}} + H_D \qquad (2.31)$$

where $H_{\text{bath}} = \sum_{k\sigma} \varepsilon_k c_{k\sigma}^\dagger c_{k\sigma}$, $H_{\text{hyb}} = \sum_{k\sigma}(\mathcal{V}_k c_{k\sigma}^\dagger d_\sigma + \mathcal{V}_k^* d_\sigma^\dagger c_{k\sigma})$ and $H_D = \sum_\sigma \varepsilon_d d_\sigma^\dagger d_\sigma + U n_\uparrow n_\downarrow$ and we want to perform the perturbation in terms of the hybridization term H_{hyb} so we further write

$$H = H_0 + H_{\text{hyb}} \qquad (2.32)$$

where $H_0 = H_{\text{bath}} + H_D$ denotes the bare decoupled system. Note that this H_0 is different from the notation used in the previous section where it was $H(t_0)$.

We switch to a path integral representation and introduce the action with the Keldysh formalism as

$$S = \int_{\mathcal{C}} dt \left(\sum_{k\sigma} c_{k\sigma}^*(t) i\partial_t c_{k\sigma}(t) + \sum_\sigma d_\sigma^*(t) i\partial_t d_\sigma(t) - H(t) \right) \qquad (2.33)$$

where we replaced the operators in Heisenberg representation with the respective Grassmann variables and the integration is over the whole Keldysh contour as indicated by $\int_{\mathcal{C}}$. This results in the following expression

$$
S = \int_{\mathcal{C}} dt \left(\sum_{k\sigma} (c^*_{k\sigma}(t)(i\partial_t - \varepsilon_k)c_{k\sigma}(t) - \sum_{k\sigma} (\mathcal{V}_k c^*_{k\sigma}(t)d_\sigma(t) + \mathcal{V}^*_k d^*_\sigma(t)c_{k\sigma}(t)) \right.
$$
$$
\left. + \sum_\sigma d^*_\sigma(t)(i\partial_t - \varepsilon_d)d_\sigma(t) - Un_\uparrow(t)n_\downarrow(t) \right) \tag{2.34}
$$

Now if we discretize time on the Keldysh contour, then the integration on the contour $\int_{\mathcal{C}} dt$, summation over different indices $\sum_{k\sigma}$ can all be condensed into vector-matrix multiplications. Consider a row-vector

$$
c^* = \left(c^*_{k_1\sigma_1}(t_1) \ldots c^*_{k_1\sigma_1}(t_n) c^*_{k_2\sigma_1}(t_1) \ldots c^*_{k_2\sigma_1}(t_n) \ldots c^*_{k_n\sigma_2}(t_n) \right) \tag{2.35}
$$

and column-vector c (same for d^*, d and other multiplying quantities). The action then reads

$$
S = c^* \underbrace{(i\partial_t - \varepsilon_k)}_{G_c^{-1}} c - c^* \mathcal{V} d - d^* \mathcal{V} c + S_D, \tag{2.36}
$$

where we define the nonequilibrium Green's function as the contour-ordered expectation value and the Green's function for the bath electron is

$$
G_c(t, t') = -i \left\langle \mathcal{T}_{\mathcal{C}} \, c(t)c^\dagger(t') \right\rangle_{\text{bath}} \tag{2.37}
$$

and we denote the action of the impurity as S_D

$$
S_D = d^*(i\partial_t - \varepsilon_d)d - U \int_{\mathcal{C}} dt n_\uparrow(t)n_\downarrow(t) \tag{2.38}
$$

We use the Hubbard-Stratonovich transformation twice

$$
e^{d^* AB^{-1}Ad} \det(B) = \int \mathcal{D}c^* \mathcal{D}c \, e^{-c^* Bc - d^* Ac - c^* Ad} \tag{2.39}
$$

First time we choose two matrices A and B to be $A = i\mathcal{V}$ and $B = -iG_c^{-1}$ resulting in $AB^{-1}A = i\mathcal{V}G_c\mathcal{V}$. Thus we define a hybridization function

$$\Delta(t, t') \equiv \mathcal{V}G_c\mathcal{V} = \sum_k \mathcal{V}_k G_c(k; t, t')\mathcal{V}_k \tag{2.40}$$

where $\mathcal{V}_k$ indicates that in general the dot-lead coupling can be momentum-dependent. But in this thesis, we assume $\mathcal{V}_k = \mathcal{V}$ is a real constant. Then after plugging A and B into Eq. (2.39), we have

$$e^{-id^*\Delta d}\det(-iG_c^{-1}) = \int \mathcal{D}c^*\mathcal{D}c \; e^{ic^*G_c^{-1}c - id^*\mathcal{V}c - ic^*\mathcal{V}d} \tag{2.41}$$

Rearranging this expression and plugging the action Eq. (2.36) in, we have

$$\int \mathcal{D}c^*\mathcal{D}c \; e^{iS} = -i\det(G_c^{-1})e^{iS_D}e^{-id^*\Delta d} \tag{2.42}$$

Then we do the second time Hubbard-Stratonovich transformation by choosing $A = i$ and $B = -i\Delta^{-1}$

$$e^{-id^*\Delta d}\det(-i\Delta^{-1}) = \int \mathcal{D}c^*\mathcal{D}c \; e^{ic^*\Delta^{-1}c - id^*c - ic^*d} \tag{2.43}$$

Therefore, we can write

$$\int \mathcal{D}c^*\mathcal{D}c \; e^{iS} = \frac{\det(G_c^{-1})}{\det(\Delta^{-1})} \int \mathcal{D}c^*\mathcal{D}c \; e^{ic^*\Delta^{-1}c - id^*c - ic^*d + iS_D} \tag{2.44}$$

where the factor $\frac{\det(G_c^{-1})}{\det(\Delta^{-1})}$ will enter the expressions for any observable and the partition function, so it will always cancel out with each other. As a consequence, we can ignore it and unify all baths to a single hybridization function Δ and write the effective action as (with $\Delta \neq 0$)

$$\boxed{S = c^*\Delta^{-1}c - d^*c - c^*d + S_D} \tag{2.45}$$

to simplify the notation and we further denote $S = S_{\text{bath}} + S_{\text{hyb}} + S_D$ where $S_{\text{bath}} = c^*\Delta^{-1}c$, $S_{\text{hyb}} = -d^*c - c^*d$ to correspond to different parts in the Hamiltonian

Eq. (2.31).

2.2.1 Second order expansion in coupling

Since the first order term in the expansion of the hybridization term $S_{\text{hyb}} = -d^*c - c^*d$ is zero because our system conserves the number of particles during the evolution, let us do the lowest order - second order expansion to get an idea how general expressions for the average of some local operator $\langle \hat{O}(t) \rangle$ at any time t will look like. Beginning from Eq. (2.29), we get up to second order

$$\langle \hat{O}(t) \rangle = \frac{1}{Z} \text{Tr} \left[\mathcal{T}_\mathcal{C} \left\{ e^{-i \int_\mathcal{C} d\bar{t} \ \hat{H}(\bar{t})} \ \hat{O}(t) \right\} \right] \tag{2.46}$$

$$= \frac{1}{Z} \int_\mathcal{C} \mathcal{D}d^* \mathcal{D}d \mathcal{D}c^* \mathcal{D}c \ O(t) e^{iS} \tag{2.47}$$

$$= \frac{1}{Z} \int_\mathcal{C} \mathcal{D}d^* \mathcal{D}d \mathcal{D}c^* \mathcal{D}c \ e^{ic^* \Delta^{-1} c + iS_D} O(t) \left[1 - \int_\mathcal{C} dt_1 dt_2 d^*(t_1) c(t_1) c^*(t_2) d(t_2) \right] \tag{2.48}$$

$$= \frac{Z_{\text{bath}} Z_D}{Z} \langle \hat{O}(t) \rangle_D - \frac{i}{Z} \int_\mathcal{C} dt_1 dt_2 Z_{\text{bath}} \Delta(t_1, t_2) \int_\mathcal{C} \mathcal{D}d^* \mathcal{D}d e^{iS_D} \left[O(t) d^*(t_1) d(t_2) \right] \tag{2.49}$$

$$= \frac{Z_D}{\tilde{Z}_D} \langle \hat{O}(t) \rangle_D - \frac{i}{\tilde{Z}_D} \int_C dt_1 dt_2 \Delta(t_1, t_2) \text{Tr}_D \left\{ \mathcal{T}_\mathcal{C} \ e^{-\beta \hat{H}_D} \hat{O}(t) \hat{d}^\dagger(t_1) \hat{d}(t_2) \right\} \tag{2.50}$$

where $\cdot_D$ denotes averaging with the bare dot Hamiltonian H_D and partition function $\tilde{Z}_D \equiv Z/Z_{\text{bath}}$ is a dressed partition function of the impurity. There is an implicit sum over spin indices σ in the vector representations of operators: $\Delta = \{\Delta_\sigma\} = \{\Delta_\uparrow, \Delta_\downarrow\}$. Note that all expressions in the path integral form are assumed to be time-ordered, so time-ordering operator $\mathcal{T}_\mathcal{C}$ appears only in the

trace. Writing each configuration of times explicitly, we get

$$\langle O(t) \rangle = \frac{Z_D}{\tilde{Z}_D} \langle O(t) \rangle_D - \frac{iZ_D}{\tilde{Z}_D} \sum_\sigma \Big[\tag{2.51}$$

$$+ \int_0^t dt_2 \int_{t_2}^t dt_1 \langle \hat{O}(t) \hat{d}_\sigma^\dagger(t_1) \hat{d}_\sigma(t_2) \rangle_D \Delta_\sigma(t_1, t_2) \qquad (\text{I}, t_2 < t_1 < t) \tag{2.52}$$

$$+ \int_0^t dt_2 \int_t^{-i\beta} dt_1 \langle \hat{d}_\sigma^\dagger(t_1) \hat{O}(t) \hat{d}_\sigma(t_2) \rangle_D \Delta_\sigma(t_1, t_2) \qquad (\text{II}, t_2 < t < t_1) \tag{2.53}$$

$$+ \int_t^{-i\beta} dt_2 \int_{t_2}^{-i\beta} dt_1 \langle \hat{d}_\sigma^\dagger(t_1) \hat{d}_\sigma(t_2) \hat{O}(t) \rangle_D \Delta_\sigma(t_1, t_2) \qquad (\text{III}, t < t_2 < t_1) \tag{2.54}$$

$$- \int_0^t dt_1 \int_{t_1}^t dt_2 \langle \hat{O}(t) \hat{d}_\sigma(t_2) \hat{d}_\sigma^\dagger(t_1) \rangle_D \Delta_\sigma(t_1, t_2) \qquad (\text{IV}, t_1 < t_2 < t) \tag{2.55}$$

$$- \int_0^t dt_1 \int_t^{-i\beta} dt_2 \langle \hat{d}_\sigma(t_2) \hat{O}(t) \hat{d}_\sigma^\dagger(t_1) \rangle_D \Delta_\sigma(t_1, t_2) \qquad (\text{V}, t_1 < t < t_2) \tag{2.56}$$

$$- \int_t^{-i\beta} dt_1 \int_{t_1}^{-i\beta} dt_2 \langle \hat{d}_\sigma(t_2) \hat{d}_\sigma^\dagger(t_1) \hat{O}(t) \rangle_D \Delta_\sigma(t_1, t_2) \Big] \qquad (\text{VI}, t < t_1 < t_2) \tag{2.57}$$

Again, note that all of the integrals are contour integrals. And $\tilde{Z}_D$ also needs to be evaluated separately. Similarly, it reads

$$\tilde{Z}_D = Z_D - i \sum_\sigma \int_\mathcal{C} dt_1 dt_2 \Delta_\sigma(t_1, t_2) \text{Tr}_D \Big\{ \mathcal{T}_\mathcal{C} \ e^{-\beta \hat{H}_D} \hat{d}_\sigma^\dagger(t_1) \hat{d}_\sigma(t_2) \Big\} \tag{2.58}$$

2.2.1.1 Atomic propagators

The correction to the bare partition function of the dot $\delta Z_D = \tilde{Z}_D - Z_D$ reads for $t_1 > t_2$

$$\delta Z_D^{(\mathrm{I})} = -i \sum_\sigma \int_0^{-i\beta} dt_1 \int_0^{t_1} dt_2 \Delta_\sigma(t_1, t_2) \mathrm{Tr}_D \left\{ e^{-\beta \hat{H}_D} e^{i\hat{H}_D t_1} \hat{d}_\sigma^\dagger e^{-i\hat{H}_D t_1} e^{i\hat{H}_D t_2} \hat{d}_\sigma e^{-i\hat{H}_D t_2} \right\}$$

(2.59)

Note that the evolution term $e^{-i\hat{H}t}$ is a symbolic form for the general case $\mathcal{T}_C \left\{ e^{-i \int_C d\bar{t}\, \hat{H}(\bar{t})} \right\}$ as we developed in Sec. 2.1 and it is solely for the purpose of simplicity of notations. Therefore, the derivation is valid for general time-dependent problems. Now using the cyclic property of trace, the last expression reads:

$$\delta Z_D^{(\mathrm{I})} = -i \sum_\sigma \int_0^{-i\beta} dt_1 \int_0^{t_1} dt_2 \Delta_\sigma(t_1, t_2) \sum_j \langle j \left| e^{-\beta \hat{H}_D} e^{i\hat{H}_D t_1} \hat{d}_\sigma^\dagger e^{-i\hat{H}_D t_1} e^{i\hat{H}_D t_2} \hat{d}_\sigma e^{-i\hat{H}_D t_2} \right| j \rangle$$

(2.60)

where $|j\rangle$ is one of the basis states of the impurity and it is useful to consider $\hat{d}_\sigma$ as a matrix in $|j\rangle$ space. Then the last expression is rewritten as

$$\delta Z_D^{(\mathrm{I})} = -\sum_\sigma \int_0^{-i\beta} dt_1 \int_0^{t_1} dt_2 \Delta_\sigma(t_1, t_2) \sum_j \langle j \left| \hat{p}(t_2, 0^+) \hat{p}(-i\beta, t_1) \hat{d}_\sigma^\dagger \hat{g}(t_1, t_2) \hat{d}_\sigma \right| j \rangle$$

(2.61)

where we have introduced *atomic propagators* as

$$\hat{p}(t_1, t_2)_{s_1 s_2} = \begin{cases} -i \left\langle s_1 \left| e^{-i\hat{H}_D t_1} e^{i\hat{H}_D t_2} \right| s_2 \right\rangle & t_1 > t_2 \\ -i \langle s_1 | \hat{\xi} e^{-i\hat{H}_D t_1} e^{-\beta \hat{H}_D} e^{i\hat{H}_D t_2} | s_2 \rangle = i\hat{\xi} \left[\hat{p}(t_1, 0) \hat{p}(-i\beta, t_2) \right]_{s_1 s_2} & t_1 < t_2 \end{cases}$$

(2.62)

and corresponding matrix in the basis space of dot as $\hat{p}$. We have also introduced operator $\hat{\xi} = (-1)^{\hat{N}}$, where $\hat{N}$ measures the number of electrons in the state. We introduce diagonal matrix $\hat{1} = \hat{\xi}^2$ into the trace and use $[\hat{\xi}, \hat{H}] = 0$ and $[\hat{\xi}, \hat{p}] = 0$ because our system does not flip the states at the beginning and at the end. The

following relation holds : $\hat{d}\hat{\xi} = -\hat{\xi}\hat{d}$. Then

$$\delta Z_D^{(\mathrm{I})} = i\sum_\sigma \int_0^{-i\beta} dt_1 \int_0^{t_1} dt_2 \Delta_\sigma(t_1, t_2) \sum_j \langle j \left| \hat{\xi}\hat{p}(t_2, t_1)\hat{d}_\sigma^\dagger \hat{g}(t_1, t_2)\hat{d}_\sigma \right| j\rangle \quad (2.63)$$

The second correction to the partition function (at $t_1 < t_2$) can be obtained in an analogous way and reads

$$\delta Z_D^{(\mathrm{II})} = \sum_\sigma \int_0^{-i\beta} dt_2 \int_0^{t_2} dt_1 \Delta_\sigma(t_1, t_2) \sum_j \langle j \left| \hat{p}(t_1, 0^+)\hat{p}(-i\beta, t_2)\hat{d}\hat{p}(t_2, t_1)\hat{d}_\sigma^\dagger \right| j\rangle$$

$$(2.64)$$

Since we integrate over t_1 and t_2, we can swap them in the second expression and get

$$\delta Z_D^{(\mathrm{II})} = -i\sum_\sigma \int_0^{-i\beta} dt_1 \int_0^{t_1} dt_2 \Delta_\sigma(t_2, t_1) \sum_j \langle j \left| \hat{\xi}\hat{p}(t_2, t_1)\hat{d}\hat{p}(t_1, t_2)\hat{d}_\sigma^\dagger \right| j\rangle \quad (2.65)$$

Combine these two cases and we now get the total correction to the dot partition function as

$$\delta Z_D = i\sum_\sigma \int_0^{-i\beta} dt_1 \int_0^{t_1} dt_2 \sum_j \langle j \left| \hat{\xi}\hat{p}(t_2, t_1) \left(\hat{d}_\sigma^\dagger \hat{p}(t_1, t_2)\Delta_\sigma(t_1, t_2)\hat{d}_\sigma - \hat{d}_\sigma \hat{p}(t_1, t_2)\Delta_\sigma(t_2, t_1)\hat{d}_\sigma^\dagger \right) \right| j\rangle$$

$$(2.66)$$

Introducing now "*self-energy*" as

$$\hat{\mathfrak{S}}(t_1, t_2) = i\sum_\sigma \left(\hat{d}_\sigma^\dagger \hat{p}(t_1, t_2)\Delta_\sigma(t_1, t_2)\hat{d}_\sigma - \hat{d}_\sigma \hat{p}(t_1, t_2)\Delta_\sigma(t_2, t_1)\hat{d}_\sigma^\dagger \right) \quad (2.67)$$

we get

$$\delta Z_D = \int_{\mathcal{C}} dt_1 \int_0^{t_1} dt_2 \sum_j \langle j \left| \hat{\xi}\hat{p}(t_2, t_1)\hat{\mathfrak{S}}(t_1, t_2) \right| j\rangle \quad (2.68)$$

2.2.1.2 Local operator averages

The correction to the partition function is known. Now, let us continue with the expression of the second-order correction to the $\langle \hat{O}(t)\rangle$: $\langle \delta\hat{O}(t)\rangle^{(2)} = \langle \hat{O}(t)\rangle -$

$\langle \hat{O}(t) \rangle_D$. It reads:

$$i\tilde{Z}_D \langle \delta\hat{O}(t) \rangle^{(2)} = \sum_\sigma \sum_j \Big[\tag{2.69}$$

$$-i \int_0^t dt_1 \int_0^{t_1} dt_2 \langle j | \hat{\xi}\hat{p}(t_2,t)\hat{O}\hat{p}(t,t_1)\hat{d}_\sigma^\dagger \hat{p}(t_1,t_2)\hat{d}_\sigma | j \rangle \Delta_\sigma(t_1,t_2) \qquad (\mathrm{I}, t_2 < t_1 < t) \tag{2.70}$$

$$-i \int_0^t dt_2 \int_t^{-i\beta} dt_1 \langle j | \hat{\xi}\hat{p}(t_2,t_1)\hat{d}_\sigma^\dagger \hat{p}(t_1,t)\hat{O}\hat{p}(t,t_2)\hat{d}_\sigma | j \rangle \Delta_\sigma(t_1,t_2) \qquad (\mathrm{II}, t_2 < t < t_1) \tag{2.71}$$

$$-i \int_t^{t_1} dt_2 \int_t^{-i\beta} dt_1 \langle j | \hat{\xi}\hat{p}(t,t_1)\hat{d}_\sigma^\dagger \hat{p}(t_1,t_2)\hat{d}_\sigma \hat{p}(t_2,t)\hat{O} | j \rangle \Delta_\sigma(t_1,t_2) \qquad (\mathrm{III}, t < t_2 < t_1) \tag{2.72}$$

$$+i \int_0^t dt_2 \int_0^{t_2} dt_1 \langle j | \hat{\xi}\hat{p}(t_1,t)\hat{O}\hat{p}(t,t_2)\hat{d}_\sigma \hat{p}(t_2,t_1)\hat{d}_\sigma^\dagger | j \rangle \Delta_\sigma(t_1,t_2) \qquad (\mathrm{IV}, t_1 < t_2 < t) \tag{2.73}$$

$$+i \int_t^{-i\beta} dt_2 \int_0^t dt_1 \langle j | \hat{\xi}\hat{p}(t_1,t_2)\hat{d}_\sigma \hat{p}(t_2,t)\hat{O}\hat{p}(t,t_1)\hat{d}_\sigma^\dagger | j \rangle \Delta_\sigma(t_1,t_2) \qquad (\mathrm{V}, t_1 < t < t_2) \tag{2.74}$$

$$+i \int_t^{t_2} dt_1 \int_{t_1}^{-i\beta} dt_2 \langle j | \hat{\xi}\hat{p}(t,t_2)\hat{d}_\sigma \hat{p}(t_2,t_1)\hat{d}_\sigma^\dagger \hat{p}(t_1,t)\hat{O} | j \rangle \Delta_\sigma(t_1,t_2) \Big] \qquad (\mathrm{VI}, t < t_1 < t_2) \tag{2.75}$$

We swap t_1 and t_2 wherever there is $\hat{p}(t_2, t_1)$, do cyclic permutation to get $\hat{d}\hat{p}(t_1, t_2)\hat{d}^\dagger$ and move $\hat{\xi}$ to the beginning of each term, then we get

$$i\tilde{Z}_D \langle \delta\hat{O}(t)\rangle^{(2)} = \sum_\sigma \sum_j \Big[\tag{2.76}$$

$$-i \int_0^t dt_1 \int_0^{t_1} dt_2 \langle j \big| \hat{\xi}\hat{p}(t_2, t)\hat{O}\hat{p}(t, t_1)\hat{d}_\sigma^\dagger \hat{p}(t_1, t_2)\hat{d}_\sigma \big| j\rangle \Delta_\sigma(t_1, t_2) \qquad (\mathrm{I}, t_2 < t_1 < t)$$

$$\tag{2.77}$$

$$+i \int_0^t dt_1 \int_t^{-i\beta} dt_2 \langle j \big| \hat{\xi}\hat{d}_\sigma \hat{p}(t_1, t_2)\hat{d}_\sigma^\dagger \hat{p}(t_2, t)\hat{O}\hat{p}(t, t_1) \big| j\rangle \Delta_\sigma(t_2, t_1) \qquad (\mathrm{II}, t_1 < t < t_2)$$

$$\tag{2.78}$$

$$-i \int_t^{-i\beta} dt_1 \int_t^{t_1} dt_2 \langle j \big| \hat{\xi}\hat{p}(t, t_1)\hat{d}_\sigma^\dagger \hat{p}(t_1, t_2)\hat{d}_\sigma \hat{p}(t_2, t)\hat{O} \big| j\rangle \Delta_\sigma(t_1, t_2) \qquad (\mathrm{III}, t < t_2 < t_1)$$

$$\tag{2.79}$$

$$+i \int_0^t dt_1 \int_0^{t_1} dt_2 \langle j \big| \hat{\xi}\hat{p}(t_2, t)\hat{O}\hat{p}(t, t_1)\hat{d}_\sigma \hat{p}(t_1, t_2)\hat{d}_\sigma^\dagger \big| j\rangle \Delta_\sigma(t_2, t_1) \qquad (\mathrm{IV}, t_2 < t_1 < t)$$

$$\tag{2.80}$$

$$-i \int_0^t dt_1 \int_t^{-i\beta} dt_2 \langle j \big| \hat{\xi}\hat{d}_\sigma^\dagger \hat{p}(t_1, t_2)\hat{d}_\sigma \hat{p}(t_2, t)\hat{O}\hat{p}(t, t_1) \big| j\rangle \Delta_\sigma(t_1, t_2) \qquad (\mathrm{V}, t_1 < t < t_2)$$

$$\tag{2.81}$$

$$+i \int_t^{-i\beta} dt_1 \int_t^{t_1} dt_2 \langle j \big| \hat{\xi}\hat{p}(t, t_1)\hat{d}_\sigma \hat{p}(t_1, t_2)\hat{d}_\sigma^\dagger \hat{p}(t_2, t)\hat{O} \big| j\rangle \Delta_\sigma(t_2, t_1) \Big] \qquad (\mathrm{VI}, t < t_2 < t_1)$$

$$\tag{2.82}$$

Joining now the parts with the same integration limits we obtain

$$i\tilde{Z}_D\langle\delta\hat{O}(t)\rangle^{(2)} = \sum_\sigma\sum_j\Big[\tag{2.83}$$

$$-i\int_0^t dt_1\int_0^{t_1} dt_2\langle j\Big|\hat{\xi}\hat{p}(t_2,t)\hat{O}\hat{p}(t,t_1)\left(\hat{d}_\sigma^\dagger\hat{p}(t_1,t_2)\Delta_\sigma(t_1,t_2)\hat{d}_\sigma - \hat{d}_\sigma\hat{p}(t_1,t_2)\Delta_\sigma(t_2,t_1)\hat{d}_\sigma^\dagger\right)\Big|j\rangle \tag{2.84}$$

$$(\text{I},t_2<t_1<t)$$

$$-i\int_0^t dt_1\int_t^{-i\beta} dt_2\langle j\Big|\hat{\xi}\left(\hat{d}_\sigma^\dagger\hat{p}(t_1,t_2)\Delta_\sigma(t_1,t_2)\hat{d}_\sigma - \hat{d}_\sigma\hat{p}(t_1,t_2)\Delta_\sigma(t_2,t_1)\hat{d}_\sigma^\dagger\right)\hat{p}(t_2,t)\hat{O}\hat{p}(t,t_1)\Big|j\rangle \tag{2.85}$$

$$(\text{II},t_1<t<t_2)$$

$$-i\int_t^{-i\beta} dt_1\int_t^{t_1} dt_2\langle j\Big|\hat{\xi}\hat{p}(t,t_1)\left(\hat{d}_\sigma^\dagger\hat{p}(t_1,t_2)\Delta_\sigma(t_1,t_2)\hat{d}_\sigma - \hat{d}_\sigma\hat{p}(t_1,t_2)\Delta_\sigma(t_2,t_1)\hat{d}_\sigma^\dagger\right)\hat{p}(t_2,t)\hat{O}\Big|j\rangle\Big]$$

$$(\text{III},t<t_2<t_1) \tag{2.86}$$

Substituting the "self-energy" $\hat{\mathfrak{S}}$ from Eq. (2.67), we get

$$i\tilde{Z}_D\langle\delta\hat{O}(t)\rangle^{(2)} = \sum_j\Big[\tag{2.87}$$

$$-\langle j\Big|\int_0^t dt_1\int_0^{t_1} dt_2\ \hat{\xi}\hat{p}(t_2,t)\hat{O}\hat{p}(t,t_1)\hat{\mathfrak{S}}(t_1,t_2)\Big|j\rangle \qquad (\text{I},t_2<t_1<t) \tag{2.88}$$

$$-\langle j\Big|\int_0^t dt_1\int_t^{-i\beta} dt_2\ \hat{\xi}\hat{\mathfrak{S}}(t_1,t_2)\hat{p}(t_2,t)\hat{O}\hat{p}(t,t_1)\Big|j\rangle \qquad (\text{II},t_1<t<t_2) \tag{2.89}$$

$$-\langle j\Big|\int_t^{-i\beta} dt_1\int_t^{t_1} dt_2\ \hat{\xi}\hat{p}(t,t_1)\hat{\mathfrak{S}}(t_1,t_2)\hat{p}(t_2,t)\hat{O}\Big|j\rangle\Big] \qquad (\text{III},t<t_2<t_1) \tag{2.90}$$

Using $[\hat{\xi},\hat{p}]=0$ and $[\hat{\xi},\hat{O}]=0$ (since $[\hat{x},\hat{H}]=0$) we get

$$i\tilde{Z}_D\langle\delta\hat{O}(t)\rangle^{(2)} = \sum_j\Big[\tag{2.91}$$

$$-\langle j\Big|\int_0^t dt_1\int_0^{t_1} dt_2\ \hat{\xi}\hat{p}(t,t_1)\hat{\mathfrak{S}}(t_1,t_2)\hat{p}(t_2,t)\hat{O}\Big|j\rangle \qquad (\text{I},t_2<t_1<t) \tag{2.92}$$

$$-\langle j\Big|\int_0^t dt_1\int_t^{-i\beta} dt_2\ \hat{\xi}\hat{p}(t,t_1)\hat{\mathfrak{S}}(t_1,t_2)\hat{p}(t_2,t)\hat{O}\Big|j\rangle \qquad (\text{II},t_1<t<t_2) \tag{2.93}$$

$$-\langle j\Big|\int_t^{-i\beta} dt_1\int_t^{t_1} dt_2\ \hat{\xi}\hat{p}(t,t_1)\hat{\mathfrak{S}}(t_1,t_2)\hat{p}(t_2,t)\hat{O}\Big|j\rangle\Big] \qquad (\text{III},t<t_2<t_1) \tag{2.94}$$

Finally we get

$$\langle \delta \hat{O}(t) \rangle^{(2)} = \frac{i}{\tilde{Z}_D} \text{Tr}_D \left\{ \hat{\xi} \hat{p} \circlearrowright \hat{\mathfrak{S}} \circlearrowright \hat{p} \hat{O} \right\} \tag{2.95}$$

where the *convolution operator* on the Keldysh contour is defined as

$$[a \circlearrowright b](t_1, t_2) = \begin{cases} \int_{t_2}^{t_1} dt' a(t_1, t') b(t', t_2) & t_1 > t_2 \\ \int_{t_2}^{-i\beta} dt' a(t_1, t') b(t', t_2) + \int_0^{t_1} dt' a(t_1, t') b(t', t_2) & t_1 < t_2 \end{cases} \tag{2.96}$$

which results in a *Dyson's equation* of the dressed propagator $\hat{P}$ up to the second order in the following form

$$P = p + p \circlearrowright \mathfrak{S} \circlearrowright p \tag{2.97}$$

So at the end, we arrive to

$$\langle \hat{O}(t) \rangle = \frac{i}{\tilde{Z}_D} \text{Tr}_D \left\{ \hat{\xi} \hat{P}(t_+, t_-) \hat{O} \right\} \tag{2.98}$$

where the dressed propagator is going from t_-, the time t on $\mathcal{C}_-$ to t_+, the time t on $\mathcal{C}_+$. Note that this expression and the Dyson's equation defines the direction of the propagators on the Keldysh contour that we need to evaluate: $t_- \to 0_- \to 0_M \to -i\beta \to 0_+ \to t_+$, as shown in Fig. 2.3. We call this the *twisted contour ordering* and denote $t_- \prec 0_- \prec 0_M \prec -i\beta \prec 0_+ \prec t_+$. It is a direct consequence of the fact that there is always a physical measurement at time t, i.e. a projection onto atomic states of the impurity, also indicated by the last equation where operator $\hat{O}$ at time t is arranged on the right-most side in the trace. Notice the distinction between this and the Keldysh contour ordering.
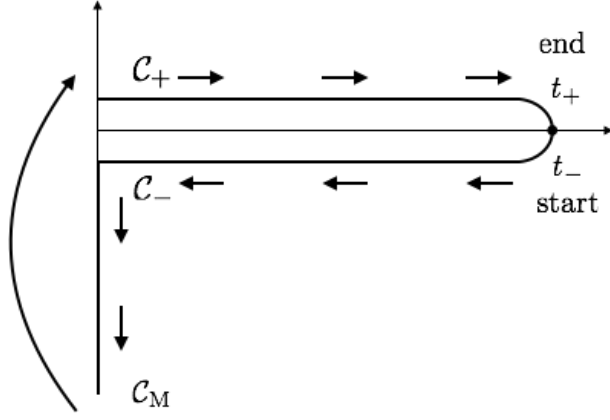
FIGURE 2.3: The twisted contour ordering in the complex time plane. The starting point is t_- and the end point is t_+ and follows the direction $t_- \to 0_- \to 0_M \to -i\beta \to 0_+ \to t_+$. And we denote $t_- \prec 0_- \prec 0_M \prec -i\beta \prec 0_+ \prec t_+$.

2.2.2 Fourth order expansion in coupling

The purpose of this section is to check the behavior of the fourth order expansion in coupling to get an idea how the signs work out:

$$\langle \hat{O}(t) \rangle = \frac{1}{Z} \int \mathcal{D}d^* \mathcal{D}d \mathcal{D}c^* \mathcal{D}c \, O(t) e^{iS} \tag{2.99}$$

$$= \frac{1}{Z} \int \mathcal{D}d^* \mathcal{D}d \mathcal{D}c^* \mathcal{D}c \, e^{ic^* \Delta^{-1} c + iS_D} O(t)$$

$$\cdot \left[1 + 2^{nd} \text{ order} + \int_C dt_1 dt_2 dt_3 dt_4 d^*(t_1) c(t_1) c^*(t_2) d(t_2) d^*(t_3) c(t_3) c^*(t_4) d(t_4) \right] \tag{2.100}$$

$$\langle \delta \hat{O}(t) \rangle^{(4)} = \frac{1}{Z} \int_C dt_1 dt_2 dt_3 dt_4 \left(\int \mathcal{D}c^* \mathcal{D}c \, c(t_1) c^*(t_2) c(t_3) c^*(t_4) e^{ic^* \Delta^{-1} c} \right)$$

$$\cdot \left(\int \mathcal{D}d^* \mathcal{D}d \, O(t) d^*(t_1) d(t_2) d^*(t_3) d(t_4) e^{iS_D} \right) \tag{2.101}$$

We look at the bath term first. Since it is non-interacting, we could make use of Wick's theorem

$$\int \mathcal{D}c^* \mathcal{D}c \, c(t_1) c^*(t_2) c(t_3) c^*(t_4) e^{ic^* \Delta^{-1} c} \tag{2.102}$$

$$= Z_{\text{bath}} \cdot \Delta(t_1, t_3; t_4, t_2) \tag{2.103}$$

$$= Z_{\text{bath}} \cdot [\Delta(t_1, t_4) \cdot \Delta(t_3, t_2) - \Delta(t_1, t_2) \cdot \Delta(t_3, t_4)] \tag{2.104}$$

Then the fourth order correction is given by

$$\langle \delta \hat{O}(t) \rangle^{(4)} = - \frac{Z_{\text{bath}}}{Z} \int_C dt_1 dt_2 dt_3 dt_4 \Delta(t_1, t_2) \cdot \Delta(t_3, t_4) \text{Tr}_D \left\{ \mathcal{T}_C e^{-\beta \hat{H}_D} \hat{O}(t) \hat{d}^\dagger(t_1) \hat{d}(t_2) \hat{d}^\dagger(t_3) \hat{d}(t_4) \right\}$$

(2.105)

$$+ \frac{Z_{\text{bath}}}{Z} \int_C dt_1 dt_2 dt_3 dt_4 \Delta(t_1, t_4) \cdot \Delta(t_3, t_2) \text{Tr}_D \left\{ \mathcal{T}_C e^{-\beta \hat{H}_D} \hat{O}(t) \hat{d}^\dagger(t_1) \hat{d}(t_2) \hat{d}^\dagger(t_3) \hat{d}(t_4) \right\}$$

(2.106)

We investigate only one possibility of the first term. When $t_4 < t_3 < t_2 < t_1 < t$ (I), we get

$$\langle \delta \hat{O}(t) \rangle^{(4)(\text{I})} = - \frac{1}{\tilde{Z}_D} \sum_\sigma \sum_j \int_{\mathcal{C}_{(\text{I})}} dt_1 dt_2 dt_3 dt_4 \Delta_\sigma(t_1, t_2) \cdot \Delta_\sigma(t_3, t_4) \tag{2.107}$$

$$\cdot \left\langle j \left| e^{-\beta \hat{H}_D} \hat{O}(t) \hat{d}_\sigma^\dagger(t_1) \hat{d}_\sigma(t_2) \hat{d}_\sigma^\dagger(t_3) \hat{d}_\sigma(t_4) \right| j \right\rangle \tag{2.108}$$

$$= - \frac{i}{\tilde{Z}_D} \sum_\sigma \sum_j \int_{\mathcal{C}_{(\text{I})}} dt_1 dt_2 dt_3 dt_4 \Delta_\sigma(t_1, t_2) \cdot \Delta_\sigma(t_3, t_4) \tag{2.109}$$

$$\cdot \left\langle j \left| \hat{\xi} \hat{p}(t_4, t) \hat{O} \hat{p}(t, t_1) \hat{d}_\sigma^\dagger \hat{p}(t_1, t_2) \hat{d}_\sigma \hat{p}(t_2, t_3) \hat{d}_\sigma^\dagger \hat{p}(t_3, t_4) \hat{d}_\sigma \right| j \right\rangle \tag{2.110}$$

$$= - \frac{i}{\tilde{Z}_D} \sum_\sigma \sum_j \int_{\mathcal{C}_{(\text{I})}} dt_1 dt_2 dt_3 dt_4 \tag{2.111}$$

$$\cdot \left\langle j \left| \hat{\xi} \hat{p}(t, t_1) \underbrace{\hat{d}_\sigma^\dagger \Delta_\sigma(t_1, t_2) \hat{p}(t_1, t_2) \hat{d}_\sigma}_{-i\hat{\mathfrak{S}}(t_1, t_2)} \hat{p}(t_2, t_3) \underbrace{\hat{d}_\sigma^\dagger \Delta_\sigma(t_3, t_4) \hat{p}(t_3, t_4) \hat{d}_{\sigma_1}}_{-i\hat{\mathfrak{S}}(t_3, t_4)} \hat{p}(t_4, t) \hat{O} \right| j \right\rangle$$

(2.112)

where the last step we used the commutation relation $[\hat{\xi}, \hat{p}] = 0$ and $\hat{d}\hat{\xi} = -\hat{\xi}\hat{d}$. Now imagine we combine this term with the cases $t_4 < t_3 < t_1 < t_2 < t$ ($\mathcal{C}_{(\text{II})}$), $t_3 < t_4 < t_2 < t_1 < t$ ($\mathcal{C}_{(\text{III})}$) and $t_1 < t_2 < t_3 < t_4 < t$ ($\mathcal{C}_{(\text{IV})}$) and all other possibility that do not involve crossings of hybridization lines, which are the cases we care in the next section Sec. 2.3, we will get exactly the correction expressed in terms of the "self-energy" as:

$$\langle \delta O(t) \rangle^{(4)}_{(\text{NCA})} = \frac{i}{\tilde{Z}_D} \text{Tr} \left\{ \hat{\xi} \hat{p} \circlearrowright \hat{\mathfrak{S}} \circlearrowright \hat{p} \circlearrowright \hat{\mathfrak{S}} \circlearrowright \hat{p} \hat{O} \right\} \tag{2.113}$$

2.3 Self-consistent approximations

2.3.1 Non-crossing approximation (NCA)

Apparently calculating the full expansion of the observable $\langle \hat{O}(t) \rangle$ that we are interested analytically is not feasible. Instead, we can sum part of the terms self-consistently. So in this section, we develop the simplest self-consistent skeleton approximation that is called non-crossing approximation (NCA) [57]. And in the next chapter, we will know that this approximation corresponds to summing all the terms (diagrams) without crossing of conduction-electron lines in the original perturbation. It is generated by writing the Dyson's equation Eq. (2.97) with dressed propagators. We have

$$P = p + p \circlearrowleft \mathfrak{S}_{\text{NCA}} \circlearrowleft P \tag{2.114}$$

$$\hat{\mathfrak{S}}_{\text{NCA}}(t_1, t_2) = i \sum_\sigma \left(\hat{d}^\dagger_\sigma \hat{P}(t_1, t_2) \Delta_\sigma(t_1, t_2) \hat{d}_\sigma - \hat{d}_\sigma \hat{P}(t_1, t_2) \Delta_\sigma(t_2, t_1) \hat{d}^\dagger_\sigma \right) \tag{2.115}$$

As we have seen in the second and fourth order expansions, a higher order correction to P would generate an expression of this form: $\ldots p \circlearrowleft \mathfrak{S} \circlearrowleft p \circlearrowleft \mathfrak{S} \circlearrowleft \ldots$. The convolution operator $\circlearrowleft$ guarantees the contour-ordering of the arguments, so that every $\mathfrak{S}$ "ends" before the next one starts. In either bare Hamiltonian H_0 or NCA, the atomic propagators (p or P) do not change the state of the impurity, that is, only the diagonal elements in $\hat{p}$ and $\hat{P}$ are non-zero. Consequently, $\hat{\mathfrak{S}}$ is also a diagonal matrix. Let's define

$$P_{|s\rangle}(t_1, t_2) \equiv \left\langle s \left| \hat{P}(t_1, t_2) \right| s \right\rangle \tag{2.116}$$

$$\mathfrak{S}_{|s\rangle}(t_1, t_2) \equiv \left\langle s \left| \hat{\mathfrak{S}}(t_1, t_2) \right| s \right\rangle \tag{2.117}$$

for each impurity state $|s\rangle$ ($s = 0, \uparrow, \downarrow, \uparrow\downarrow$). Then

- $|s = 0\rangle$ state

$$\mathfrak{S}_{|0\rangle}(t_1, t_2) = i \left(-\Delta_{|\uparrow\rangle}(t_2, t_1) \cdot P_{|\uparrow\rangle}(t_1, t_2) - \Delta_{|\downarrow\rangle}(t_2, t_1) \cdot P_{|\downarrow\rangle}(t_1, t_2) \right)$$

(2.118)

- $|s = \uparrow\rangle$ state

$$\mathfrak{S}_{|\uparrow\rangle}(t_1, t_2) = i \left(+\Delta_{|\uparrow\rangle}(t_1, t_2) \cdot P_{|0\rangle}(t_1, t_2) - \Delta_{|\downarrow\rangle}(t_2, t_1) \cdot P_{|\uparrow\downarrow\rangle}(t_1, t_2) \right)$$

(2.119)

- $|s = \downarrow\rangle$ state

$$\mathfrak{S}_{|\downarrow\rangle}(t_1, t_2) = i \left(+\Delta_{|\downarrow\rangle}(t_1, t_2) \cdot P_{|0\rangle}(t_1, t_2) - \Delta_{|\uparrow\rangle}(t_2, t_1) \cdot P_{|\uparrow\downarrow\rangle}(t_1, t_2) \right)$$

(2.120)

- $|s = \uparrow\downarrow\rangle$ state

$$\mathfrak{S}_{|\uparrow\downarrow\rangle}(t_1, t_2) = i \left(+\Delta_{|\uparrow\rangle}(t_1, t_2) \cdot P_{|\downarrow\rangle}(t_1, t_2) + \Delta_{|\downarrow\rangle}(t_1, t_2) \cdot P_{|\uparrow\rangle}(t_1, t_2) \right)$$

(2.121)

And for the propagators P, in integral form explicitly as

$$P_{|s\rangle}^{(d)}(t_1, t_2) = p_{|s\rangle}(t_1, t_2) + \int_{t_2}^{t_1} d\eta_1 \int_{t_2}^{\eta_1} d\eta_2 p_{|s\rangle}(t_1, \eta_1) \, \mathfrak{S}_{|s\rangle}^{(d)}(\eta_1, s_2) \, P_{|s\rangle}^{(d-1)}(\eta_2, t_2)$$

(2.122)

$$= p_{|s\rangle}(t_1, t_2) + \int_{t_2}^{t_1} d\eta_1 p_{|s\rangle}(t_1, \eta_1) \left(\int_{t_2}^{\eta_1} d\eta_2 \mathfrak{S}_{|s\rangle}^{(d)}(\eta_1, \eta_2) \, P_{|s\rangle}^{(d-1)}(\eta_2, t_2) \right)$$

(2.123)

$$= p_{|s\rangle}(t_1, t_2) + \int_{t_2}^{t_1} d\eta_1 p_{|s\rangle}(t_1, \eta_1) \left(I_{|s\rangle}^{(d)}(\eta_1, t_2) \right)$$

(2.124)

where $I_{|s\rangle}^{(d)}(\eta_1, t_2)$ is the intermediate quantity and be aware of the constraint for the time points $t_1 \succ \eta_1 \succ \eta_2 \succ t_2$. Therefore, a NCA solution is obtained by summing over NCA terms via a Dyson equation. It involves an iterative procedure and self-consistently converges to a semi-analytic solution. More details can be found in [58].

2.3.2 One-crossing approximation (OCA)

The next order self-consistent approximate method is the one-crossing approximation (OCA) [59, 60]. Previously, we looked into the behavior of the fourth order perturbation in the aspect of NCA. There, we dropped out all the terms that include hybridization lines crossings. Now we would like to bring them back and include them as the next-order terms. Here we will omit the derivation and state only the resulting formula. It is again generated by writing the Dyson's equation Eq. (2.97) with dressed propagators:

$$P = p + p \circlearrowleft \mathfrak{S}_{\text{OCA}} \circlearrowleft P \tag{2.125}$$

and we define the self-consistent "self-energy" for OCA as

$$\hat{\mathfrak{S}}_{\text{OCA}}(t_3, t_4) = \hat{\mathfrak{S}}_{\text{NCA}}(t_3, t_4) + 4 \sum_{\sigma_1} \sum_{\sigma_2} \int_{t_4}^{t_3} dt_1 \int_{t_4}^{t_1} dt_2 \tag{2.126}$$

$$\cdot \left(\hat{d}_{\sigma_1}^\dagger \Delta_{\sigma_1}(t_3, t_2) \hat{P}(t_3, t_1) \hat{d}_{\sigma_2}^\dagger \hat{P}(t_1, t_2) \hat{d}_{\sigma_1} \hat{P}(t_2, t_4) \Delta_{\sigma_2}(t_1, t_4) \hat{d}_{\sigma_2} \right. \tag{2.127}$$

$$- \hat{d}_{\sigma_1} \Delta_{\sigma_1}(t_2, t_3) \hat{P}(t_3, t_1) \hat{d}_{\sigma_2}^\dagger \hat{P}(t_1, t_2) \hat{d}_{\sigma_1}^\dagger \hat{P}(t_2, t_4) \Delta_{\sigma_2}(t_1, t_4) \hat{d}_{\sigma_2} \tag{2.128}$$

$$- \hat{d}_{\sigma}^\dagger \Delta_{\sigma_1}(t_3, t_2) \hat{P}(t_3, t_1) \hat{d}_{\sigma_2} \hat{P}(t_1, t_2) \hat{d}_{\sigma_1} \hat{P}(t_2, t_4) \Delta_{\sigma_2}(t_4, t_1) \hat{d}_{\sigma_2}^\dagger \tag{2.129}$$

$$\left. + \hat{d}_{\sigma_1} \Delta_{\sigma_1}(t_2, t_3) \hat{P}(t_3, t_1) \hat{d}_{\sigma_2} \hat{P}(t_1, t_2) \hat{d}_{\sigma_1}^\dagger \hat{P}(t_2, t_4) \Delta_{\sigma_2}(t_4, t_1) \hat{d}_{\sigma_2}^\dagger \right) \tag{2.130}$$

where $\hat{\mathfrak{S}}_{\text{NCA}}$ is the NCA contribution of the "self-energy" in Eq. (2.115) and the direction of integration should be consistent with the one in convolution Eq. (2.96). Just like in NCA, the atomic propagators (p or P) in OCA do not change the state of the impurity, that is, only the diagonal elements in $\hat{p}$ and $\hat{P}$

are non-zero. Consequently, $\hat{\mathfrak{S}}$ is also a diagonal matrix. Let's define

$$P_{|s\rangle}(t_1, t_2) \equiv \left\langle s \left| \hat{P}(t_1, t_2) \right| s \right\rangle \tag{2.131}$$

$$\mathfrak{S}_{|s\rangle}(t_1, t_2) \equiv \left\langle s \left| \hat{\mathfrak{S}}(t_1, t_2) \right| s \right\rangle \tag{2.132}$$

for each impurity state $|s\rangle$ ($s = 0, \uparrow, \downarrow, \uparrow\downarrow$). Then

- $|s = 0\rangle$ state

$$\mathfrak{S}_{|0\rangle}(t_1, t_2) = \mathfrak{S}_{|0\rangle,NCA}(t_1, t_2) \tag{2.133}$$

$$- 4 \int_{t_2}^{t_1} d\eta_1 \int_{t_2}^{\eta_1} d\eta_2 \left(\Delta_{|\uparrow\rangle}(\eta_2, t_1) \Delta_{|\downarrow\rangle}(t_2, \eta_1) \cdot P_{|\downarrow\rangle}(t_1, \eta_1) P_{|\uparrow\downarrow\rangle}(\eta_1, \eta_2) P_{|\uparrow\rangle}(\eta_2, t_2) \right. \tag{2.134}$$

$$\left. + \Delta_{|\downarrow\rangle}(\eta_2, t_1) \Delta_{|\uparrow\rangle}(t_2, \eta_1) \cdot P_{|\uparrow\rangle}(t_1, \eta_1) P_{|\uparrow\downarrow\rangle}(\eta_1, \eta_2) P_{|\downarrow\rangle}(\eta_2, t_2) \right) \tag{2.135}$$

- $|s = \uparrow\rangle$ state

$$\mathfrak{S}_{|\uparrow\rangle}(t_1, t_2) = \mathfrak{S}_{|\uparrow\rangle,NCA}(t_1, t_2) \tag{2.136}$$

$$+ 4 \int_{t_2}^{t_1} d\eta_1 \int_{t_2}^{\eta_1} d\eta_2 \left(\Delta_{|\downarrow\rangle}(\eta_2, t_1) \Delta_{|\uparrow\rangle}(\eta_1, t_2) \cdot P_{|\uparrow\downarrow\rangle}(t_1, \eta_1) P_{|\downarrow\rangle}(\eta_1, \eta_2) P_{|0\rangle}(\eta_2, t_2) \right. \tag{2.137}$$

$$\left. + \Delta_{|\uparrow\rangle}(t_1, \eta_2) \Delta_{|\downarrow\rangle}(t_2, \eta_1) \cdot P_{|0\rangle}(t_1, \eta_1) P_{|\downarrow\rangle}(\eta_1, \eta_2) P_{|\uparrow\downarrow\rangle}(\eta_2, t_2) \right) \tag{2.138}$$

- $|s = \downarrow\rangle$ state

$$\mathfrak{S}_{|\downarrow\rangle}(t_1, t_2) = \mathfrak{S}_{|\downarrow\rangle,NCA}(t_1, t_2) \tag{2.139}$$

$$+ 4 \int_{t_2}^{t_1} d\eta_1 \int_{t_2}^{\eta_1} d\eta_2 \left(\Delta_{|\uparrow\rangle}(\eta_2, t_1) \Delta_{|\downarrow\rangle}(\eta_1, t_2) \cdot P_{|\uparrow\downarrow\rangle}(t_1, \eta_1) P_{|\uparrow\rangle}(\eta_1, \eta_2) P_{|0\rangle}(\eta_2, t_2) \right. \tag{2.140}$$

$$\left. + \Delta_{|\downarrow\rangle}(t_1, \eta_2) \Delta_{|\uparrow\rangle}(t_2, \eta_1) \cdot P_{|0\rangle}(t_1, \eta_1) P_{|\uparrow\rangle}(\eta_1, \eta_2) P_{|\uparrow\downarrow\rangle}(\eta_2, t_2) \right) \tag{2.141}$$

- $|s =\uparrow\downarrow\rangle$ state

$$\mathfrak{S}_{|\uparrow\downarrow\rangle}(t_1, t_2) = \mathfrak{S}_{|\uparrow\downarrow\rangle, NCA}(t_1, t_2) \tag{2.142}$$

$$- 4 \int_{t_2}^{t_1} d\eta_1 \int_{t_2}^{\eta_1} d\eta_2 \left(\Delta_{|\downarrow\rangle}(t_1, \eta_2) \Delta_{|\uparrow\rangle}(\eta_1, t_2) \cdot P_{|\uparrow\rangle}(t_1, \eta_1) P_{|0\rangle}(\eta_1, \eta_2) P_{|\downarrow\rangle}(\eta_2, t_2) \right. \tag{2.143}$$

$$\left. + \Delta_{|\uparrow\rangle}(t_1, \eta_2) \Delta_{|\downarrow\rangle}(\eta_1, t_2) \cdot P_{|\downarrow\rangle}(t_1, \eta_1) P_{|0\rangle}(\eta_1, \eta_2) P_{|\uparrow\rangle}(\eta_2, t_2) \right) \tag{2.144}$$

And for the propagators P, the integral form of OCA stays the same as in NCA, as they all follow from the Dyson's equation. And in spite of self-consistent approximations we choose, the correction to the expectation value of an equal-time observable is always Eq. (2.98):

$$\langle \hat{O}(t) \rangle = \frac{i}{\tilde{Z}_D} \mathrm{Tr}_D \left\{ \hat{\xi} \hat{P}(t_+, t_-) \hat{O} \right\} \tag{2.145}$$

where the dressed propagator $\hat{P}$ is the corresponding dressed propagator from the self-consistent approximation, such as NCA Eq. (2.114) or OCA Eq. (2.125).

Chapter 3

Quantum Monte Carlo Algorithm for Impurity Models out of Equilibrium

The ongoing experimental progress has stimulated intensive research on the theoretical side. As we mentioned, a promising framework to capture both ultrafast dynamics and strong electronic correlations is the nonequilibrium formulation of dynamical mean-field theory (DMFT). The biggest challenge within the context of nonequilibrium DMFT is the development of impurity solvers which allow to compute the long-time dynamics after a perturbation.

Solving the interacting quantum impurity model is conceptually and algorithmically challenging and no analytical solution is available. There have been a wide range of approximate techniques developed to solve the model. For example, exact-diagonalization (ED) [61] approximates the continuum of bath levels by a small number variationally chosen eigenstates and hybridization function, but is limited by the number of bath site can be included. Density matrix renormalization group (DMRG) [62] and numerical renormalization group (NRG) methods both intelligently truncate the Hilbert space, where NRG is based on iterative diagonalization using a logarithmic discretization of the energy spectrum of the bath states and DMRG involves an isolation of the relevant low-lying states.

However, they are particularly powerful in resolving collective states and low energy levels but encounter difficulties in providing information over a wide range of frequencies.

Another approach, which we use in our calculations, is the so-called *continuous time Quantum Monte Carlo* (CT-QMC) method. At equilibirum, there have been a class of CT-QMC methods developed to accomodate different coupling regimes and they have the advantage of avoiding the time discretization of Hirsch-Fye quantum Monte Carlo methods [63] and providing very efficient and flexible solvers at $T > 0$ [64]. At the side of its nonequilibrium extension, however, no numerical "exact" solver has been developed. It requires a generalization of the expansion on the imaginary time branch in equilibrium to the full Keldysh contour to represent the time dependent dynamics. For example, self-consistent perturbation expansion around the atomic limit (generalization of NCA in Sec. 2.3.1 and OCA in Sec. 2.3.2) [58] are reliable at limited parameter regimes, e.g. when interaction U is much larger than the bandwidth of the bath. [65] and [55] are formulated on the forward-backward Keldysh contour thus are lack of the physical initial conditions of the system.

In this chapter, we will present a detailed description of the numerical algorithm we developed that is suitable for strong-coupling regimes. This is a generalization of the continuous time hybridization expansion solver in [55] to Keldysh contour. We will begin in Sec. 3.1 with a short derivation and formalism of the general hybridization expansion approach in nonequilibrium on Keldysh contour. In Sec. 3.2, we will outline the details of the Monte Carlo procedure performed in the sampling of the configuration space. And we discuss the measurements available in this method and state the procedures to calculate them. We examine the dynamics of a correlated quantum dot in the mixed valence regime in Sec. 3.5 [66]. We perform numerically exact calculations of the current after a quantum quench from equilibrium by rapidly applying a bias voltage in a wide range of initial temperatures. The current exhibits short equilibration times and saturates upon the decrease of temperature at all times, indicating Kondo behavior

both in the transient regime and in steady state. The time-dependent current saturation temperature connects the equilibrium Kondo temperature to a substantially increased value at voltages outside of linear response. These signatures are directly observable by experiments in the time-domain.

3.1 Continuous-time QMC - hybridization expansion

CT-QMC methods start with the same basic idea of the perturbation theory – splitting of the Hamiltonian. We are interested in the strongly coupling regime, therefore we will perform the expansion in powers of the dot-lead hybridization $\mathcal{V}$. As in Eq. (2.32), we write

$$H = H_0 + H_{\text{hyb}} \tag{3.1}$$

where $H_0 = H_{\text{bath}} + H_D$ denotes the bare decoupled system. And this corresponds to writing

$$S = S_0 + S_{\text{hyb}} \tag{3.2}$$

where $S_0 = c^*\Delta^{-1}c + S_D$ and $S_{\text{hyb}} = -d^*c - c^*d$ in Eq. (2.2). Then we expand a general average of some local operator in Eq. (2.29) in powers of S_{hyb} and get

$$\langle \hat{O}(t) \rangle = \frac{1}{\tilde{Z}_D} \sum_{n=0}^{\infty} \sum_{o_i=d,d^\dagger} \int_0^{-i\beta} dt_1 \int_{t_3}^{t_1} dt_2 \ldots \int_t^{t_{k-1}} dt_k \int_{t_{k+2}}^{t} dt_{k+1} \ldots \int_0^{t_{2n-1}} dt_{2n}$$

$$\times \text{Tr}_s w(o_1 \ldots o_{2n}, t_1 \ldots t_{2n}, \mathcal{P}, s) \tag{3.3}$$

where

$$w(o_1 \ldots o_{2n}, t_1 \ldots t_{2n}, \mathcal{P}, s) \tag{3.4}$$

$$= (-i)^{2n}(-1)^{\mathcal{P}} \langle s| e^{-\beta \hat{H}_D} \hat{o}_1(t_1) \ldots \hat{o}_k(t_k) \hat{O}(t) \hat{o}_{k+1}(t_{k+1}) \ldots \hat{o}_{2n}(t_{2n}) |s\rangle \cdot i^n \det \Delta(t_1 \ldots t_{2n}) \tag{3.5}$$

- the first $(-i)^{2n}$ comes from the prefactor in expanding $e^{iS_0 + iS_{\text{hyb}}}$ in powers of S_{hyb} to the $2n^{\text{th}}$ order;

- $(-1)^{\mathcal{P}}$ is a permutation factor that comes from the sign change from explicit time ordering;

- $-i\beta \geq t_1 > \ldots > t_k > t > t_{k+1} > \ldots > t_{2n} \geq 0_+$ follows the time-ordering on the Keldysh contour;

- each operator $\hat{o}_i$ can be a $\hat{d}_\sigma$ or a $\hat{d}_\sigma^\dagger$, and the numbers of $\hat{d}_\sigma$ and $\hat{d}_\sigma^\dagger$ have to be the same;

- s denotes one of the four atomic states $|0\rangle$, $|\uparrow\rangle$, $|\downarrow\rangle$ and $|\uparrow\downarrow\rangle$;

- the last term $i^n \det \Delta(t_1 \ldots t_{2n})$ comes from applying the Wick's theorem to the n-particle Green's function of the bath electrons that is obtained by the expansion because they are non-interacting and

$$
\det \Delta(t_1 \ldots t_{2n}) \equiv \det \begin{pmatrix} \Delta(t_{i_1}, t_{j_1}) & \Delta(t_{i_1}, t_{j_2}) & \cdots & \Delta(t_{i_1}, t_{j_n}) \\ \Delta(t_{i_2}, t_{j_1}) & \Delta(t_{i_2}, t_{j_2}) & \cdots & \Delta(t_{i_2}, t_{j_n}) \\ \vdots & \vdots & \ddots & \vdots \\ \Delta(t_{i_n}, t_{j_1}) & \Delta(t_{i_n}, t_{j_2}) & \cdots & \Delta(t_{i_n}, t_{j_n}) \end{pmatrix} \quad (3.6)
$$

where $t_{i_1} \ldots t_{i_n}$ are the times where $\hat{o}_i$'s are $\hat{d}_\sigma^\dagger$'s and $t_{j_1} \ldots t_{j_n}$ are the times where $\hat{o}_i$'s are $\hat{d}_\sigma$'s.

We can further write the expectation in $w(o_1 \ldots o_{2n}, t_1 \ldots t_{2n}, \mathcal{P}, s)$ in terms of the atomic propagators defined in Eq. (2.62) as

$$
\langle s | e^{-\beta \hat{H}_D} \hat{o}_1(t_1) \ldots \hat{o}_k(t_k) \hat{O}(t) \hat{o}_{k+1}(t_{k+1}) \ldots \hat{o}_{2n}(t_{2n}) | s \rangle \quad (3.7)
$$

$$
= (-1)^k \langle s | \hat{\xi} \hat{o}_{k+1}(t_{k+1}) \ldots \hat{o}_{2n}(t_{2n}) \hat{\xi} e^{-\beta \hat{H}_D} \hat{o}_1(t_1) \ldots \hat{o}_k(t_k) \hat{O}(t) | s \rangle \quad (3.8)
$$

$$
= (-1)^k i^{2n+1} \langle s | \hat{\xi} \hat{p}(t, t_{k+1}) \ldots \hat{p}(t_{k-1}, t_k) \hat{p}(t_k, t) \hat{O} | s \rangle \quad (3.9)
$$

Therefore, splitting w into several parts gives

$$w(o_1 \ldots o_{2n}, t_1 \ldots t_{2n}, \mathcal{P}, s) = i^{n+1} w_{\text{loc}} w_{\text{hyb}} \mathcal{O}(s) \qquad (3.10)$$

$$w_{\text{loc}} = (-1)^{\mathcal{P}} (-1)^k \langle s | \hat{\xi} \hat{p}(t, t_{k+1}) \ldots \hat{p}(t_{k-1}, t_k) \hat{p}(t_k, t) | s \rangle \qquad (3.11)$$

$$w_{\text{hyb}} = \det \Delta(t_1 \ldots t_{2n}) \qquad (3.12)$$

because for a non-vanishing contribution, the operator $\hat{O}$ should commute with $\hat{H}_D$, therefore can be separated from the expectation expression and written as a projected value on state s as $\mathcal{O}(s)$.

We interpret Eq. (3.3) as a sum over the configuration space that is the collection of all possible *hybridization line configurations* on the Keldysh contour $\mathcal{C}$: $\mathbf{x} = \{s, \{t_1, \sigma_1, \zeta_1\}, \{t_2, \sigma_2, \zeta_2\}, \ldots, \{t_{2n}, \sigma_{2n}, \zeta_{2n}\}\}$, $n = 0, 1, 2, \ldots$, s is the atomic state at time t, the time indices $t_i \in \mathcal{C}$, the spin indices $\sigma_i = \uparrow$ or $\downarrow$, and $\zeta_i = \pm$ denotes whether the operator $\hat{o}$ at the particular time t_i is $\hat{d}^\dagger$ ($\zeta_i = +$) or $\hat{d}$ ($\zeta_i = -$). And each configuration has a weight $\frac{1}{Z_D} w(o_1 \ldots o_{2n}, t_1 \ldots t_{2n}, \mathcal{P}, s)$. One example with $n = 3$ is shown in Fig. 3.1 and it belongs to the 6th order correction in the perturbation expansion.

The green lines are the hybridization lines that connect where electrons hop from the impurity to the bath (open circles) and where electrons hop from the bath to the impurity (filled circles). The top panel is one way to connect the hybridization lines that originate from one of the terms in the determinant in w_{hyb}. And the bottom panel shows the other non-zero possibility. From the construction of the Hamiltonian, the evolution operator does not change the number of particles on the impurity and conserves the spins. Thus the numbers of the filled circles ("+" points) and the open circles ("−" points) have to be the same in order to get a non-vanishing diagram. Also the two end points of a hybridization line have to be of the same spin. Therefore the two diagrams shown in Fig. 3.1 are the only two contributing terms in this configuration.

With the diagram interpretation, the self-consistent approximate methods, NCA introduced in Sec. 2.3.1 and OCA in Sec. 2.3.2 associate with sums over some
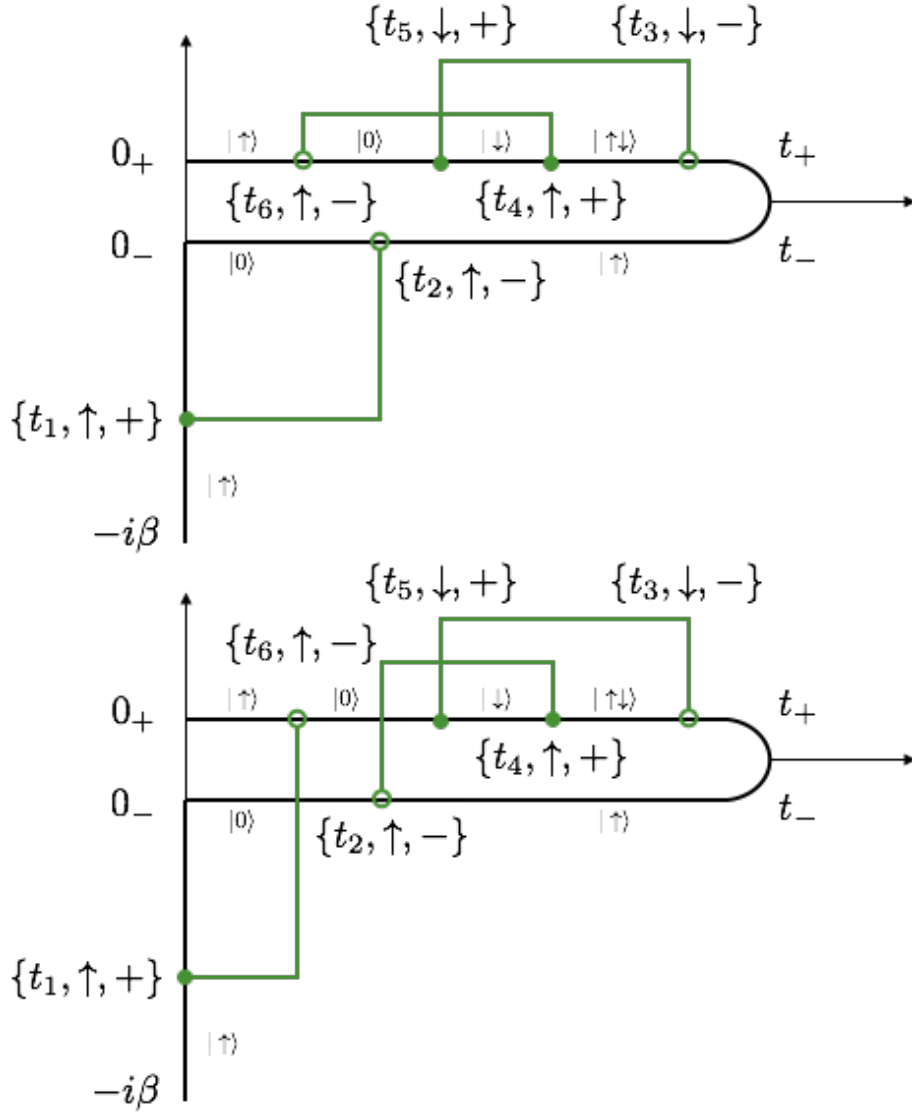
FIGURE 3.1: The two possibilities of drawing hybridization lines in configuration $\mathbf{x} = \{|\uparrow\rangle, \{t_1, \uparrow, +\}, \{t_2, \uparrow, -\}, \{t_3, \downarrow, -\}, \{t_4, \uparrow, +\}, \{t_5, \downarrow, +\}\{t_6, \uparrow, -\}\}$. The green lines are the hybridization lines, the open circles denote the moments when electrons hop from the impurity to the bath, and the filled circles denote the moments when electrons hop from the bath to the impurity. The atomic states at each stage are also shown along the contour.
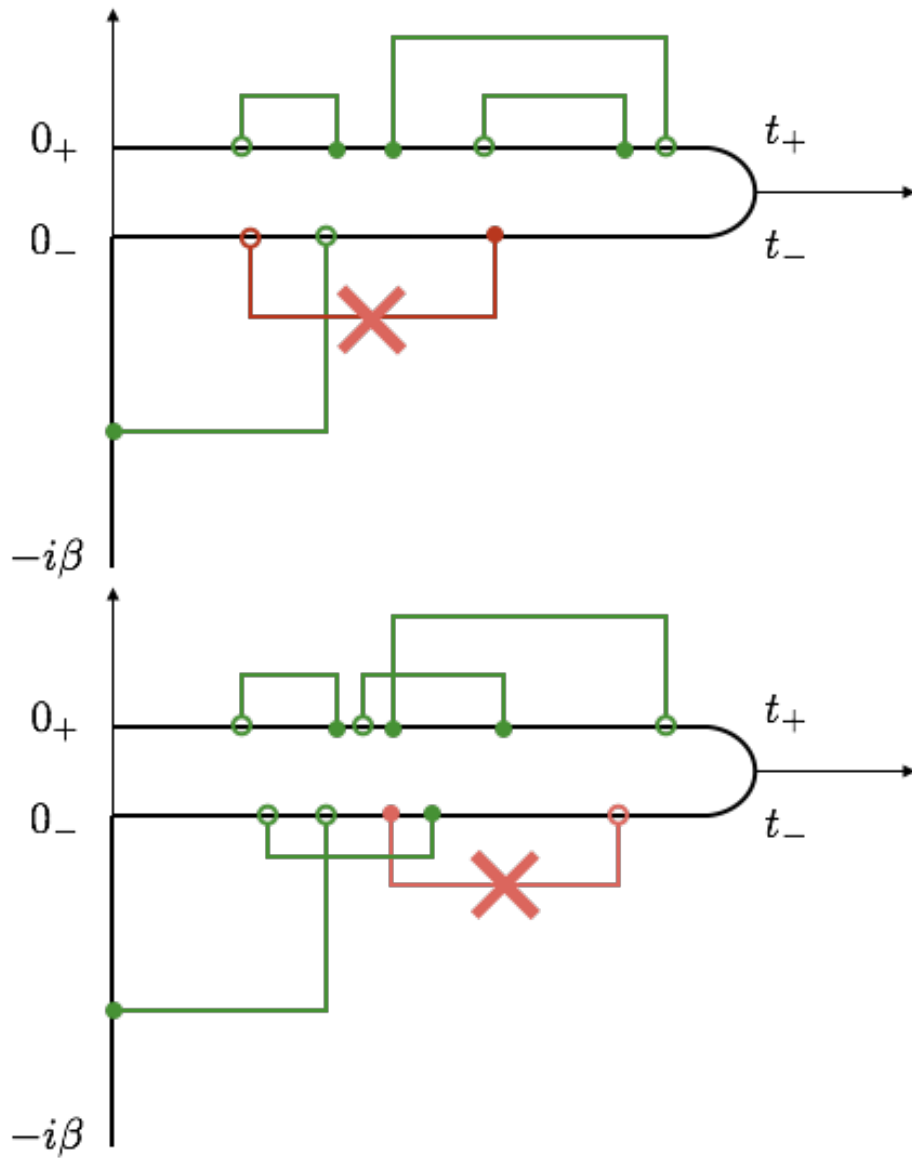
FIGURE 3.2: Illustrations of NCA and OCA diagrams. Top panel: An example of NCA diagrams. Hybridization lines are not allowed to cross with each other, therefore the red line is prohibited. Bottom panel: An example of OCA diagrams. Hybridization lines are not allowed to cross twice, so the red line can not be added.

subsets of the configuration space. The NCA subspace includes all diagrams with no hybridization lines crossing with each other. And the OCA subspace consists of the diagrams that have maximum one crossing with other hybridization lines. These features are direct consequences of the constructions of their self-energies and partial sums over these subspaces will recover the self-consistent approximate solutions respectively.

In this way, computing an average is turned into an enumeration of all the possible configurations. And since the configuration space is large, the direct approach is impractical. We use instead the statistical methods and estimate the average values. The well-established procedure is a Monte Carlo sampling of the most probable configurations, as described by [67] and first proposed in the equilibrium *contious-time hybridization expansion* (CT-HYB) study of AIM in [68]. We rewrite the expectation value of a quantity $\hat{O}$ in Eq. (3.3) as an integration over the configuration space C with weight w

$$\langle \hat{O}(t) \rangle = \langle O \rangle_w = \frac{1}{\tilde{Z}_D} \int_C d\mathbf{x} \, \mathcal{O}(\mathbf{x}) w(\mathbf{x}) \tag{3.13}$$

where we group the rest of $w(t_1 \ldots t_{2n}, P, s)$ except $\mathcal{O}(\mathbf{x})$ to be $w(\mathbf{x})$:

$$w(\mathbf{x}) = i^{n+1} w_{\text{loc}}(\mathbf{x}) w_{\text{hyb}}(\mathbf{x}). \tag{3.14}$$

This weighed sum can be estimated in a Monte Carlo procedure by selecting M configurations $\mathbf{x}_i$ with a probability $w(\mathbf{x}_i) d\mathbf{x}_i / \tilde{Z}_D$ and averaging the contributions $\mathcal{O}(\mathbf{x}_i)$:

$$\langle O \rangle_w \approx \langle O \rangle_{\text{MC}} \equiv \frac{1}{M} \sum_{i=1}^{M} \mathcal{O}(\mathbf{x}_i) \tag{3.15}$$

And according to the central limit theorem, if the number of configurations is large enough, the estimate $\langle O \rangle_{\text{MC}}$ will be normally distributed around the exact value $\langle O \rangle_w$ with variance

$$\langle (\Delta O)^2 \rangle \equiv \langle (O_{\text{MC}} - O_w)^2 \rangle = \frac{\text{Var} O}{M} \tag{3.16}$$

58

3.2   Monte Carlo procedure and details

Integrals with general distributions such as Eq. (3.13) are best sampled by generating configurations using a Markov process. A Markov process is fully characterized by a transition matrix $W_{\mathbf{xy}}$ specifying the probability of going from state $\mathbf{x}$ to state $\mathbf{y}$ in one step of the Markov process. Conservation of probabilities requires $\sum_{\mathbf{y}} W_{\mathbf{xy}} = 1$. Starting from an arbitrary distribution, the Markov process will converge exponentially to a stationary distribution $w(\mathbf{x})$ as we desire if the following two conditions are satisfied:

- Ergodicity: It has to be possible to reach any configuration $\mathbf{x}$ from any other configuration $\mathbf{y}$ in a finite number of Markov steps, i.e. for all $\mathbf{x}$ and $\mathbf{y}$ there exists an integer $N < \infty$ such that for all $n \geq N$ the probability $(W^n)_{\mathbf{xy}} \neq 0$.

- Balance: Stationarity implies that the distribution $w(\mathbf{x})$ fulfills the balance condition

$$\int_C d\mathbf{x} \; w(\mathbf{x}) W_{\mathbf{xy}} = w(\mathbf{y}), \qquad (3.17)$$

  that is, $w(\mathbf{x})$ is a left eigenvector of the transition matrix $W_{\mathbf{xy}}$. A sufficient but not necessary condition usually used instead of the balance condition is the *detailed balance* condition

$$\frac{W_{\mathbf{xy}}}{W_{\mathbf{yx}}} = \frac{w(\mathbf{y})}{w(\mathbf{x})} \qquad (3.18)$$

  which we use in our calculations.

The first, and still most widely used, algorithm that satisfies the detailed balance condition is the Metropolis-Hastings algorithm [67, 69]. The transition from a configuration $\mathbf{x}$ to a new configuration $\mathbf{y}$ is proposed with a probability $W_{\mathbf{xy}}^{\mathrm{prop}}$ but accepted only with probability $W_{\mathbf{xy}}^{\mathrm{acc}}$. If the proposal is rejected, the old

configuration $\mathbf{x}$ is used again. The transition matrix is

$$W_{\mathbf{xy}} = W_{\mathbf{xy}}^{\text{prop}} W_{\mathbf{xy}}^{\text{acc}} \tag{3.19}$$

and the detailed balance condition Eq.(3.18) is satisfied by using the Metropolis-Hastings acceptance rate:

$$W_{\mathbf{xy}}^{\text{acc}} = \min \left\{ 1, R_{\mathbf{xy}} \right\}. \tag{3.20}$$

with the acceptance ratio $R_{\mathbf{xy}}$ given by

$$R_{\mathbf{xy}} = \frac{w(\mathbf{y}) W_{\mathbf{yx}}^{\text{prop}}}{w(\mathbf{x}) W_{\mathbf{xy}}^{\text{prop}}} \tag{3.21}$$

and $R_{\mathbf{yx}} = 1/R_{\mathbf{xy}}$. Notice that here, we omit the integral variable $d\mathbf{x}$ that is also part of the distribution probability for neatness, but one should always keep in mind its existence.

3.2.1 Updates and evaluations

The two basic updates required for ergodicity of the Markov process in CT-HYB are the insertion of and the removal of a *segment* $\hat{d}^\dagger(\eta_1)\hat{d}(\eta_2)$ or an *antisegment* $\hat{d}(\eta_1)\hat{d}^\dagger(\eta_2)$, $\eta_1 > \eta_2$. The strategy we choose for inserting a segment/antisegment is the following: we pick a random time on $\mathcal{C}$ for the creation operator $\hat{d}^\dagger$. If it falls on an existing segment/antisegment of the same spin, the impurity is already occupied, so $w(\mathbf{x}_{n+1}) = 0$ and the move is rejected. If it falls on an empty space, we compute l_m, the length from this position to either the next segment or the next antisegment, whichever encountered first along the direction of increasing contour time. If there are no segments/antisegments on the contour, $l_m = l \equiv 2t_{\max} + \beta$, i.e. the total length of the Keldysh contour with $t_{\max}$ being the time at the tip of the contour. The position of the new annihilation operator $\hat{d}$ is then chosen randomly in this interval of l_m. The Keldysh contour is cyclic around $-i\beta \to 0_+$, so the searching of l_m will wind around the end

point $-i\beta$ till reaching η_1, where η_1 is the time of the creation operator. If the annihilation operator is inserted at a later time η_2 and $\eta_2 > \eta_1$, we have an antisegment; and if $\eta_2 < \eta_1$, we have a segment. If we propose to remove a randomly chosen segment/antisegment, the probability is $1/n$, where n is the total number of hybridization lines in the current configuration. In conclusion, we have the proposal probabilities

$$W^{\text{prop}}_{\mathbf{x}_n \to \mathbf{x}_{n+1}} = \frac{\Delta t}{l} \frac{\Delta t}{l_m} \tag{3.22}$$

$$W^{\text{prop}}_{\mathbf{x}_{n+1} \to \mathbf{x}_n} = \frac{1}{n+1} \tag{3.23}$$

where Δt being the discretization of the Keldysh contour. In principal, one can choose different discretizations on different branches or even non-uniform discretizations. For simplicity, we choose to have a uniform discretization throughout the contour, as well as the derivation. Then

$$\frac{w(\mathbf{x}_{n+1})}{w(\mathbf{x}_n)} = i \cdot \frac{(-1)^{\mathcal{P}_{n+1}}}{(-1)^{\mathcal{P}_n}} \frac{(-1)^{k_{n+1}}}{(-1)^{k_n}} \frac{\det \Delta(t_1, \ldots, t_{2n+2})}{\det \Delta(t_1, \ldots, t_{2n})} d\eta_1 d\eta_2 \tag{3.24}$$

$$\times \frac{\langle s_{n+1} | \hat{\xi} \hat{p}(t, t_{k_{n+1}+1}) \ldots \hat{p}(t_{k_{n+1}-1}, t_{k_{n+1}}) \hat{p}(t_{k_{n+1}}, t) | s_{n+1} \rangle}{\langle s_n | \hat{\xi} \hat{p}(t, t_{k_n+1}) \ldots \hat{p}(t_{k_n-1}, t_{k_n}) \hat{p}(t_{k_n}, t) | s_n \rangle} \tag{3.25}$$

where $d\eta_1$ and $d\eta_2$ are the integral variables that come directly from contour integrals $d\mathbf{x}_{n+1}$ as the added times η_1, η_2 for the new segment/antisegment. And $d\eta = f \cdot \Delta t$, with f being the "contour factors" $(+1, -1, i)$ depending on the branch of added time points t_1, t_2 on $\mathcal{C}_+$, $\mathcal{C}_-$ or $\mathcal{C}_M$. Therefore the acceptance ratio of adding a segment/antisegment is given by

$$R_{\mathbf{x}_n \to \mathbf{x}_{n+1}} = \frac{w(\mathbf{x}_{n+1}) W^{\text{prop}}_{\mathbf{x}_{n+1} \to \mathbf{x}_n}}{w(\mathbf{x}_n) W^{\text{prop}}_{\mathbf{x}_n \to \mathbf{x}_{n+1}}} \tag{3.26}$$

$$= i \cdot \frac{(-1)^{\mathcal{P}_{n+1}}}{(-1)^{\mathcal{P}_n}} \frac{(-1)^{k_{n+1}}}{(-1)^{k_n}} \frac{\det \Delta(t_1, \ldots, t_{2n+2})}{\det \Delta(t_1, \ldots, t_{2n})} \frac{l \cdot l_m}{n+1} f_1 f_2$$

$$\times \frac{\langle s_{n+1} | \hat{\xi} \hat{p}(t, t_{k_{n+1}+1}) \ldots \hat{p}(t_{k_{n+1}-1}, t_{k_{n+1}}) \hat{p}(t_{k_{n+1}}, t) | s_{n+1} \rangle}{\langle s_n | \hat{\xi} \hat{p}(t, t_{k_n+1}) \ldots \hat{p}(t_{k_n-1}, t_{k_n}) \hat{p}(t_{k_n}, t) | s_n \rangle} \tag{3.27}$$

where f_1, f_2 are the contour factors depending on the branch of added time points η_1, η_2. Note that segments/antisegments can wind around the tip $t_{\max}$ and change

the tip state $|s\rangle$ at the measurement point.

In addition to the basic insertions and deletions of segments/antisegments, we also add the following two moves in order to increase the efficiency of sampling the configuration space:

1. If the current configuration is empty, flip the state at the tip $|s\rangle$ to one of the basis states.

2. Where there are no segments/antisegments for a certain spin σ, flip the occupation state of that spin at the tip.

3. Shift the end points of the existing segments/antisegments to another allowed position.

And all of these updates should satisfy the detailed balance condition.

3.2.2   Normalization

The MC average given by Eq. (3.15) is sufficient for computing any local observables. However, if we want to get specifically the value of, for example, the dressed dot partition function $\tilde{Z}_D$ by putting $\hat{O} = \hat{\mathbb{I}}$ in the formula, or dressed propagators introduced in Sec. 3.3.1, a *normalization* procedure is necessary.

Consider a reference system, for example a self-consistent non-crossing approximation (NCA) or one-crossing approximation (OCA) up to some fixed number of order n, we have

$$Z_{\mathrm{ref}} = \int d\mathbf{x}\ \mathbb{I}_{\mathrm{ref}}(\mathbf{x})w(\mathbf{x}) \tag{3.28}$$

$$\tilde{Z}_D = \int d\mathbf{x}\ w(\mathbf{x}) \tag{3.29}$$

where

$$\mathbb{I}_{\text{ref}}(\mathbf{x}) = \begin{cases} 1 & \text{if } \mathbf{x} = \mathbf{x}_{\text{ref}} \\ 0 & \text{otherwise} \end{cases} \tag{3.30}$$

is an indicator function for configurations in the reference system and $\mathbf{x}_{\text{ref}}$ represents the configurations that the reference system includes, for example, finite-order NCA/OCA diagrams. Dividing these two equations we get

$$\tilde{Z}_D = Z_{\text{ref}} \cdot \frac{\int d\mathbf{x} \ w(\mathbf{x})}{\int d\mathbf{x} \ \mathbb{I}_{\text{ref}}(\mathbf{x}) w(\mathbf{x})} \tag{3.31}$$

$$= Z_{\text{ref}} \cdot \frac{1}{\langle \mathbb{I}_{\text{ref}} \rangle_w} \tag{3.32}$$

where Z_{ref} is known and $\langle \mathbb{I}_{\text{ref}} \rangle_w$ can be estimated by a MC average $\langle \mathbb{I}_{\text{ref}} \rangle_{\text{MC}}$. In this way, $\tilde{Z}_D$ can be computed by iterating over each permutation in every configuration generated for measurements and identity whether it is one of the reference diagrams.

At high temperatures, perturbation orders are often small and this normalization method is feasible. However, at lower temperatures, large perturbation orders are observed and we can perform a series of calculations, progressively increasing the perturbation order and normalize with respect to lower order calculations as reference systems until convergence is achieved.

3.3 Measurements

In this section, we outline the quantities that are of interest in this thesis and state the methods to measure them.

3.3.1 Dressed propagators

From Eq. (3.10) we realize that for any local operator $\hat{O}$, the expression can be divided into two independent parts:

$$w(o_1 \ldots o_{2n}, t_1 \ldots t_{2n}, \mathcal{P}, s) = i\xi_s P(o_1 \ldots o_{2n}, t_1 \ldots t_{2n}, \mathcal{P}, s)\mathcal{O}(s) \qquad (3.33)$$

and

$$P(o_1 \ldots o_{2n}, t_1 \ldots t_{2n}, \mathcal{P}, s) = i^n \xi_s w_{\text{loc}} w_{\text{hyb}} \qquad (3.34)$$

can be interpreted as a $2n^{\text{th}}$ order expansion of the *dressed atomic propagators*

$$\hat{P}(t_1, t_2)_{s_1 s_2} = \begin{cases} -i \left\langle s_1 \left| e^{-i\hat{H}t_1} e^{i\hat{H}t_2} \right| s_2 \right\rangle & t_1 > t_2 \\ -i \langle s_1 | \hat{\xi} e^{-i\hat{H}t_1} e^{-\beta\hat{H}} e^{i\hat{H}t_2} | s_2 \rangle = i\hat{\xi} \left[\hat{P}(t_1, 0)\hat{P}(-i\beta, t_2) \right]_{s_1 s_2} & t_1 < t_2 \end{cases}$$

$$(3.35)$$

The form is exactly identical to the definition of bare atomic propagators $\hat{p}$ in Eq. (2.62) except for the full Hamiltonian $\hat{H}$ instead of the local impurity Hamiltonian $\hat{H}_D$ used in the expression. Here we integrate out the bath degrees of freedom and incorporate them as hybridization functions in Δ. Now, instead of sampling the local observables, we sample all the dressed propagators

$$\hat{P}_s(t_1, t_2) = \sum_{n=0}^{\infty} \sum_{o=d,d^\dagger} \int_0^{-i\beta} dt_1 \int_{t_3}^{t_1} dt_2 \ldots \int_t^{t_{k-1}} dt_k \int_{t_{k+2}}^t dt_{k+1} \ldots \int_0^{t_{2n-1}} dt_{2n}$$

$$\cdot P(o_1 \ldots o_{2n}, t_1 \ldots t_{2n}, \mathcal{P}, s) \qquad (3.36)$$

for every time pair $t_1 \succ t_2$ (on twisted Keldysh contour) and normalize the MC results using the technique in Sec. 3.2.2. Then any local observable has an universal form, as in NCA or OCA:

$$\langle \hat{O}(t) \rangle = \frac{i}{\tilde{Z}_D} \text{Tr}_D \left\{ \hat{\xi}\hat{P}(t_+, t_-)\hat{O} \right\} \qquad (3.37)$$

and different algorithms, self-consistent approximate methods or numerically "exact" QMC methods, all correspond to different samplings of dressed propagators.

3.3.2   Currents

We follow [70] and derive the currents through an interacting dot:

$$\langle \hat{I}(t) \rangle \equiv \left\langle \frac{d\hat{N}(t)}{dt} \right\rangle \tag{3.38}$$

By the equation of motion in the Heisenberg representation

$$i\frac{\partial \hat{X}(t)}{\partial t} = [\hat{X}(t), \hat{H}(t)] \tag{3.39}$$

we have

$$
\langle \hat{I}(t) \rangle = -i \left\langle [\hat{N}(t), \hat{H}(t)] \right\rangle \tag{3.40}
$$

$$
= -i \left\langle \sum_\sigma \left[\hat{d}_\sigma^\dagger(t) \hat{d}_\sigma(t), \mathcal{V} \sum_k \left(\hat{c}_{k\sigma}^\dagger(t) \hat{d}_\sigma(t) + \hat{d}_\sigma^\dagger(t) \hat{c}_{k\sigma}(t) \right) \right] \right\rangle \tag{3.41}
$$

$$
= -i\mathcal{V} \sum_{k\sigma} \left\langle \left(-\hat{c}_{k\sigma}^\dagger(t) \left\{ \hat{d}_\sigma^\dagger(t), \hat{d}_\sigma(t) \right\} \hat{d}_\sigma(t) + \hat{d}_\sigma^\dagger(t) \left\{ \hat{d}_\sigma(t), \hat{d}_\sigma^\dagger(t) \right\} \hat{c}_{k\sigma}(t) \right) \right\rangle
$$
$$\tag{3.42}$$

$$
= -i\mathcal{V} \sum_{k\sigma} \left(\left\langle \hat{d}_\sigma^\dagger(t) \hat{c}_{k\sigma}(t) \right\rangle - \left\langle \hat{c}_{k\sigma}^\dagger(t) \hat{d}_\sigma(t) \right\rangle \right) \tag{3.43}
$$

$$
= 2\mathcal{V} \sum_{k\sigma} \Im \left\{ \left\langle \hat{d}_\sigma^\dagger(t) \hat{c}_{k\sigma}(t) \right\rangle \right\} \tag{3.44}
$$

$$
= 2\mathcal{V} \sum_\sigma \Im \left\{ \frac{1}{Z} \int \mathcal{D}d^* \mathcal{D}d \mathcal{D}c^* \mathcal{D}c \; d_\sigma^*(t) c_\sigma(t) e^{ic^* \Delta^{-1} c + iS_D} \right. \tag{3.45}
$$

$$
\times \left. \left(-i\mathcal{V} \sum_{\sigma_1} \int dt_1 c_{\sigma_1}^*(t_1) d_{\sigma_1}(t_1) + \cdots \right) \right\} \tag{3.46}
$$

$$
= 2 \sum_\sigma \Im \left\{ \int dt_1 \Delta_\sigma(t, t_1) \left[\frac{1}{\tilde{Z}_D} \int \mathcal{D}d^* \mathcal{D}d \; e^{iS_D} d_\sigma^*(t) d_\sigma(t_1) + \cdots \right] \right\} \tag{3.47}
$$

$$
= -2 \sum_\sigma \Re \left\{ \int_\mathcal{C} dt' \; G_\sigma(t', t) \times \Delta_\sigma(t, t') \right\} \tag{3.48}
$$

Therefore, in order to compute the current, the Green's function of the impurity is required and is introduced in the next part.

3.3.3 Green's functions

In all methods discussed so far, diagrams or configurations are generated for local operators $\hat{O}$ with weights contributing to the partition function $\tilde{Z}_D$. Besides this, we are also interested in quantities with operators at two times, in particular, Green's functions. Single particle Green's functions are the fundamental objects of many-body theories. They describe single particle excitations as well as statistical distributions of particles, and play a central role in the formulation

66

of nonequilibrium DMFT, as seen in Sec. 1.3. They can be obtained by modifying such partition function configurations and sampling both series for $\tilde{Z}_D$ and $G(t, t')$ simultaneously. This method was originally employed in the bosonic context by [71] and it is often referred as the *worm sampling.*

We define the nonequilibrium Green's function as the contour-ordered expectation value

$$G_\sigma(t, t') \equiv -i \left\langle \mathcal{T}_\mathcal{C} \hat{d}_\sigma(t) \hat{d}_\sigma^\dagger(t') \right\rangle \tag{3.49}$$

where $\hat{d}_\sigma^\dagger(\hat{d}_\sigma)$ is a creation (annihilation) operator of the impurity particles, and $t, t' \in \mathcal{C}$. To get a flavor how the general weights look like, we write the expansion of the Green's function up to the second order in terms of H^{hyb}

$$\left\langle \mathcal{T}_\mathcal{C} \hat{d}_\sigma(t_1) \hat{d}_\sigma^\dagger(t_2) \right\rangle$$

$$= \frac{1}{Z} \int \mathcal{D}d^* \mathcal{D}d \mathcal{D}c^* \mathcal{D}c \; d_\sigma(t_1) d_\sigma^*(t_2) e^{iS} \tag{3.50}$$

$$= \frac{1}{Z} \int \mathcal{D}d^* \mathcal{D}d \mathcal{D}c^* \mathcal{D}c \; e^{ic^* \Delta^{-1} c + iS_D} d_\sigma(t_1) d_\sigma^*(t_2)$$

$$\times \left[1 - \sum_{\sigma_1} \int_\mathcal{C} dt_3 dt_4 d_{\sigma_1}^*(t_3) c_{\sigma_1}(t_3) c_{\sigma_1}^*(t_4) d_{\sigma_1}(t_4) \right] \tag{3.51}$$

$$= \frac{Z_{\text{bath}} Z_D}{Z} \left\langle \mathcal{T}_\mathcal{C} \hat{d}_\sigma(t_1) \hat{d}_\sigma^\dagger(t_2) \right\rangle_D$$

$$- \frac{i}{Z} \sum_{\sigma_1} \int_\mathcal{C} dt_3 dt_4 Z_{\text{bath}} \Delta_{\sigma_1}(t_3, t_4) \int \mathcal{D}d^* \mathcal{D}d \; e^{iS_D} d_\sigma(t_1) d_\sigma^*(t_2) d_{\sigma_1}^*(t_3) d_{\sigma_1}(t_4)$$

$$\tag{3.52}$$

$$= \frac{Z_D}{\tilde{Z}_D} \left\langle \mathcal{T}_\mathcal{C} \hat{d}_\sigma(t_1) \hat{d}_\sigma^\dagger(t_2) \right\rangle_D$$

$$- \frac{i}{\tilde{Z}_D} \sum_{\sigma_1} \int_\mathcal{C} dt_3 dt_4 \Delta_{\sigma_1}(t_3, t_4) \operatorname{Tr} \left\{ \mathcal{T}_\mathcal{C} e^{-\beta \hat{H}_D} \hat{d}_\sigma(t_1) \hat{d}_\sigma^\dagger(t_2) \hat{d}_{\sigma_1}^\dagger(t_3) \hat{d}_{\sigma_1}(t_4) \right\}$$

$$\tag{3.53}$$

where the notations all follows from the previously defined ones. Therefore, the general MC weight reads (with no loss of generality, we assume $t_1 > t_2$ here)

$$\frac{\tilde{Z}_D}{Z_D}\left\langle \mathcal{T}_{\mathcal{C}}\hat{d}_\sigma(t_1)\hat{d}_\sigma^\dagger(t_2)\right\rangle$$

$$= \sum_{n=0}^\infty \sum_{o_i=d,d^\dagger} \int_0^{-i\beta} dt_3 \int_{t_5}^{t_3} dt_4 \cdots \int_{t_1}^{t_{k-1}} dt_k \int_{t_{k+2}}^{t_1} dt_{k+1} \cdots \int_{t_2}^{t_{l-1}} dt_l \int_{t_{l+2}}^{t_2} dt_{l+1} \cdots \int_0^{t_{2n+1}} dt_{2n+2}$$

$$\times \operatorname{Tr}_s w\left(o_3,\ldots,o_{2n+2},t_1,t_2,\ldots,t_{2n+2},\mathcal{P},s\right) \tag{3.54}$$

where

$$w\left(o_3,\ldots,o_{2n+2},t_1,t_2,\ldots,t_{2n+2},\mathcal{P},s\right)$$

$$= i^{2n}(-1)^{\mathcal{P}}\left\langle s\left|e^{-\beta\hat{H}_D}\hat{o}(t_3)\cdots\hat{o}(t_k)\hat{d}_\sigma(t_1)\hat{o}_{k+1}(t_{k+1})\cdots\hat{o}_l(t_l)\hat{d}_\sigma^\dagger(t_2)\hat{o}_{l+1}(t_{l+1})\cdots\hat{o}_{2n+2}(t_{2n+2})\right|s\right\rangle$$

$$\cdot i^n \det\Delta\left(t_{3,\ldots,}t_{2n+2}\right) \tag{3.55}$$

in which $-i\beta \geq t_2 > \ldots > t_k > t_1 > t_{k+1} > \ldots > t_l > t_2 > t_{l+1} > \ldots > t_{2n+2} \geq 0_+$ follows the time-ordering on the Keldysh contour, and all the rest are the same as in Sec. 3.1.

We can again write the expectation in $w(o_3,\ldots,o_{2n+2},t_1\ldots t_{2n+2},\mathcal{P},s)$ in terms of the atomic propagators defined in Eq. (2.62) as

$$\left\langle s\left|e^{-\beta\hat{H}_D}\hat{o}(t_3)\cdots\hat{o}(t_k)\hat{d}_\sigma(t_1)\hat{o}_{k+1}(t_{k+1})\cdots\hat{o}_l(t_l)\hat{d}_\sigma^\dagger(t_2)\hat{o}_{l+1}(t_{l+1})\cdots\hat{o}_{2n+2}(t_{2n+2})\right|s\right\rangle$$

$$= (-1)^l\left\langle s\left|\hat{\xi}\hat{o}_{l+1}(t_{l+1})\cdots\hat{o}_{2n+2}(t_{2n+2})\hat{\xi}e^{-\beta\hat{H}_D}\hat{o}(t_3)\cdots\hat{o}(t_k)\hat{d}_\sigma(t_1)\hat{o}_{k+1}(t_{k+1})\cdots\hat{o}_l(t_l)\hat{d}_\sigma^\dagger(t_2)\right|s\right\rangle$$

$$= (-1)^l i^{2n+2}\left\langle s\left|\hat{\xi}\hat{p}(t_2,t_{l+1})\cdots\hat{p}(t_k,t_1)\hat{d}_\sigma\hat{p}(t_1,t_{k+1})\cdots\hat{p}(t_l,t_2)\hat{d}_\sigma^\dagger\right|s\right\rangle \tag{3.56}$$

Therefore, splitting w into several parts gives

$$w(o_3,\ldots,o_{2n+2},t_1,t_2,\ldots,t_{2n+2},\mathcal{P},s) = i^{n+2}w_{\text{loc}}w_{\text{hyb}} \tag{3.57}$$

$$w_{\text{loc}} = (-1)^{\mathcal{P}}(-1)^l\left\langle s\left|\hat{\xi}\hat{p}(t_2,t_{l+1})\cdots\hat{p}(t_k,t_1)\hat{d}_\sigma\hat{p}(t_1,t_{k+1})\cdots\hat{p}(t_l,t_2)\hat{d}_\sigma^\dagger\right|s\right\rangle \tag{3.58}$$

$$w_{\text{hyb}} = \det\Delta\left(t_{3,\ldots,}t_{2n+2}\right) \tag{3.59}$$

We can see that the expression for Green's function is in complete analogy to the partition function configurations: we can identify Green's function configurations as segment configurations with two additional $\hat{d}_\sigma$ and $\hat{d}_\sigma^\dagger$ operators. We have two options to proceed:

1. Trying to insert the operators $\hat{d}_\sigma(t_1)$, $\hat{d}_\sigma^\dagger(t_2)$ into a configuration of the partition function, and then compute the ratio of the local weights;

2. Identifying two operators in a partition function segment configuration, and removing the hybridization lines between them.

With 2, we identify that a configuration for the partition function at order n is thereby turned to a configuration of the Green's function at order $n-1$. If the overall weight associated with a partition function configuration is

$$
\begin{aligned}
&w_Z\left(o_1\ldots o_{2n+2}, t_1\ldots t_{2n+2}, \mathcal{P}, s\right) \\
&= i^{n+1}(-1)^{\mathcal{P}}(-1)^l\left\langle s\left|\hat{\xi}\hat{p}\left(t_2, t_{l+1}\right)\cdots\hat{p}\left(t_k, t_1\right)\hat{d}_\sigma\hat{p}\left(t_1, t_{k+1}\right)\cdots\hat{p}\left(t_l, t_2\right)\hat{d}_\sigma^\dagger\right|s\right\rangle\cdot\det\Delta\left(t_{1,\ldots,}t_{2n+2}\right)
\end{aligned}
$$

$$(3.60)$$

and the weight associated with a Green's function configuration is

$$
\begin{aligned}
&w_G\left(\{o_3\ldots o_{2n+2}, t_3\ldots t_{2n+2}\},\left(t_1, t_2\right), \mathcal{P}, s\right) \\
&= i^{n+2}(-1)^{\mathcal{P}}(-1)^l\left\langle s\left|\hat{\xi}\hat{p}\left(t_2, t_{l+1}\right)\cdots\hat{p}\left(t_k, t_1\right)\hat{d}_\sigma\hat{p}\left(t_1, t_{k+1}\right)\cdots\hat{p}\left(t_l, t_2\right)\hat{d}_\sigma^\dagger\right|s\right\rangle\cdot\det\Delta\left(t_{3,\ldots,}t_{2n+2}\right)
\end{aligned}
$$

$$(3.61)$$

Therefore, we employ the "reweighted" expectation value formula

$$
iG(t_1, t_2) = \left\langle\mathcal{T}_\mathcal{C}\hat{d}\left(t_1\right)\hat{d}^\dagger\left(t_2\right)\right\rangle = \frac{1}{\tilde{Z}_D}\int_C d\mathbf{x}\,\frac{w_G(\mathbf{x})}{w_Z(\mathbf{x})}w_Z(\mathbf{x})
$$

$$(3.62)$$

and accumulate

$$
\frac{w_G}{w_Z} = i\cdot\frac{\det\Delta\left(t_{3,\ldots,}t_{2n+2}\right)}{\det\Delta\left(t_{1,\ldots,}t_{2n+2}\right)}
$$

$$(3.63)$$

in the MC simulations. Thus, the Green's function is given by

$$G(t_1, t_2) = \left\langle \frac{\det \Delta \left(t_{3,\dots,}t_{2n+2}\right)}{\det \Delta \left(t_{1,\dots,}t_{2n+2}\right)} \right\rangle_{w_Z} \tag{3.64}$$

3.3.4   Spectral functions

One way to extract the spectral function $A(\omega)$ in equilibrium is by a direct Fourier transform of the real-time Green's function, which is not available in the equilibrium QMC. We have

$$G^{\gtrless}(t_1, t_2) = \int_{-\infty}^{+\infty} \frac{d\omega}{2\pi} \, e^{-i\omega(t_1 - t_2)} G^{\gtrless}(\omega) \tag{3.65}$$

$$G^{\gtrless}(\omega) = \int_{-\infty}^{+\infty} dt \, e^{i\omega(t_1 - t_2)} G^{\gtrless}(t_1, t_2) \tag{3.66}$$

and

$$G^{\gtrless}(t_1, t_2) = G(t_1, t_2) \qquad \text{when } t_1 \gtrless t_2 \text{ and } t_1, t_2 \in \mathcal{C}_+. \tag{3.67}$$

$G(t_1, t_2)$ is the contour-ordered Green's function and is directly accessible from the measurements. Then the spectral function is given by

$$A(\omega) = \frac{1}{2\pi} \Im \left[G^<(\omega) - G^>(\omega) \right] \tag{3.68}$$

There is an alternate way to produce the spectral functions firstly introduced in [72, 73] and it is briefly discussed in Appendix. 5.3.3.

3.4   The sign problem

Until now we have tacitly assumed that the expansion coefficients of our expectation value are always positive or zero. This has allowed us to interpret the weights as probability densities on the configuration space and the stochastic sampling of

these configurations in a Monte Carlo simulation. If the weights $w(\mathbf{x})$ becomes negative or even complex, as is often the case in fermionic simulations due to the anticommutation relations between fermionic operators, they can no longer be regarded as probabilities. The common solution is to sample with respect to the absolute value of the weight $|w(\mathbf{x})|$ and reweight the measurements as follows

$$\langle O \rangle_w = \frac{1}{\tilde{Z}_D} \int_C d\mathbf{x} \mathcal{O}(\mathbf{x}) w(\mathbf{x}) \tag{3.69}$$

$$= \frac{\int_C d\mathbf{x} \, \mathcal{O}(\mathbf{x}) \frac{w(\mathbf{x})}{|w(\mathbf{x})|} |w(\mathbf{x})|}{\int_C d\mathbf{x} \, \frac{w(\mathbf{x})}{|w(\mathbf{x})|} |w(\mathbf{x})|} \tag{3.70}$$

$$= \frac{\langle O \cdot (w/|w|) \rangle_{|w|}}{\langle w/|w| \rangle_{|w|}} \tag{3.71}$$

We denote $\mathrm{sign}(w) \equiv w(\mathbf{x})/|w(\mathbf{x})|$ then have

$$\langle O \rangle_w = \frac{\langle O \cdot \mathrm{sign} \rangle_{|w|}}{\langle \mathrm{sign} \rangle_{|w|}}, \tag{3.72}$$

so the average can be evaluated by sampling the numerator and denominator separately with respect to the positive weight $|w(\mathbf{x})|$.

However, while sampling with the absolute value and reweighting allows Monte Carlo simulations of systems with complex weights, it does not solve the so-called "*sign problem*": sampling of Eq. (3.72) suffers from exponentially growing errors. We consider the average sign

$$\langle \mathrm{sign} \rangle_{|w|} = \frac{\int_C d\mathbf{x} \, \mathrm{sign}(\mathbf{x}) |w(\mathbf{x})|}{\int_C d\mathbf{x} \, |w(\mathbf{x})|} = \frac{\tilde{Z}_{D,w}}{\tilde{Z}_{D,|w|}} \sim e^{-\beta \Delta F}. \tag{3.73}$$

We see it is the ratio of the partition function $\tilde{Z}_{D,w}$ and the partition function of a "bosonic" system $\tilde{Z}_{D,|w|}$ with positive weights $|w(\mathbf{x})|$. We express it in terms of the difference in free energies ΔF of these two systems and see that the quantity decreases exponentially as the temperature is lowered or the volume of the system is increased. Then the relative error after M measurements of MC procedures is

given by

$$\mathrm{err(sign)} = \frac{\sqrt{\mathrm{Var\ sign}/M}}{\langle\mathrm{sign}\rangle_{|w|}} \tag{3.74}$$

$$= \frac{\sqrt{\left(\langle\mathrm{sign}^2\rangle_{|w|} - \langle\mathrm{sign}\rangle_{|w|}^2\right)/M}}{\langle\mathrm{sign}\rangle_{|w|}} \tag{3.75}$$

$$\sim \sqrt{\left(1 - e^{-2\beta\Delta F}\right)/M} \cdot e^{\beta\Delta F} \tag{3.76}$$

$$\sim \frac{1}{M}e^{\beta\Delta F} \tag{3.77}$$

which grows exponentially with decreasing temperature and increasing system size. Fortunately, the equilibrium continuous-time QMC algorithms dot not have a sign problem at any filling in the case of the single-orbital impurity model [68, 74]. However, they generally suffer from a negative sign problem when applied to a multiorbital or cluster impurity model with an internal structure in which electrons can be exchanged [75], and the sign problem becomes worse as the system becomes larger.

But more to our concern, the non-equilibrium extension of the CT-HYB has a dynamical sign problem [55]: the factors of $\pm i$ associated with each order of the expansion of the time evolution operator $e^{\pm iHt}$ cause the average sign of the diagrams contributing to any quantity decays exponentially as the perturbation order is increased. Configurations with "+" signs canceling with configurations with "−" signs makes the MC sampling exponentially inefficient. To keep the error on $\langle O\rangle_w$ constant, we need to increase the number of Monte Carlo steps (at least) as $1/\langle\mathrm{sign}\rangle_{|w|}^2$, which becomes impractical. In the nonequilibrium simulation on a full Keldysh contour, the average perturbation order increases linearly with the time interval to be simulated as shown in Fig. 3.3 and it is not surprising that the signs drop down exponentially, as shown in Fig. 3.4, as an important limiting factor in the simulations.

In the next chapter, we adapt a new idea of "Inchworm Algorithm", based on
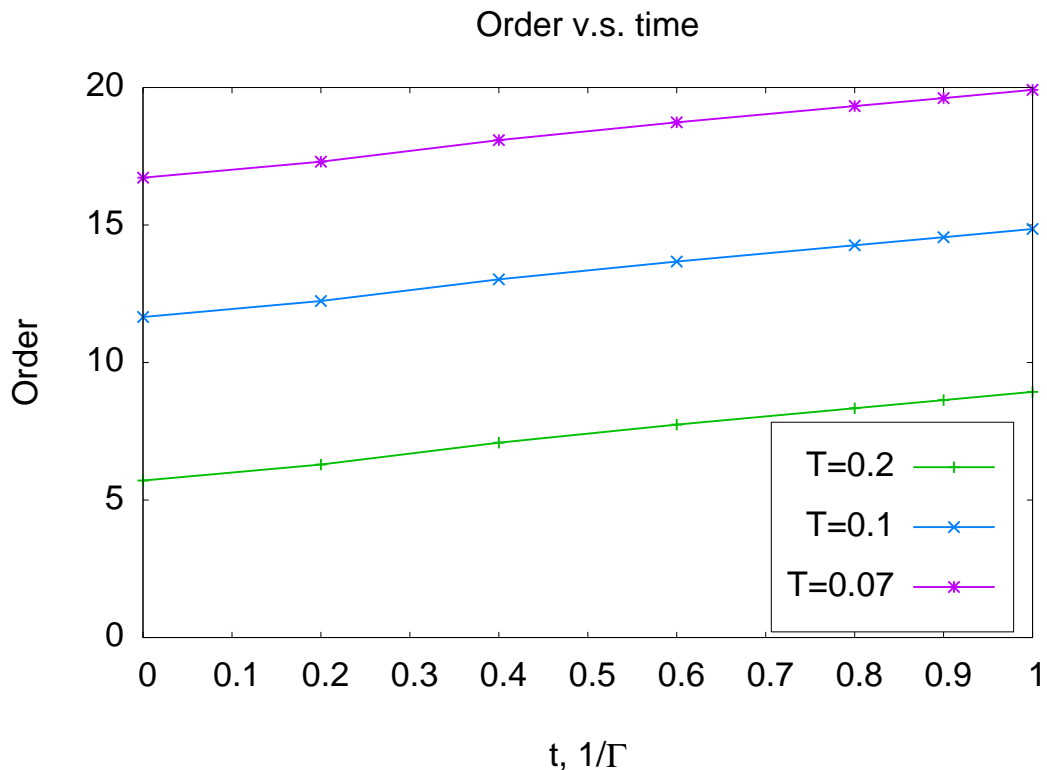
FIGURE 3.3: The growth of average perturbation orders as a function of time t along the real branch.

iteratively reusing the information obtained in previous steps to extend the propagation to longer times. The algorithm largely reduces the required order at each simulation and re-scales the exponential challenge to quadratic.

3.5 Application: Voltage quench dynamics of a Kondo system

The Kondo effect is a many-body phenomenon in which localized and itinerant electrons form a strongly correlated state [76]. It is an unusual scattering mechanism of conduction electrons in a metal due to magnetic impurities, which contributes a term to the electrical resistivity that increases logarithmically with temperature as the temperature T is lowered (as $\log(T)$). It shows signatures in thermodynamic, spectral, and linear response transport properties [77, 78] and
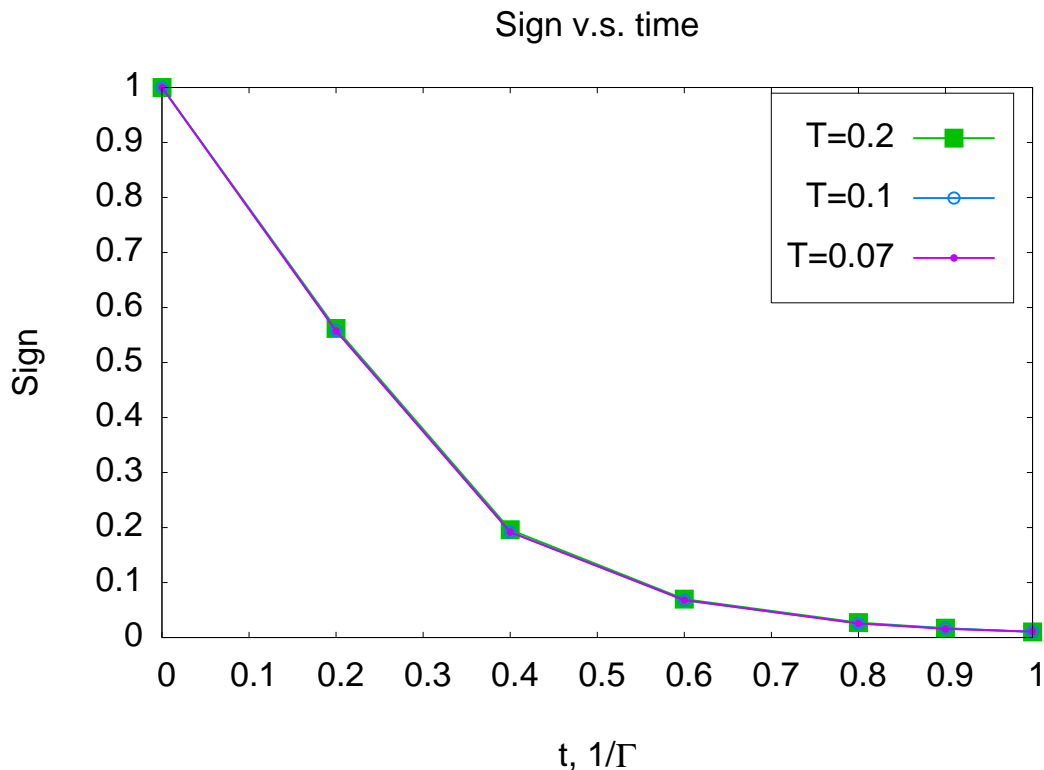
FIGURE 3.4: The average of the sign as a function of time t along the real branch.

has since been observed in a wide variety of correlated electron systems ranging from impurities adsorbed on surfaces [79, 80] to molecular transistors [81], heavy fermion materials [82], and mesoscopic quantum wires [83]. Kondo behavior is also observed in semiconducting quantum dot heterostructures, where a confined interacting region is coupled to non-interacting leads [44, 84, 85]. Gating of these systems allows to study Kondo physics over a wide parameter range [44].

Kondo correlations only emerge at low temperature. Their onset is character-ized by the Kondo temperature T_K that can be defined as the temperature at which the zero-bias conductance reaches half of its low-temperature value [77]. In thermal equilibrium, the Kondo problem is well understood and quantitatively described by a range of analytical and numerical methods [64, 86–89].

When a Kondo system is driven out of equilibrium, additional phenomena ap-pear. For instance, the application of a (time-independent) bias voltage splits

the Kondo peak [70, 85] and shows signatures in the double occupancy and magnetization [90]. At large voltages the voltage dependence of the conductance decreases on an energy scale comparable to T_K [91–93] and its temperature dependence saturates at temperatures above T_K [94, 95].

How observables evolve in time after a rapid change of parameters [96, 97] and how they decay to their steady state limit is an open question. Recent experimental progress in the measurement of time-dependent quantities on ever faster time scales has enabled experimental studies of such transient dynamics [98, 99], making a theoretical description of quenches from correlated initial states important.

In this section we apply the nonequilibrium impurity solver to examine the dynamics of a correlated quantum dot in the mixed valence regime. We present numerically exact results for the real time evolution of the single impurity Anderson model following a symmetric voltage quench $V(t) = V\theta(t)$ in Eq. (1.2c) from a correlated equilibrium ensemble to a non-equilibrium steady state. The system is in equilibrium for $t < 0$, and for $t > 0$ the lead levels ε_k are instantaneously moved to $\varepsilon_k \pm \frac{V}{2}$, with the sign depending on the lead index α. We show results for transient and steady state currents and populations at temperatures ranging from $T \gg T_K$ to $T \ll T_K$, which have not previously been accessible in numerical calculations.

Fig. 3.5 shows the behavior of the current $I_T(t)$ after a voltage quench. In panel (a) we show $I_T(t)$ as a function of time t following a voltage quench from $V = 0$ to $V = 2$ for a set of temperatures $0.07 \leq T \leq 1$ (between 0.7 and 11 K). Results from semi-analytical approximations are shown as fine dotted lines (NCA) and dash-dotted lines (OCA) for comparison. We observe that for all temperatures the current equilibrates at time $t \approx 0.6$ (≈ 2.5 ps) well within reachable times of ~ 1 (4 ps). As temperature is lowered from $T = 1$ (11 K) to $T \sim 0.2$ (2 K) the current at fixed times and in steady state increases. Further reducing T by a factor of five yields no additional increase of current, illustrated by panel (b).
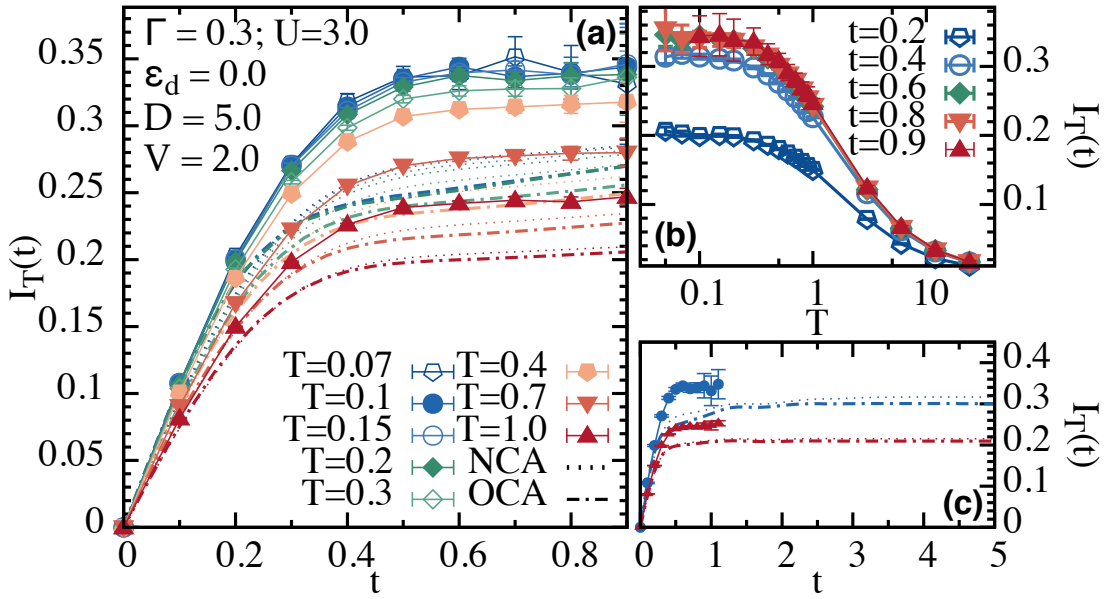
FIGURE 3.5: Current $I_T(t)$ as a function of time t after a voltage quench, for temperatures T indicated. Parameters $U = 3$, $\varepsilon_d = 0$, $\Gamma = 0.3$, $D = 5$ and $V = 2$. (a) Monte Carlo (solid symbols, full lines), NCA (dotted lines) and OCA (dash dotted lines) results. (b) The temperature dependence of $I_T(t)$ at times $t = 0.2 - 0.9$. (c) Behavior of the NCA and OCA currents up to $t = 5$.

We attribute the fast equilibration time to the high Kondo temperature of this mixed valence system [64].

Results from NCA and OCA correctly capture the short-time behavior and the overall shape of the current but underestimate both the transient and the steady state value by $\approx 20\%$. This is known for systems with $U < D$ [60], although the quality of these methods will presumably improve in the strong interaction limit and by including vertex corrections in OCA [100]. Both results are shown in panel (c) for times much longer than presently accessible by QMC. No additional time-dependence is visible, illustrating that our calculations are able to reach steady state.

The temperature dependence of the transient voltage quench dynamics is analyzed in Fig. 3.6 for $V = 2$ and (a) $\Gamma_1 = 0.3$, $U_1 = 3$; (b) $\Gamma_2 = 0.2$, $U_2 = 5$. Shown is the temperature dependence of the time-dependent current $I_T(t)/I_{T=0}(t)$ and static magnetic susceptibility $\chi_T/\chi_{T=0}$ normalized to the respective zero-temperature
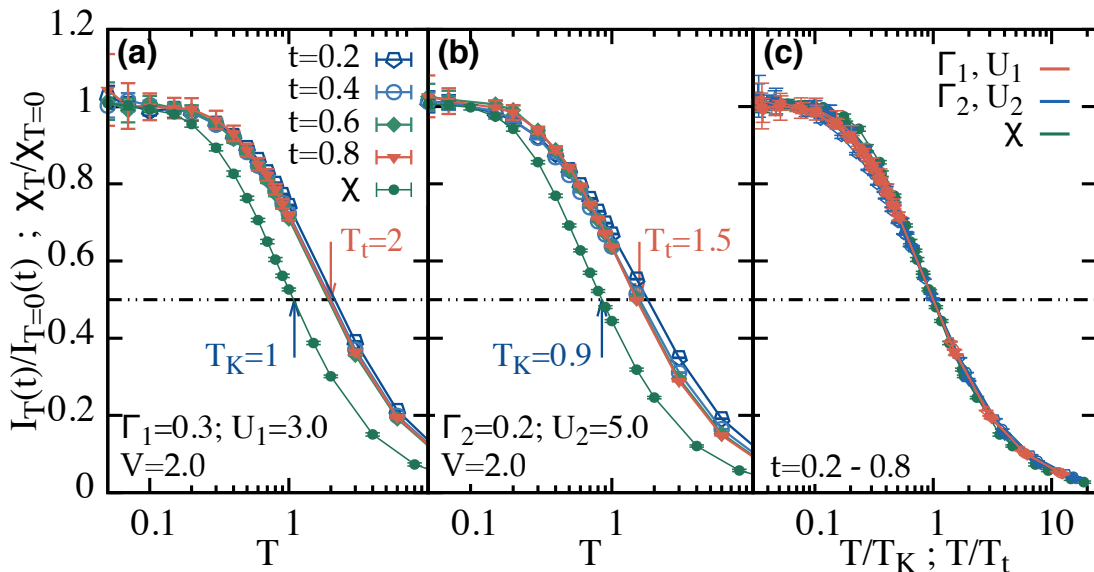
FIGURE 3.6: Normalized transient current $I_T(t)/I_{T=0}(t)$ and static magnetic susceptibility $\chi_T/\chi_{T=0}$ as a function of temperature T for a set of times at $V = 2$, $\varepsilon_d = 0$, $D = 5$ and (a) $\Gamma = 0.3$, $U = 3$; (b) $\Gamma = 0.2$, $U = 5$. Dashed line: value of $1/2$. Vertical arrows: crossing points T_K (susceptiblity) and T_t (current). (c) $I_T(t)/I_{T=0}(t)$ and $\chi_T/\chi_{T=0}$ (all points from panels (a) and (b)) rescaled as a function of T/T_t and T/T_K correspondingly.

values, extracted from the converged low-T data [1]. χ_T is defined as a response to the infinitesimal local magnetic field h, $\chi_T = \left.\frac{d\langle n_\uparrow - n_\downarrow \rangle}{dh}\right|_{h\to 0}$ and is time-independent for $V = 2$. Both quantities saturate at $T \lesssim 0.2$, which we identify with Kondo behavior. The temperatures, at which current and magnetic susceptibility reach half of its zero-T value are the estimates for the Kondo temperature T_t and T_K respectively [77, 87]. We attribute the difference between T_t and T_K to the applied voltage $V = 2$. Being rescaled as the function of T/T_t and T/T_K all plots collapse on the single curve, as depicted in panel (c). This shows that Kondo behavior can be detected based purely on short-time transient dynamics with these parameters.

We proceed with studying the impact of the magnitude of the applied bias voltage. Fig. 3.7 shows the time dependence of the quantum dot occupancy (a) and current (b) at a range of voltages between 0.8 and 10. At voltages $V \leq 2$ (close to linear response) the occupancy retains its equilibrium value and the current

---

[1]The value used is averaged over the T-independent plateau at low temperatures, consisting of points within 2% of the mean value.
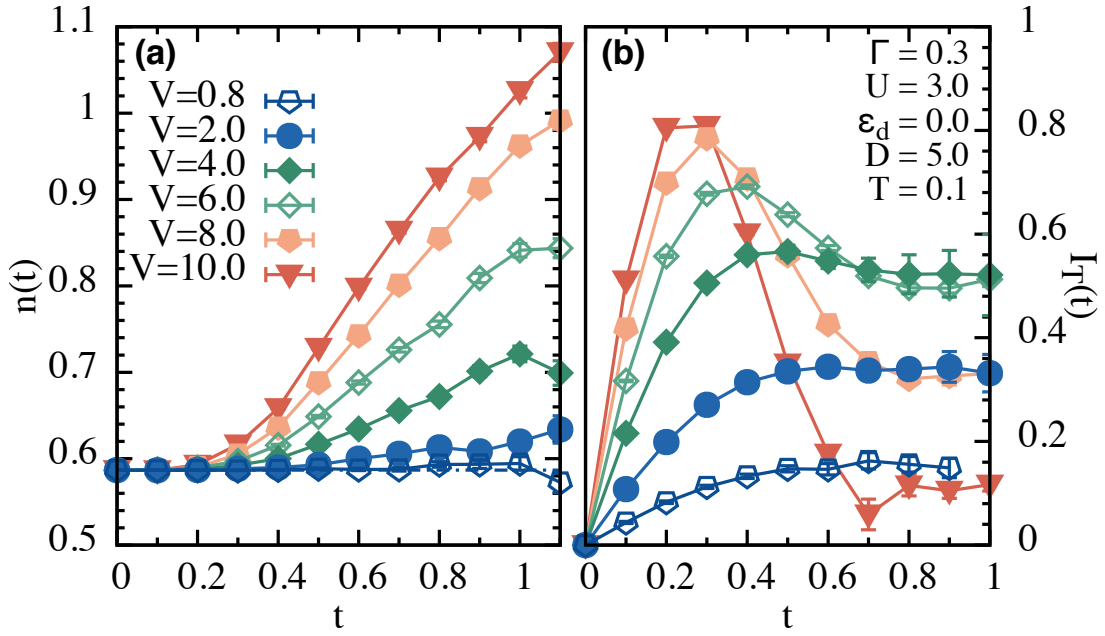
FIGURE 3.7: (a) Dot occupancy and (b) current at $U = 3, \varepsilon_d = 0, \Gamma = 0.3$, $D = 5$ and temperature $T = 0.1$ for voltages $V = 0.8, 2, 4, 6$ (equal to $2U$), 8, and 10 (equal to $2D$).

shows a monotonic rise and saturation to the steady state value, which increases with the applied voltage. Larger voltages $V > 2$ demonstrate linear response behavior only at small times $t < 0.3$. At larger times the nonlinear behavior is visible: the current decreases to the steady state value, which becomes smaller with applied V, illustrating the breakdown of conductance at large voltages.

The temperature dependence of the current outside of the linear response regime is analyzed in Fig. 3.8. Panel (a) shows $I_T(t)/I_{T=0}(t)$ at $V = 6$ as a function of temperature T. Different traces show different transient times, between 0.2 (1 ps) and 1 (4 ps). Similarly to the $V = 2$ case (Fig. **??**), the current exhibits the low temperature saturation at all times. The Kondo effect is therefore visible in transient dynamics for all voltages. Outside linear response, the temperature T_t at which the current saturates is strongly time-dependent. At short times (panel (b)) T_t has the same value for all voltages. As time increases T_t increases by $\approx 60\%$ and reaches its steady state value of $T_t \simeq 2.9$ for $V = 6$ (c). Further increase of the voltage results in a non-monotonic temperature dependence of the current [95].
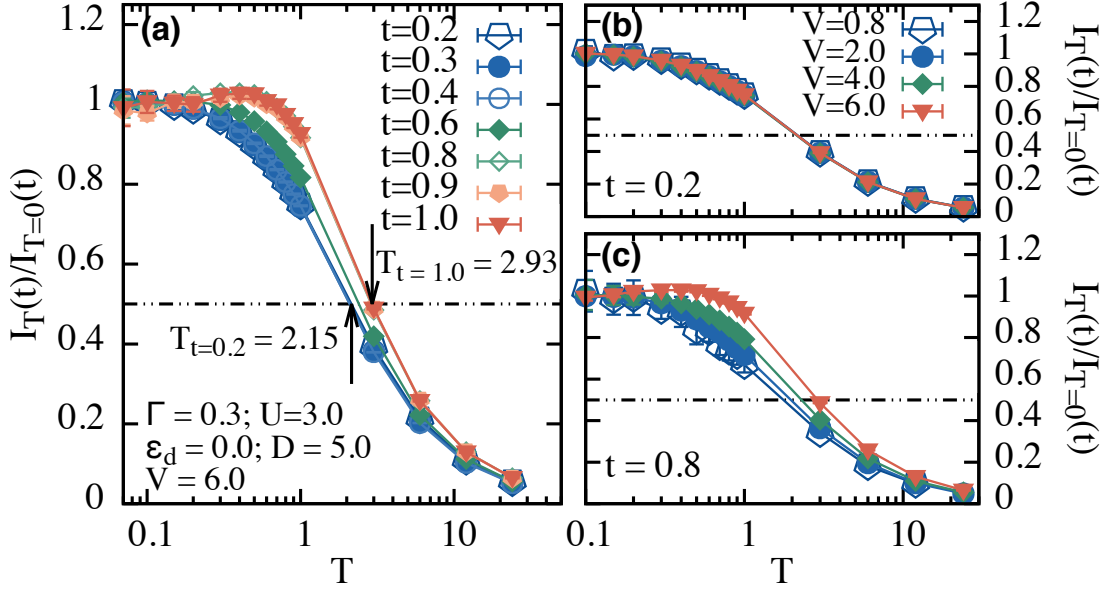
FIGURE 3.8: (a) Normalized current $I_T(t)/I_{T=0}(t)$ as a function of T at $t = 0.2, 0.3, 0.4, 0.6, 0.8, 0.9, 1.0$ and $U = 3, \varepsilon_d = 0, \Gamma = 0.3$, $D = 5$ and $V = 6$. Dashed line: value of $1/2$. (b) Normalized current $I_T(t)/I_{T=0}(t)$ as a function of T at $t = 0.2$ and (c) $t = 0.8$ for different V.
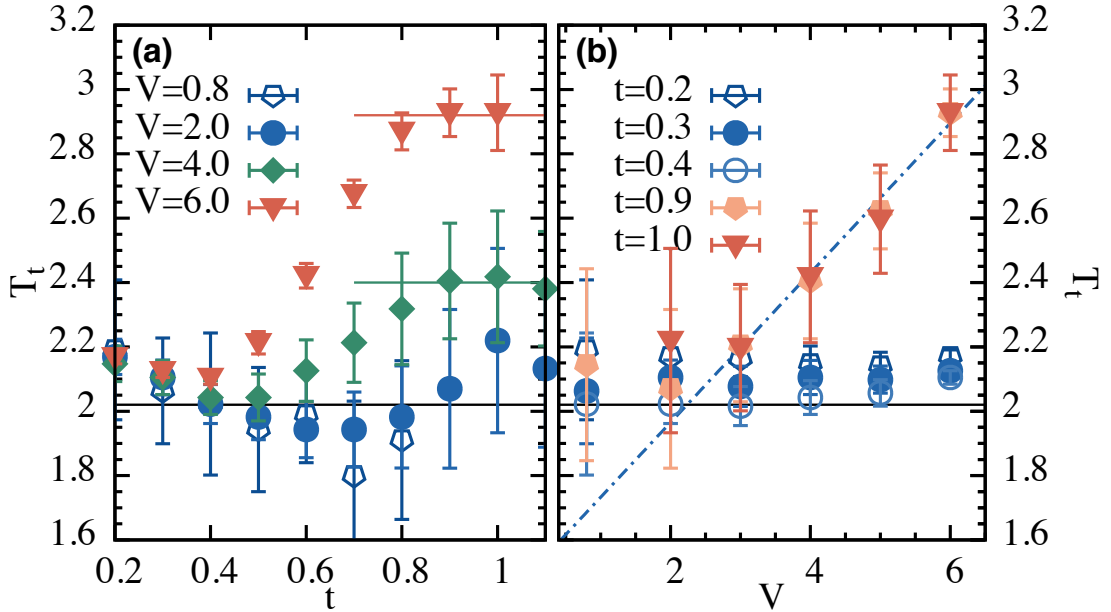
FIGURE 3.9: (a) Current saturation temperature T_t (T at half of zero-temperature current value) as a function of t at different V at $U = 3, \varepsilon_d = 0, \Gamma = 0.3$, $D = 5$. Solid lines: estimates of the steady-state T_t. (b) T_t as a function of V at a set of t. Dashed line: linear fit at $V > 2$.

In Fig. 3.9 we show the time (a) and voltage (b) evolution of T_t. For small voltages, there is no time-dependence of T_t. In contrast, as V is increased up to $2U$, T_t rapidly rises and equilibrates. Estimates of the steady-state T_t as defined by the value at which the current reaches half of its low-T value for $V = 2, 4, 6$ are given by the horizontal lines. Fig. 3.9b shows a separation of short- and long-time behavior: no change in T_t is observed for short times $t \leq 0.4$ (1.5 ps), whereas T_t in the steady state is found to be increasing with V for $V > 2$ in agreement with experiments [94] and predictions from the real time renormalization group [95].

To conclude, we have described the transient dynamics of a quantum dot in the mixed valence regime following the instantaneous application of a bias voltage in a range of temperatures below and above the Kondo temperature T_K. We have observed the full dynamics of the system from equilibrium to steady state. At all times and all voltages below the lead bandwidth, the current saturates at low temperature, exhibiting Kondo behavior. The current saturation temperature T_t describes the interplay of non-equilibrium (applied voltage) and strong Kondo correlations in the system. Outside of the linear response regime T_t has a strong time dependence and connects the equilibrium Kondo temperature to the increased steady state value [94, 95].

The results presented here are exact within the error-bars and the current and time-dependent T_t are directly accessible in time-resolved experiments. The dynamics of the mixed valence system is fast - the equilibration occurs on a picosecond scale. We believe that the same physics can be observed at much larger time scales by lowering the level spacing ε_d and, consequently, entering the Kondo regime, thereby decreasing T_K and exponentially increasing the relaxation time $\tau \propto \exp(-T_K)$ [64].

Chapter 4

The Inchworm Algorithm as an Impurity Solver

The Anderson impurity model [16] with time-dependent parameters or multiple baths at different thermodynamic parameters [101] is one of the simplest fermionic non-equilibrium quantum problems. The model contains localized impurity states coupled to a non-interacting bath and appears in a wide range of contexts, including impurities embedded into a host material [16], confined nanostructures [17] and molecules adsorbed on surfaces [18, 19].

Impurity models also appear as auxiliary models in non-equilibrium dynamical mean field theory [8, 34, 35]. A solution of the dynamical mean field equations requires the calculation of two-time quantities such as Green's functions, for temperatures low enough that the impurity model exhibits Kondo behavior and—in quench setups—for times long enough that a new equilibrium or steady state behavior can be observed [101]. Additionally, real-time solvers are of a great interest in the equilibrium study as well. It is in particular useful for obtaining spectral functions from the real time data, eliminating the need for the numerically ill-conditioned analytical continuation procedure of imaginary time data. In Sec. 3.4, we have seen that the severe dynamical sign problem is the main limiting factor of preventing the simulation from accessing accurate information

at longer times. Hence, methods that are numerically exact and offer a stringent assessment of uncertainties are greatly desired.

In this chapter, we present a numerical method that fulfills all of these criteria. It can treat general time-dependent setups of Anderson impurity models with any number of baths. It captures initial correlations of equilibrated states, and it is controlled in the sense that there is a small parameter that can be tuned in practice in order to approach the exact solution.

Our method is a generalization of the inchworm [102] quantum Monte Carlo (QMC) method, which was originally formulated on the forward-backward Keldysh contour, to the full Keldysh contour with an additional temperature or imaginary-time branch. This enables the treatment of interacting equilibrium initial states. The Inchworm Monte Carlo algorithm is based on a reformulation of the nonequilibrium hybridization expansion [55, 65, 66, 103] discussed in the previous chapter in terms of bare and interacting atomic state propagators, which are iteratively generated. Its main advantage as compared to other Monte Carlo methods is that the dynamical sign problem [103], which causes an exponential amplification of uncertainties as a function of real time, is mitigated or overcome [102], providing access to substantially longer times.

In the following, we first introduce the inchworm idea and formalism in Sec. 4.1. It provides a way of measuring propagators and Green's functions at an iterative manner, from shorter times to longer times. In Sec. 4.2, we modify our sampling using the Wang-Landau algorithm [104, 105] in order to get enough normalization overlaps. We compare our results with bare QMC calculations and show spectral functions in various parameter regimes in Sec. 4.3 [106].

4.1 Inchworm Expansion on the Keldysh contour

4.1.1 Propagators

As illustrated in Sec. 3.3.1, the hybridization expansion can be formulated in terms of dressed atomic state propagators $\hat{P}_s$, where $\hat{P}_s(t_1, t_2)$ is defined in Eq. (4.7) and contains all possible combinations of hybridization events between the two times t_1 and t_2 that leave the system in atomic state $|s\rangle$ at times t_1 and t_2. Propagators are "contour-causal" by construction, *i.e.* all contributions to a propagator $\hat{P}_s(t_1, t_2)$ are given in terms of propagators and hybridization events with time indices between t_1 and t_2. And the time-dependent expectation values of operators are expressed as in Eq. (3.37):

$$\langle \hat{O}(t) \rangle = \frac{1}{Z} \mathrm{Tr} \left\{ e^{-\beta \hat{H}} e^{i\hat{H}t} \hat{O} e^{-i\hat{H}t} \right\} = \frac{i}{\tilde{Z}_D} \mathrm{Tr}_D \left\{ \hat{\xi} \hat{P}(t_+, t_-) \hat{O} \right\} \qquad (4.1)$$

The expression $e^{-i\hat{H}t}$ is a symbolic form that can represent either time-independent or time-dependent evolutions, t_+ denotes the time t on forward branch $\mathcal{C}_+$ and t_- denotes t on backward branch $\mathcal{C}_-$. Using the cyclic property of the trace, we choose a time-ordering on the contour such that the "minus" branch describing the evolution $e^{iHt_{\max}}$ from $t_{\max}$ to 0 occurs before the equilibrium Matsubara branch from 0 to $-i\beta$, which occurs before the "plus" branch $e^{-iHt_{\max}}$ from 0 to $t_{\max}$, rather than the usual ordering $e^{-\beta \hat{H}} e^{i\hat{H}t} \hat{O} e^{-i\hat{H}t}$, allowing us to insert single-time operators at the beginning or end (rather than in the middle) of the contour:

$$\langle \hat{O}(t) \rangle = \frac{1}{Z} \mathrm{Tr} \left\{ e^{-i\hat{H}t} e^{-\beta \hat{H}} e^{i\hat{H}t} \hat{O} \right\} = \frac{i}{\tilde{Z}_D} \mathrm{Tr}_D \left\{ \hat{\xi} \hat{P}(t_+, t_-) \hat{O} \right\} \qquad (4.2)$$
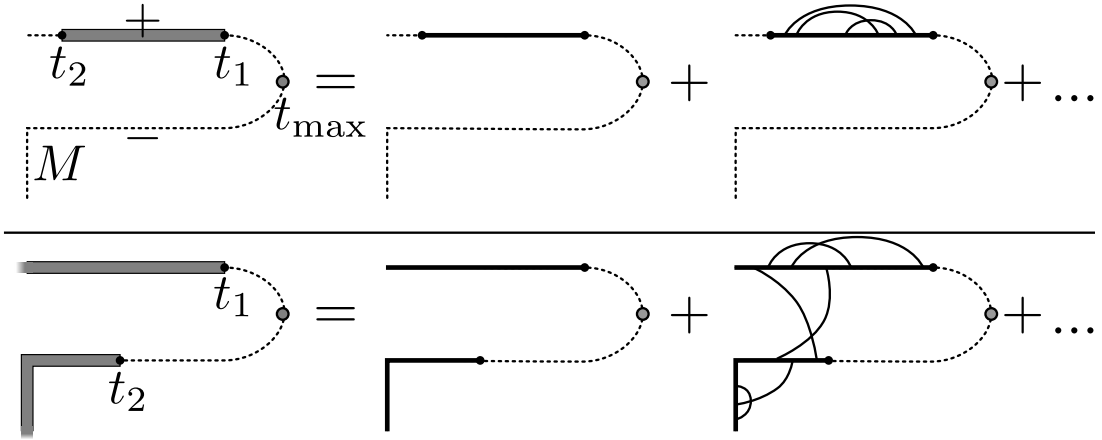
FIGURE 4.1: Illustration of hybridization expansion diagrams on the Keldysh contour with equilibrium branch. Top panel: Full propagator on the "+" branch from t_2 to t_1 (left diagram) is given by the the bare propagator (middle diagram) plus all possible combinations of hybridization events between t_2 and t_1, one of which is drawn as the right diagram. Bottom panel: Full propagator spanning the "−", equilibrium, and "+" contour containing diagrams that span the contour.

This results in exactly the twisted contour ordering as illustrated in Fig. 2.3 and defines the ordering of dressed propagators that need to be evaluated:

$$\hat{P}_s(t_1, t_2) \qquad \text{for all } t_1 \succ t_2 \tag{4.3}$$

Propagators on the Keldysh contour are illustrated graphically in Fig. 4.1: The top panel shows a propagator $\hat{P}_s$ on the upper "+" branch, with $t_1 \succ t_2$, which is given by the "bare" atomic state propagation defined in Eq. (2.62) in the absence of hybridization events (middle diagram) and all possible connected and disconnected combinations of hybridization lines, one of which is shown as the diagram on the right. The bottom panel shows a propagator starting on the lower "'−" branch, propagating along the equilibrium branch, and continuing on the upper "+" branch. It contains hybridization lines connecting the real time "+" and "−" branches to the equilibrium branch, thereby introducing thermal entanglement into the system.

The contour-causality of the propagators can be used to construct propagators

84
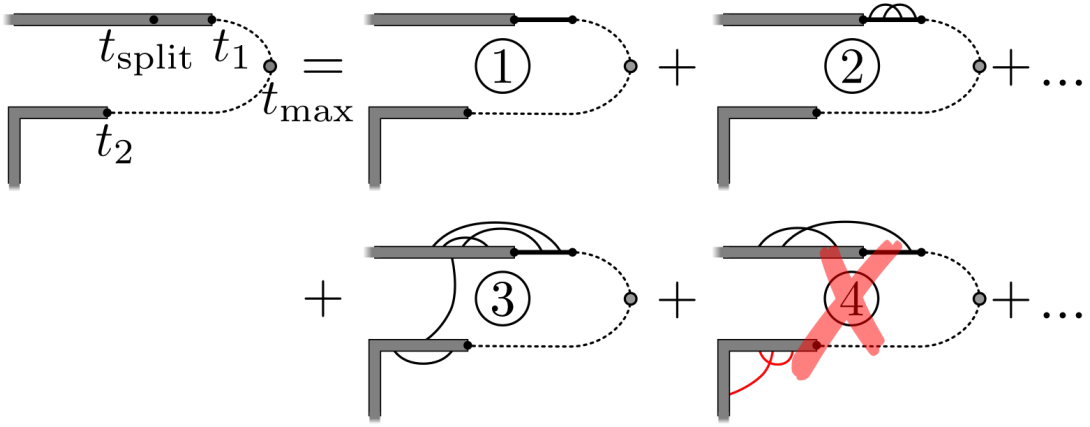
FIGURE 4.2: Illustration of the diagrams generating a propagator in the inchworm formalism. The propagator from t_2 to t_1 (left diagram) is, at the lowest inchworm order, given by the propagator from t_2 to t_{split} joined with a bare propagator from t_{split} to t_1 ①. In higher order diagrams, hybridization lines are either contained in the region between t_{split} and t_1 as in ②; or, connected by crossing to an endpoint in that region, as in ③. Diagrams with inclusions not obeying this rule, such as ④, are already included in the inchworm propagator and should not be summed over.

over longer time intervals from previously computed propagators over shorter intervals. The concept is illustrated in Fig. 4.2, which shows how a propagator from t_2 to t_1 can be expressed as a propagator from time t_2 to t_{split} multiplied by the bare propagation from time t_{split} to t_1 (diagram ①), supplemented by diagrams which have hybridization events between time t_{split} and t_1. Of those, diagram ② only has hybridization events between t_{split} and t_1; diagram ③ has hybridization events starting between t_{split} and t_1 and reaching backward in time to a position between t_2 and t_{split}, along with additional hybridization lines that cross those lines. In contrast, diagram ④ contains a separate cluster of hybridization lines (red online) which are already contained in a propagator, and is therefore not part of the series of diagrams to be summed in order to construct the propagator over the full interval.

Therefore, the inchworm expansion reuses propagators obtained at shorter time intervals and the dressed propagator $\hat{P}(t_1, t_2)$ is given by a sampling of MC

weights Eq. (3.34) with

$$w_{\text{loc}} = (-1)^{\mathcal{P}}(-1)^k \langle s|\hat{\xi}\hat{p}(t_1, t'_{k+1}) \ldots \hat{p}(t'_l, t_{\text{split}})\hat{P}(t_{\text{split}}, t'_{l+1}) \ldots \hat{P}(t'_{k-1}, t'_k)\hat{P}(t'_k, t_2)|s\rangle$$

$$(4.4)$$

$$w_{\text{hyb}} = \sum_{\text{connected}} (-1)^{\text{sign}(D_m)} D_m(t'_1 \ldots t'_{2n}) \qquad (4.5)$$

where $t'_1, \ldots, t'_{2n}$ with $t'_1 \succ \ldots \succ t'_{2n}$ are the time points of the newly inserted hybridization lines in the inchworm MC simulation. Times $t'_{k+1}, \ldots, t'_l$ are in $[t_{\text{split}}, t_1]$ so bare atomic propagators $\hat{p}$ are used. The w_{hyb} in bare QMC in Eq. (3.6) used to be

$$\det \Delta(t'_1 \ldots t'_{2n}) = \sum_{\text{all}} (-1)^{\text{sign}(D_m)} D_m(t'_1 \ldots t'_{2n}) \qquad (4.6)$$

but now it evaluates only the subset of "connected" diagrams as illustrated in Fig. 4.2 and D_m denotes a possible permutation/diagram in the determinant.

Computing corrections to known propagators rather than computing the entire propagator at once is efficient if the propagator consists of many short-time clusters of hybridization lines, so that most of the interaction contribution can be absorbed in previously computed propagators. In the case of the forward-backward Keldysh contour, it was shown that at least for some parameters this procedure changed the scaling from exponential to polynomial, overcoming the dynamical sign problem [102].

As evident in Fig. 4.2 and Eq. (4.4), computing the propagator from time t_2 to time t_1 requires knowledge of all propagators from t'' to t', with $t_2 \prec t'' \prec t' \prec t_{\text{split}}$. Fig. 4.3 shows the set of known propagators (blue) needed to compute a new propagator (red), in this case with start time on the "−" contour and end time on the "+" contour. This step, which we call "inching", could be repeated any number of times to generate longer propagators from sets of shorter ones. This suggests an iterative algorithm, graphically illustrated in Fig. 4.4: the inchworm quantum Monte Carlo method [102].
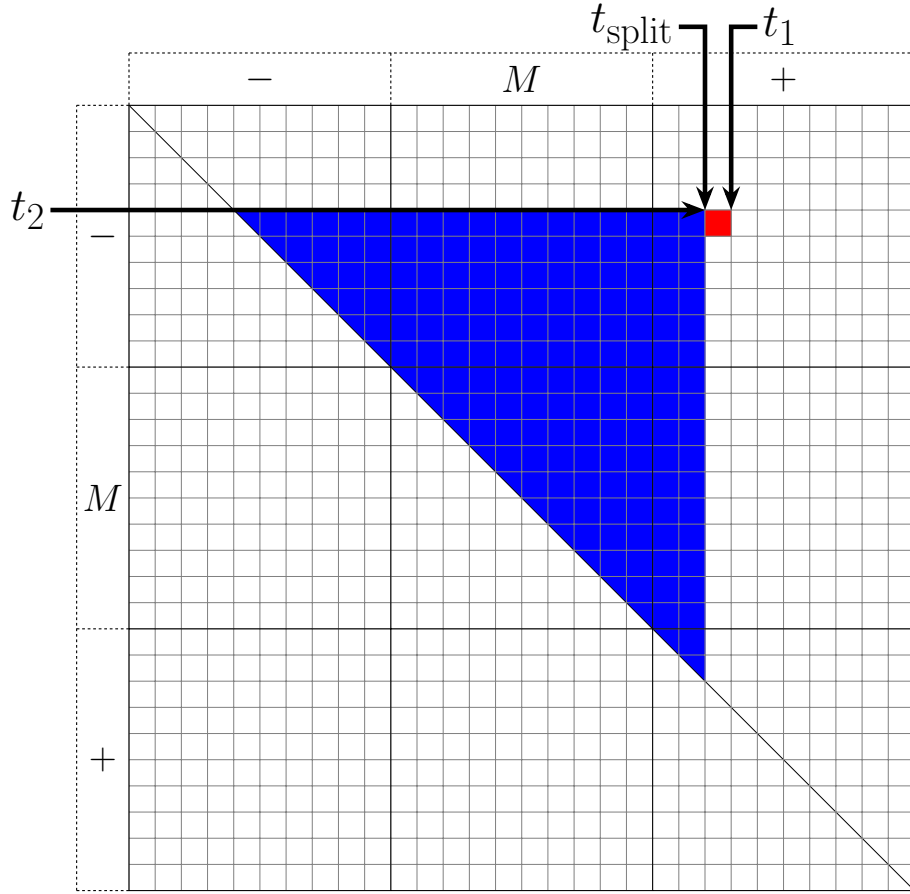
FIGURE 4.3: Illustration of the causal structure of the inchworm propagators. A propagator $\hat{P}_s(t_1, t_2)$ (red) depends on all propagators with start point on or after t_2 and end point up to t_{split} (blue).

The algorithm begins with the discretization of the backward, equilibrium, and forward branches of the Keldysh contour into N equidistant time slices with distance Δt, enumerated by $k = 1, \ldots, N$. Same-time propagators between identical contour times (which lie on the main diagonals of the matrices in Fig. 4.3) are trivial, and can be evaluated analytically. In Fig. 4.4 and Fig. 4.5, these propagators are shown in green. Next, propagators for short time differences $n\Delta t$ (with n a small integer chosen to be large enough that smoothly interpolated functions can be obtained) can be computed straightforwardly using the bare QMC method, which is efficient for short times. There are Nn such propagators, with time arguments between times $k\Delta t$ and $(k + n)\Delta t$. In Fig. 4.5, the minimal number $n = 1$ is taken and the result is shown as cells with circles. In the next step and each following step, propagators from any time $k\Delta t$ to any time
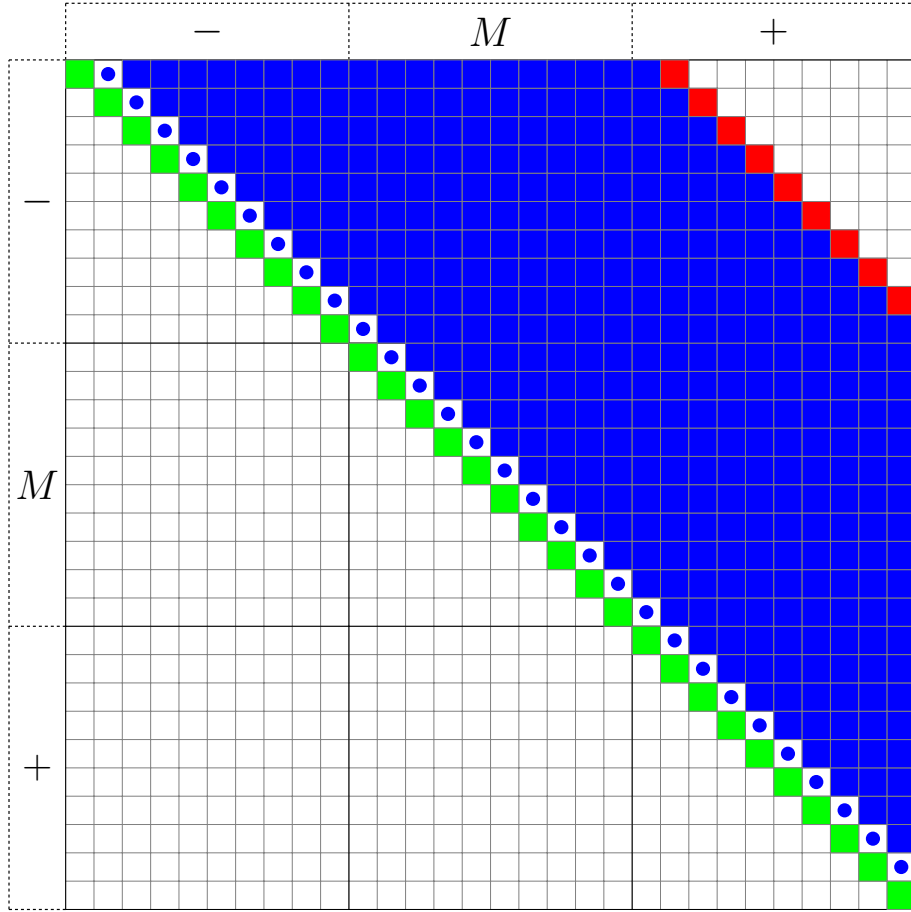
FIGURE 4.4: Illustration of the inchworm algorithm showing the values known at some step (blue) and values that can be computed using known values in blue (red). Green cells are trivial and can be evaluated analytically and cells with circles are computed with the bare algorithm. Evaluation of the full propagator proceeds diagonally towards the upper right corner from the initial values as dictated by the causal structure of the propagators.

$(k+n+1)\Delta t$ need to be computed. We obtain them by stochastically generating all diagrams illustrated in Fig. 4.2, where t_2 is $k\Delta t$, t_1 is $(k+n+1)\Delta t$, and t_{split} is set to $(k+n)\Delta t$. We then increase n by 1 and iterate the last step of the procedure, simulating propagators from $k\Delta t$ to $(k+n+1)\Delta t$ based on any propagator with times between $k\Delta t$ and $k+a\Delta t$ at each iteration, until the propagator from time 0 to time $N\Delta t$ is generated (top right corner of Fig. 4.4).

Fig. 4.5 shows the inchworm procedure step by step, with the elements participating in each particular step highlighted in red. This illustrates the trivial
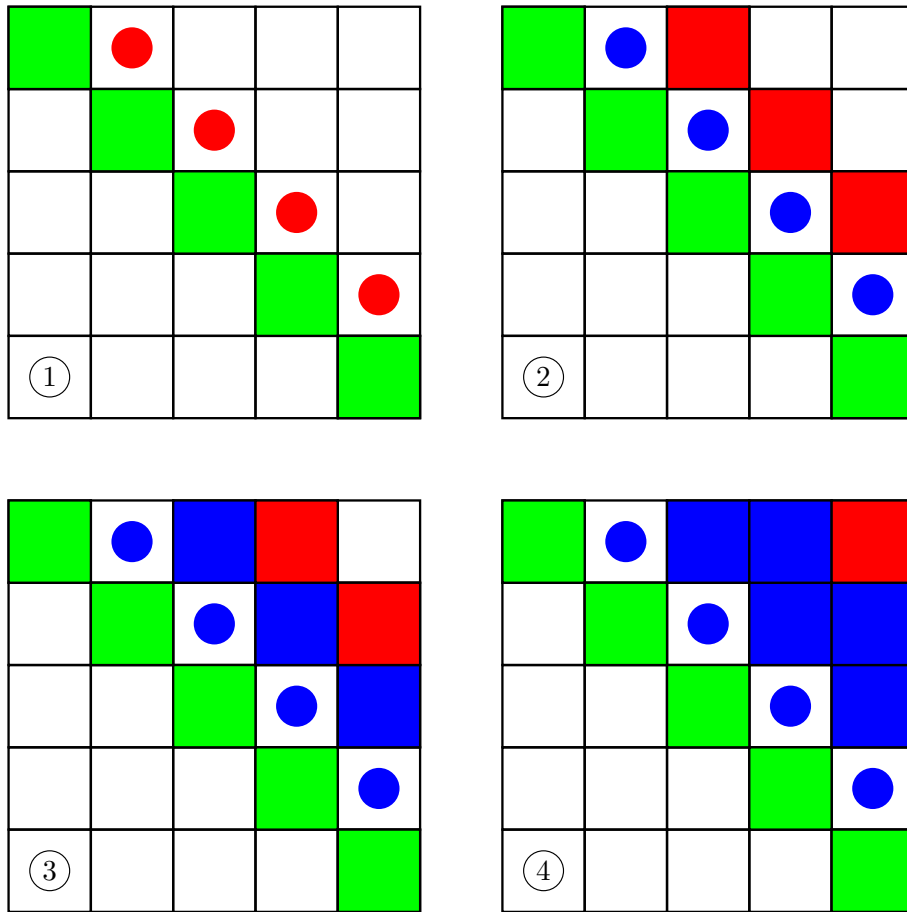
FIGURE 4.5: A step-by-step illustration of the algorithm. Cells with circles are evaluated with the bare algorithm and solid cells with inchworm. Red cells represent propagators computed at a given step, while blue cells represent already computed propagators. Green cells in all panels are trivial and can be evaluated analytically.

elements (in green), the initial bare step (circles), and two inchworm steps (solid) that gradually extend the known propagators along the Keldysh contour.

The complete procedure requires performing $O(N^2)$ interdependent Monte Carlo simulations of diagrams, each of which is represented by a cell in the matrices in Fig. 4.4. However, at any given step all the computations corresponding to cells which can currently be evaluated—*e.g.*, the cells colored in red at every step of Fig. 4.5)—can be evaluated simultaneously and independently. Furthermore, since the computation of each individual cell is a *regular* QMC simulation, the work it entails can also be trivially split between any number of compute nodes.
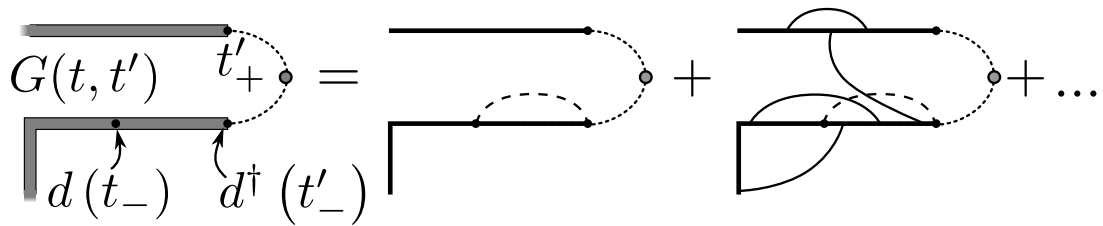
FIGURE 4.6: Illustration of the diagrams generating a Green's function. The Green's function $G(t, t')$ is given at lowest order by the middle diagram, where the dashed line is a virtual hybridization line from the Green's function creation/annihilation operators. Higher order diagrams contain at least one hybridization line that crosses the virtual line. A sample term is shown in the right diagram.

The inchworm algorithm therefore lends itself to extremely efficient parallelization strategies. However, since after every step at least some data synchronization between cells is required, it is not "embarrassingly parallel" in the sense of standard Monte Carlo methods.

4.1.2 Green's functions

Currents and Green's functions are two-time observables that cannot be obtained from knowledge of just the local (population) propagators. However, as we have seen in Sec. 3.3.3, the expansion for Green's functions is given by all possible contractions of hybridization lines in the presence of two additional local operators. Therefore, we define the *Green's function propagators* to be

$$\hat{P}_{G_\sigma^>} (t_1, t_2)_{s_1 s_2} = - i \left\langle s_1 \left| e^{-i\hat{H}t_2} e^{-\beta\hat{H}} e^{i\hat{H}t_1} \hat{d}_\sigma e^{-i\hat{H}(t_1 - t_2)} \hat{d}_\sigma^\dagger \right| s_2 \right\rangle \qquad (4.7)$$

$$\hat{P}_{G_\sigma^<} (t_1, t_2)_{s_1 s_2} = - i \left\langle s_1 \left| e^{-i\hat{H}t_2} e^{-\beta\hat{H}} e^{i\hat{H}t_1} \hat{d}_\sigma^\dagger e^{-i\hat{H}(t_1 - t_2)} \hat{d}_\sigma \right| s_2 \right\rangle \qquad (4.8)$$

with $t_1 > t_2$. Similar to the population propagators described in Sec. 4.1.1, we can sample the Green's function using expressions in Eq. (3.57) and the Monte

Carlo weights of these two Green's function propagators are then given by

$$\hat{P}_{G_\sigma^>,s}(t,t') = \sum_{n=0}^{\infty} \sum_{o_i=d,d^\dagger} \int_0^{-i\beta} dt_1 \cdots \int_t^{t_{k-1}} dt_k \cdots \int_{t'}^{t_{l-1}} dt_l \cdots \int_0^{t_{2n-1}} dt_{2n}$$

$$\cdot P_{G_\sigma^>}(\{o_1 \ldots o_{2n}, t_1 \ldots t_{2n}\}, (t,t'), \mathcal{P}, s) \tag{4.9}$$

with

$$P_{G_\sigma^>}(\{o_1 \ldots o_{2n}, t_1 \ldots t_{2n}\}, (t,t'), \mathcal{P}, s) = i^{n+1} w_{\text{loc},G_\sigma^>} w_{\text{hyb},G_\sigma^>} \tag{4.10}$$

$$w_{\text{loc},G_\sigma^>} = (-1)^{\mathcal{P}} (-1)^l \left\langle s \left| \hat{\xi} \hat{P}(t',t_{l+1}) \cdots \hat{P}(t_k,t) \, \hat{d}_\sigma \hat{P}(t,t_{k+1}) \cdots \hat{P}(t_l,t') \, \hat{d}_\sigma^\dagger \right| s \right\rangle \tag{4.11}$$

$$w_{\text{hyb},G_\sigma^>} = \sum_{\text{all-crossing}} (-1)^{\text{sign}(D_m)} D_m(t_1 \ldots t_{2n}) \tag{4.12}$$

and

$$\hat{P}_{G_\sigma^<,s}(t,t') = \sum_{n=0}^{\infty} \sum_{o_i=d,d^\dagger} \int_0^{-i\beta} dt_1 \cdots \int_t^{t_{k-1}} dt_k \cdots \int_{t'}^{t_{l-1}} dt_l \cdots \int_0^{t_{2n-1}} dt_{2n}$$

$$\cdot P_{G_\sigma^<}(\{o_1 \ldots o_{2n}, t_1 \ldots t_{2n}\}, (t,t'), \mathcal{P}, s) \tag{4.13}$$

with

$$P_{G_\sigma^<}(\{o_1 \ldots o_{2n}, t_1 \ldots t_{2n}\}, (t,t'), \mathcal{P}, s) = i^{n+1} w_{\text{loc},G_\sigma^<} w_{\text{hyb},G_\sigma^>} \tag{4.14}$$

$$w_{\text{loc},G_\sigma^<} = (-1)^{\mathcal{P}} (-1)^l \left\langle s \left| \hat{\xi} \hat{P}(t',t_{l+1}) \cdots \hat{P}(t_k,t) \, \hat{d}_\sigma^\dagger \hat{P}(t,t_{k+1}) \cdots \hat{P}(t_l,t') \, \hat{d}_\sigma \right| s \right\rangle \tag{4.15}$$

$$w_{\text{hyb},G_\sigma^<} = \sum_{\text{all-crossing}} (-1)^{\text{sign}(D_m)} D_m(t_1 \ldots t_{2n}) \tag{4.16}$$

where w_{hyb} terms sample "all-crossing" diagrams in which every hybridization line has to either cross with the Green's function $\hat{d}_\sigma$–$\hat{d}_\sigma^\dagger$ line attached in the configuration, or cross with such hybridization lines that cross with the Green's function line. A Green's function propagator diagram is illustrated in Fig. 4.6. In terms of the interacting propagators obtained in Fig. 4.1, the Green's function is given, to lowest order, by a product of propagators (middle diagram of Fig. 4.6).

Higher order corrections consist of hybridization lines crossing the two Green's function operators, and all possible additional crossing lines. The right panel of Fig. 4.6 shows an example of one such diagram. After obtaining the Green's function propagators, the interacting contour-ordered Green's function $G_\sigma(t, t')$ is constructed using the following formula

$$
G_\sigma(t, t') = \begin{cases}
\frac{1}{\tilde{Z}_D} \mathrm{Tr}_D \left\{ \hat{\xi} \hat{P}_{G_\sigma^<}(t, t') \right\} & |t| > |t'| \ \& \ t \gtreqless t' \ \& \ t \succsim t' \\
\frac{1}{\tilde{Z}_D} \mathrm{Tr}_D \left\{ \hat{\xi} \hat{P}_{G_\sigma^>}(t, t') \right\} & |t| < |t'| \ \& \ t \gtreqless t' \ \& \ t \succsim t' \\
-\frac{1}{\tilde{Z}_D} \mathrm{Tr}_D \left\{ \hat{\xi} \hat{P}_{G_\sigma^<}(t, t') \right\} & |t| > |t'| \ \& \ t \lesseqgtr t' \ \& \ t \succsim t' \\
-\frac{1}{\tilde{Z}_D} \mathrm{Tr}_D \left\{ \hat{\xi} \hat{P}_{G_\sigma^>}(t, t') \right\} & |t| < |t'| \ \& \ t \lesseqgtr t' \ \& \ t \succsim t'
\end{cases}
\tag{4.17}
$$

where $|t| \gtreqless |t'|$ denotes the real-time magnitude comparison and the last two comparisons in each case mean that either the upper or the lower signs are fulfilled at the same time, for example, $t > t' \ \& \ t \succ t'$ or $t < t' \ \& \ t \prec t'$ for the first case.

In contrast to the case of single-time propagators, where we iteratively construct diagrams at longer times using diagrams at shorter times, here we generate all Green's function diagrams at once, simulating them in parallel. And currents can be obtained through the Green's functions by Eq. (3.48).

4.1.3 Connections to self-consistent approximate methods

Each individual inchworm step is exact for any Δt, provided that all intermediate propagators are exactly known. In practice the propagators, generated by previous inchworm steps or a bare calculation, are interpolated on a grid with discretization Δt. This discretization introduces errors for large Δt, especially where propagators change on a time scale comparable to Δt, and needs to be controlled by extrapolating to $\Delta t \to 0$.
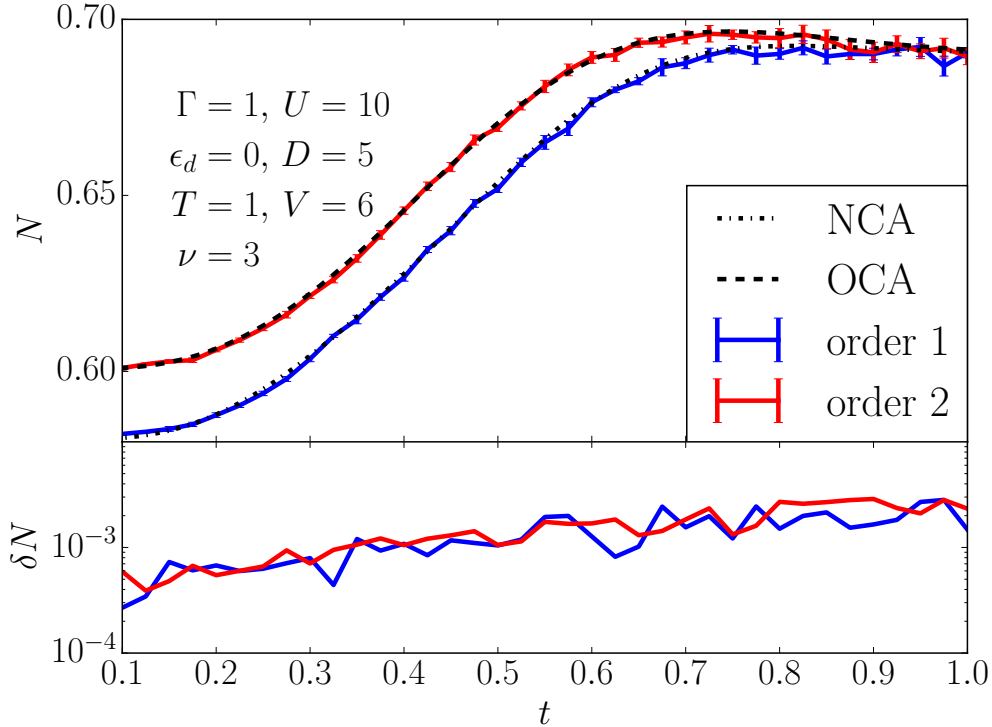
FIGURE 4.7: Top panel: Time evolution of the impurity occupation N after a voltage quench using the non-crossing and one-crossing approximations (NCA and OCA, respectively). Black lines: semi-analytically computed NCA and OCA solutions. Blue line: NCA solution generated from an inchworm expansion truncated to order one. Red line: OCA solution from an inchworm expansion truncated to order 2. Bottom panel: Statistical error estimate of the quantities shown in the upper panel.

In the limit $\Delta t \to 0$, at most one hybridization event will occur between t_{split} and t_1. In this limit, the method simplifies to the semi-analytic "N-crossing" approximations when inchworm diagrams are restricted to low orders [102]. At truncation to order $n = 1$, NCA results in Sec. 2.3.1 are obtained. Truncation to order $n = 2$ yields the OCA in Sec. 2.3.2, the two-crossing approximation (2CA) is generated for order $n = 3$, etc. Fig. 4.7 illustrates agreement within error bars of numerical results for the propagators truncated to $n = 1$ and $n = 2$ to the NCA and OCA approximations. It is shown in Sec. 4.3 that the size of the inchworm error does not strongly depend on time. This implies that for "crossing" expansions on the order of the OCA and above, inchworm Monte Carlo provides an efficient alternative to the direct integration of the equations

of motion.

Continuous-time QMC requires the sampling of diagrams to all orders. In bare expansions very high order diagrams are easily sampled, because (due to Wick's theorem) the sum over all diagrams for a particular configuration of order $2n$, of which there are $n!$, can be written as the determinant of a $n \times n$ matrix and evaluated at polynomial scaling using linear algebra algorithms [64]. However, in bold and inchworm Monte Carlo a factorial number of diagrams must be explicitly summed over at each order, and the cost of enumerating these diagrams quickly becomes prohibitive (evaluating the sum over permutations stochastically leads to a sizable increase in the overall sign problem). We therefore truncate the series at a predetermined maximum order and observe convergence as that order is increased. This corresponds to observing convergence in the hierarchy NCA $\rightarrow$ OCA $\rightarrow$ 2CA $\cdots$, each of which contains an infinite subseries of all the bare diagrams, which extends to infinite order. In the simulations included for this thesis, we typically truncate this hierarchy at order 5–7.

4.2   Normalization and Wang-Landau sampling

Additional technical complications arise when the inchworm algorithm is extended to the full Keldysh contour with the imaginary time branch. Monte Carlo importance sampling does not generate absolute values of observables. Rather, it generates probability ratios, or values up to an unknown normalization constant, as described in Sec. 3.2.2. This normalization can be computed by comparing to a known reference system, for example, a zero or first order diagram, as long as the overlap of the series with that reference $\mathbb{I}_{\mathrm{ref}}(\mathbf{x})$ is large. With the normalization technique in Eq. (3.32) and the "reweighted" measurements in Eq. (3.72), the propagators are given by

$$\frac{\hat{P}_s(t_1, t_2)}{\hat{P}_s^{(\mathrm{ref})}(t_1, t_2)} = \frac{\left\langle \frac{w}{|w|} \right\rangle_{|w|}}{\left\langle \mathbb{I}_{\mathrm{ref}} \cdot \frac{w}{|w|} \right\rangle_{|w|}} \tag{4.18}$$

As shown in the equation, the resummed inchworm propagators $\hat{P}_s(t_1, t_2)$ depend on the sign of the configurations of the reference system in the denominator. Therefore, the overlap between $w(C)$ and $w(C_{\text{ref}})$ is crucial to the precision of the inchworm calculation.

In systems where the low-order diagrams are not important, the overlap with the reference becomes small, causing a variance problem. This problem can be solved by changing the sampling such that regions at low order are visited more often using a generalized ensemble technique. We choose to modify our sampling using the Wang–Landau algorithm [104, 105] to generate a flat histogram in expansion orders. These algorithms, originally designed to overcome ergodicity barriers at first order phase transitions, were previously extended to quantum phase transitions [107] and applied to CT-QMC [108] to compute thermodynamic potentials and overcome ergodicity problems [64, 109].

In order to generate this flat histogram and get the order distribution $o(n)$ for histogram reweighting, a Wang-Landau pre-run is required prior to the Monte-Carlo simulation. The procedure is as follows:

1. Start with $o(n) = 1$, $f = e$, and a histogram of expansion orders $H(n) = 0$ initially.

2. Perform simulations until the histogram $H(n)$ is "flat":

   (a) Attempt a Metropolis update using $w'(\mathbf{x}) = w(\mathbf{x})/o(n)$.

   (b) Increase the histogram at the current order n: $H(n) \leftarrow H(n) + 1$.

   (c) Increase the estimate for $o(n)$ at the current order n: $o(n) \leftarrow o(n) \cdot f$.

3. Once $H(n)$ is flat, e.g. the mean is at least 95% of the maximum, reduce $f \leftarrow \sqrt{f}$.

4. Set the histogram back to zero and repeat. Stop once f reaches a small tolerance.
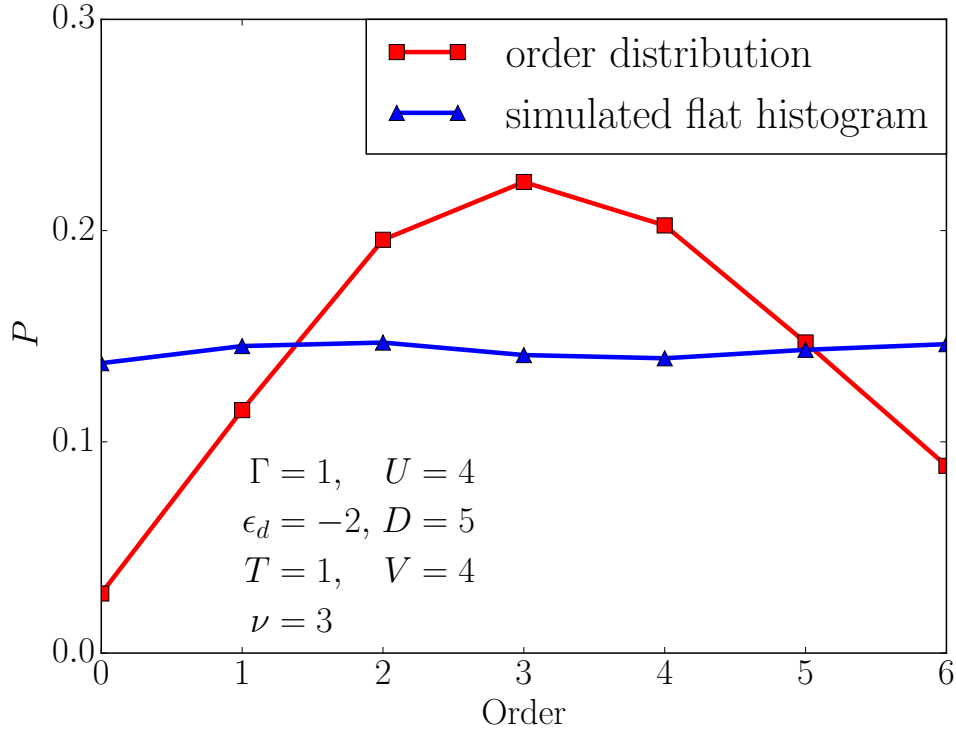
FIGURE 4.8: Order distribution (red) and sampled "flat" histogram (blue) for a Wang–Landau simulation of the inchworm propagators. The large overlap of the reweighted distribution with order zero allows normalization to low order diagrams.

Then it will be advantageous to sample configurations C_n with the new distribution $w'(\mathbf{x}) = w(\mathbf{x})/o(n)$. Then Eq. (4.18) becomes

$$\frac{\hat{P}_s(t_1, t_2)}{\hat{P}_s^{(\mathrm{ref})}(t_1, t_2)} = \frac{\left\langle \frac{w}{|w|} \cdot o(n) \right\rangle_{|w'|}}{\left\langle \mathbb{I}_{\mathrm{ref}} \cdot \frac{w}{|w|} \cdot o(n) \right\rangle_{|w'|}} \tag{4.19}$$

Fig. 4.8 shows the expansion order histogram of an inchworm propagator simulation for a representative set of parameters $\Gamma = 1$, $U = 4$, $\epsilon_d = -2$, $D = 5$, $T = 1$ and $V = 4$ up to order 6. The red line shows the contribution of the absolute value of the diagrams at each order to the inchworm propagator. It is evident that diagrams at higher order acquire higher weight, and that diagrams near order zero are strongly suppressed, making normalization to low order diagrams difficult. If, in contrast, the sampling weights are changed to produce a

'flat' order distribution (see blue line in Fig. 4.8), each expansion order is visited equally often, and normalization to low order diagrams is possible.

4.3   Results

In this section, we present the simulation results of the inchworm impurity solver applied on the single impurity Anderson model Eq. (1.2a). We consider two cases: the equilibrium case, where none of the parameters are time-dependent and $V(t) = 0$; and the case of a symmetric voltage quench $V(t) = V\theta(t)$, with $\theta(t)$ being a Heaviside step function. In the second case, the system is in equilibrium for $t < 0$, and for $t > 0$ the lead levels ε_k are instantaneously moved to $\varepsilon_k \pm \frac{V}{2}$, with the sign depending on the lead index α. The parameters $\mathcal{V}_k^\alpha$ and ε_k are chosen such that

$$\Gamma^\alpha(\omega) = \pi \sum_k |\mathcal{V}_k^\alpha|^2 \delta(\omega - \varepsilon_k) \qquad (4.20)$$

describes a flat band centered at zero with a Fermi function-like cutoff,

$$\Gamma^\alpha(\omega) = \frac{\Gamma^\alpha}{\left(1 + e^{\nu(\omega - D)}\right)\left(1 + e^{-\nu(\omega + D)}\right)}. \qquad (4.21)$$

Throughout the results section we use $\Gamma^\alpha = \Gamma = 1$; half-bandwidth $D = 5$; smoothing factor $\nu = 3$ (unless specified as $\nu = 10$); $U = 4$ and $U = 10$; temperature $T = 1$. And we are predominantly interested in obtaining observable estimates for densities, currents, and Green's functions.

4.3.1   Populations

The top panel of Fig. 4.9 shows results for the time-evolution of the density after a voltage quench of an impurity with parameters $\Gamma = 1$, $U = 10$, $\epsilon_d = 0$, $D = 5$, $T = 1$ and $V = 6$. Black triangles denote values obtained in a bare QMC simulation, and colored lines are the inchworm results with respective
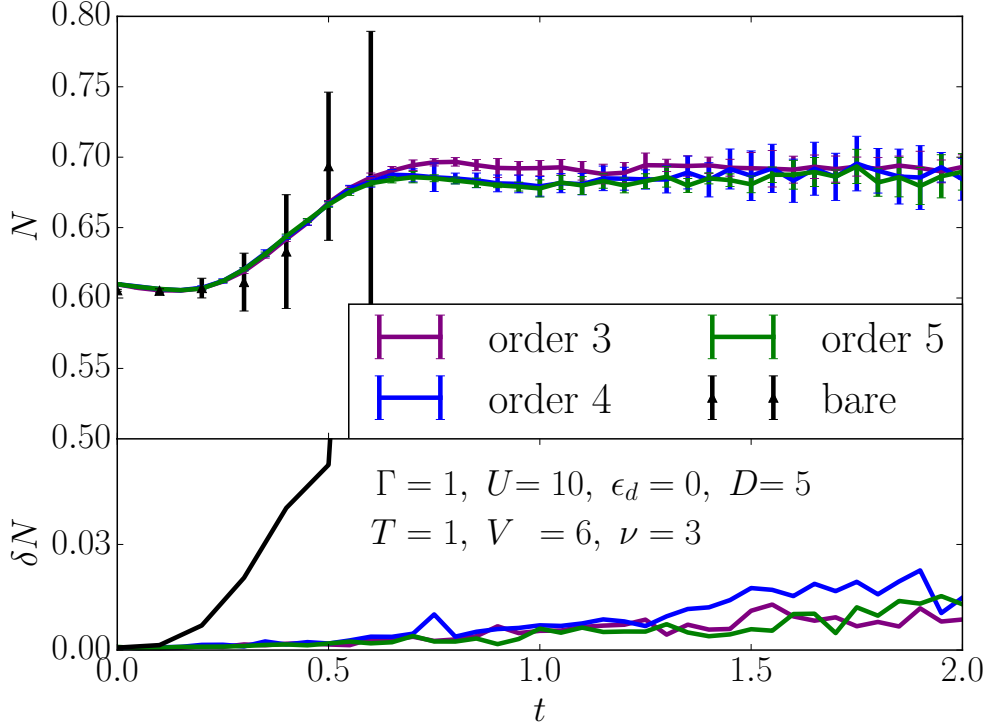
FIGURE 4.9: Top panel: Time evolution of the density on the impurity after a voltage quench with $\Gamma = 1$, $U = 10$, $\epsilon_d = 0$, $D = 5$, $T = 1$ and $V = 6$. Results obtained from a bare QMC calculation are shown for $t \leq 0.6$. The inchworm results with different orders agree with the bare result for $t \leq 0.6$ and coincide with each other for longer times. Bottom panel: Error estimates. Data obtained using the bare method shows an exponential increase of the errors as a function of time, whereas inchworm errors grow slower as a function of time.

maximum order constraints of order 3, 4, and 5 as labeled in the plot. At short times ($t \leq 0.6$ in these units), the inchworm results agree with the bare calculation within error bars, but for $t \gtrsim 0.3$ the bare QMC error bars are too large to be useful. Inchworm results for orders 4 and 5 coincide within error bars at long times, indicating that a solution obtained within a three-crossing approximation calculation would be accurate. The bottom panel of Fig. 4.9 shows statistical error bars for the data shown in the top panel. Errors for the bare calculation increase exponentially as a consequence of the dynamical sign problem. In contrast, the statistical inchworm error estimate grows slowly, allowing access to significantly longer times. We note that in order to account for error propagation and non-linear cross-correlations from short-time propagators

to long-time propagators within the inchworm algorithm, the error bars have been obtained by running multiple (in this case eight) complete independent calculations, each of which includes a different realization of the statistical noise at all times. The standard deviation between the different runs provides a useful estimate of the confidence interval, whereas the standard deviation within each run—which does not account for error propagation—grossly underestimates the error.

It is remarkable that no exponential growth of the errors is seen, signaling that the dynamical sign problem has been overcome. However, a gradual, approximately linear increase of errors with time is visible.

4.3.2 Currents

Fig. 4.10 shows results for the time dependence of a current passing through the impurity after a voltage quench from a thermalized equilibrium state. Parameters are $\Gamma = 1$, $U = 4$, $\epsilon_d = -2$, $D = 5$, $T = 1$ and $V = 4$. In the top panel, we observe that both NCA and OCA produce qualitatively wrong results for both the transient and long-time response. In contrast, inchworm results at orders 5–7 are in excellent agreement with each other, and order 4 is within about a percent from the converged result. Convergence at order 5 is well within reach of inchworm calculations but far beyond what could be realistically treated with semi-analytical methods. The bottom panel shows a rough estimate of the statistical error of the data shown in the top panel, obtained from the standard deviation of eight independent simulations of this problem. As observed for the densities, the inchworm error grows sub-exponentially in time and order constraint, indicating that the algorithm is able to overcome the dynamical sign problem.
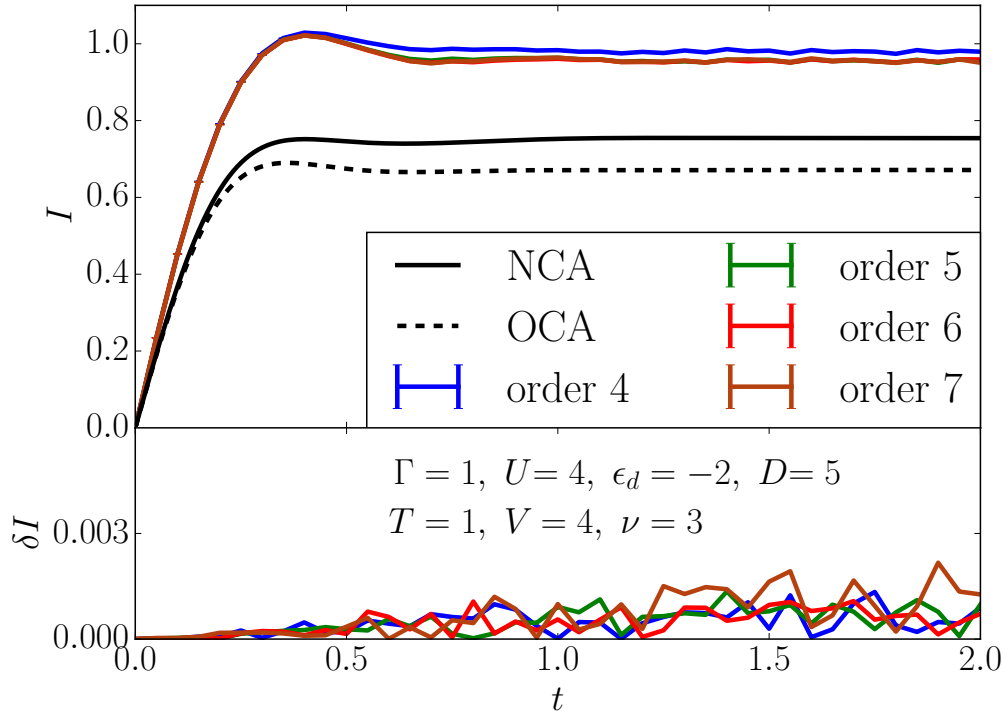
FIGURE 4.10: Top panel: The current dynamics after a voltage quench with $\Gamma = 1$, $U = 4$, $\epsilon_d = -2$, $D = 5$, $T = 1$ and $V = 4$. The inchworm results with different orders converge as max-order increases. Bottom panel: Error estimates of inchworm data obtained by averaging eight independent calculations. Errors increase as a function of time but avoid the exponential amplification seen in bare calculations.

4.3.3 Green's functions

Simulation of diagrams as shown in Fig. 4.6 enable both the simulation of currents and of two-time Green's functions. On the full Keldysh contour, a total of nine different types of Green's functions exist. One of them, the imaginary time Green's function, is shown in Fig. 4.11. The parameters used are $\Gamma = 1$, $U = 4$ and $\epsilon_d = -2$ (such that the system is at half filling), $D = 5$, $T = 1$, and $V = 0$.

As is visible in the upper panel, orders 4, 5, and 6 agree perfectly within error bars with the result obtained by a bare reference hybridization expansion calculation.

Statistical error bars, which do not estimate the systematic errors caused by the order truncation, are shown in the lower panel of Fig. 4.11. These errors are on
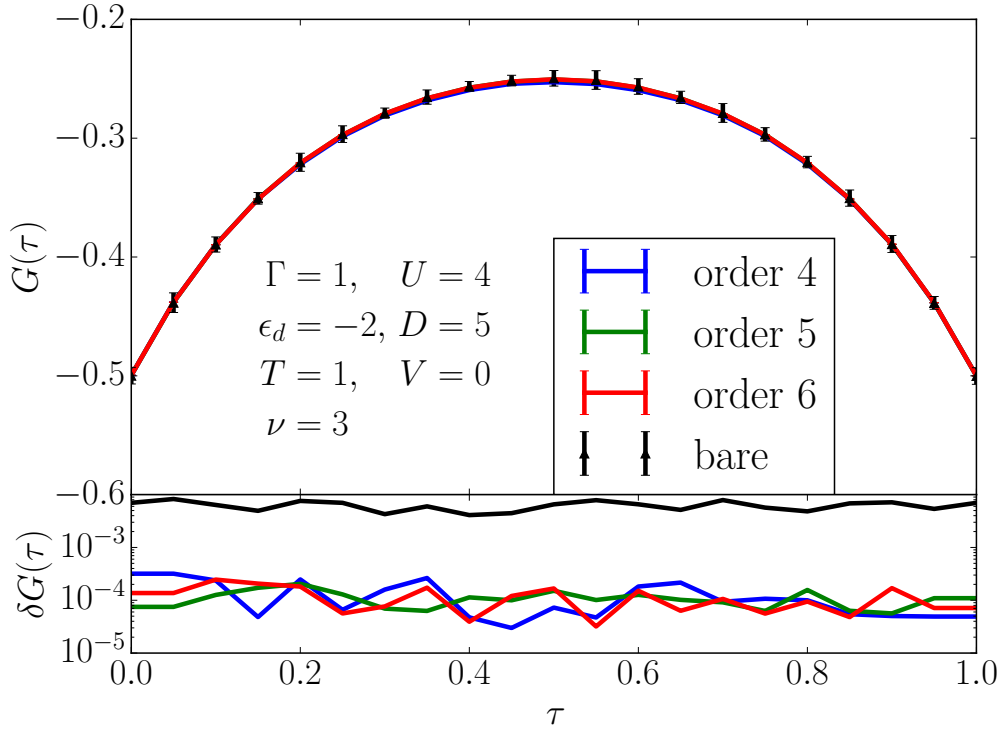
FIGURE 4.11: Top panel: The imaginary time Green's function in equilibrium (half-filling) with $\Gamma = 1$, $U = 4$, $\epsilon_d = -2$, $D = 5$, $T = 1$ and $V = 0$. Inchworm results with different orders all coincide and agree with the bare calculation. Bottom panel: The error estimate for the inchworms data is approximately constant in imaginary time.

the order of 10^{-4}.

The remaining components of the Green's function are similarly obtained by simulating the diagrams of Fig. 4.6.

4.3.4 Spectral functions

Knowledge of Green's functions and currents makes the calculation of interacting single-particle spectral functions possible. Ref. [72] introduced a method for computing steady state spectral functions $A(\omega)$ by obtaining steady state currents in two narrow auxiliary leads attached at frequency ω.
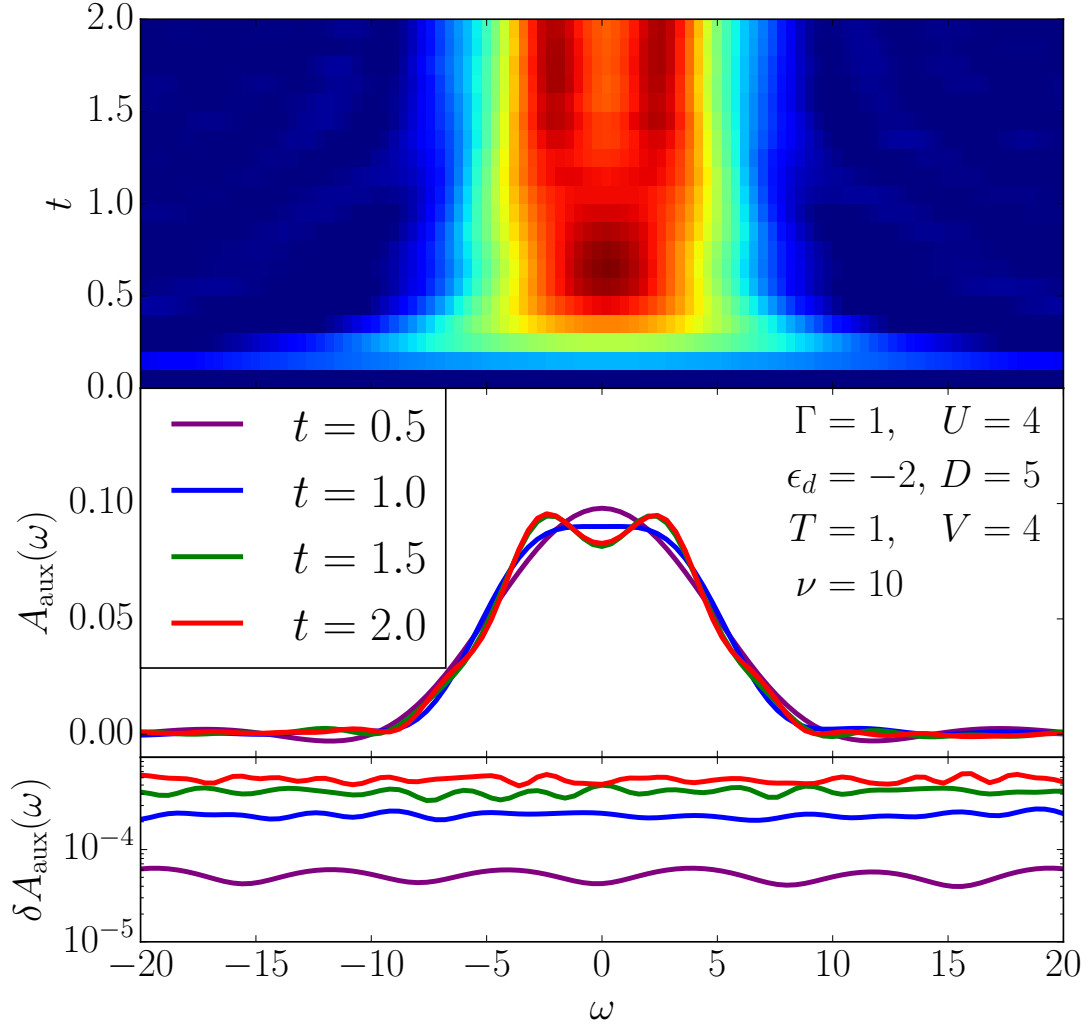
FIGURE 4.12: Top panel: A contour plot of the dynamics of auxilary current spectrum $A_{\mathrm{aux}}(\omega, t)$ after a voltage quench with $\Gamma = 1$, $U = 4$, $\epsilon_d = -2$, $D = 5$, $T = 1$ and $V = 4$. The maximum order cut-off for the inchworm calculation is 6. A formation and a splitting of the Kondo peak are observed as a function of time. Middle panel: Slices of auxiliary current spectrum at different times from the top contour plot. A clear splitting of the spectrum is shown. Bottom panel: Error estimate on the spectral function obtained from eight independent simulations.

Fig. 4.12 shows the result in the spirit of the auxiliary lead scheme, but generalized to the full Keldysh contour (see Appendix 5.3.3): initially, at $t = 0$, no current is flowing. As the voltage in the main leads, along with the auxiliary lead voltage, is instantaneously switched on, an auxiliary current starts flowing and relaxes on a time scale of about 1.5 to 2.

The upper panel shows the time-evolution of this current as a false-color contour plot. The vertical axis is time, the horizontal axis is frequency and the color represents the value of the auxiliary spectral function $A(\omega)$ obtained from the auxiliary currents. This quantity is equivalent to the physical spectral function in steady states. The middle panel shows frequency cuts through these data, illustrating a buildup of a more-or-less featureless spectral function at intermediate times ($t = 0.5, t = 1.0$), which splits into two sub-peaks (associated with the onset of Kondo physics [73, 110]) as time is extended towards time $t = 1.5$ and 2.0. By time $t = 1.5$, all features are converged.

In this parameter regime, both the final steady state spectral function, and the time-scale on which results converge are comparable after a quench from an equilibrium thermal state and after a quench from a decoupled initial state [72, 73], illustrating that in this case the presence of equilibrium correlations in the initial state did not substantially accelerate convergence.

The bottom panel shows the statistical errors of these data, obtained by computing the standard deviation of numerical data from several independent calculations. It is clearly visible that as t is increased, errors increase. However, the errors do not increase exponentially, again hinting that the dynamical sign problem has been overcome.

Fig. 4.13 shows the convergence of the data shown at the final time $t = 2.0$ in Fig. 4.12 as a function of the maximum diagram order sampled. It is evident that high orders $\gtrsim 5$ are needed to accurately capture the split peak, hinting that its correct description is related to strong dot–bath entanglement. It is also evident
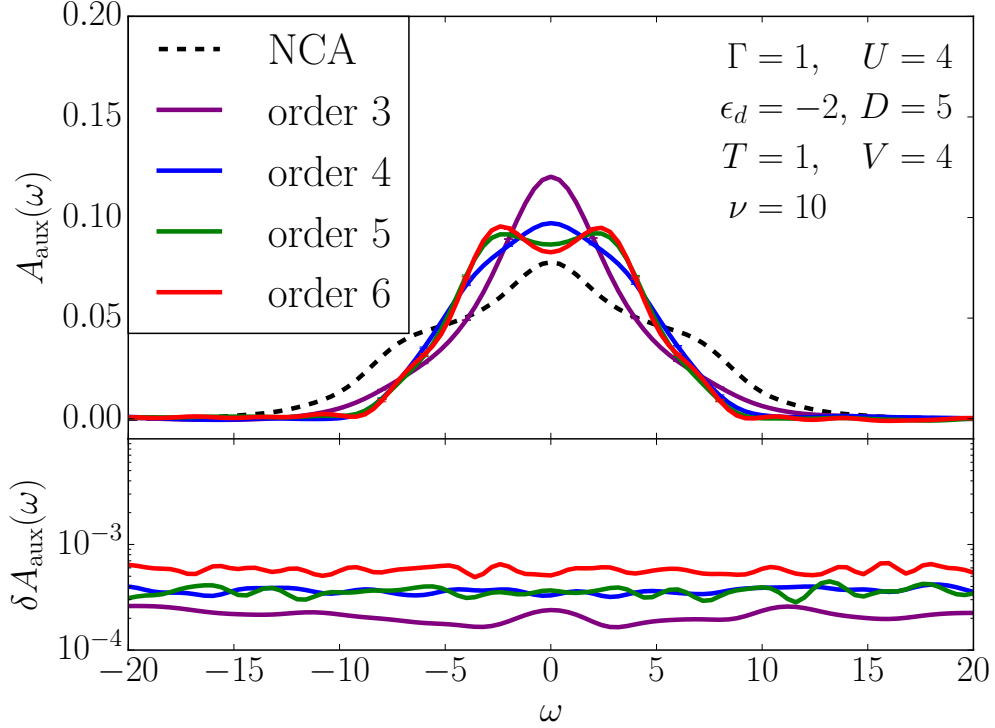
FIGURE 4.13: Top panel: The (half-filling) spectrum at $t = 2.0$ after a voltage quench with $\Gamma = 1$, $U = 4$, $\epsilon_d = -2$, $D = 5$, $T = 1$ and $V = 4$. The spectral function shows the establishment of a split Kondo peak as the diagram order is increased. The data for order 6 is identical to the data shown in Fig. 4.12. Bottom panel: Error estimate for data shown in main panel. The error remains constant as a function of frequency and increases as the maximum order is increased.

that deviations remain between orders 5 and 6, indicating that even higher orders may be necessary to fully capture the physics.

This is even more pronounced in the equilibrium case, Fig. 4.14, where contributions coming from long-lived correlations cause both an increase of the statistical errors (bottom panel) and a substantial difference order-by-order (main panel).

No additional complications arise away from half filling. Fig. 4.15 shows a sample steady state spectral function of a system obtained at time $t = 2.0$, away from particle-hole symmetry, after a voltage quench. The result is once again obtained with the auxiliary current setup, and is converged both in expansion order (orders 5 and 6 were needed) and time. While general features of the system are visible
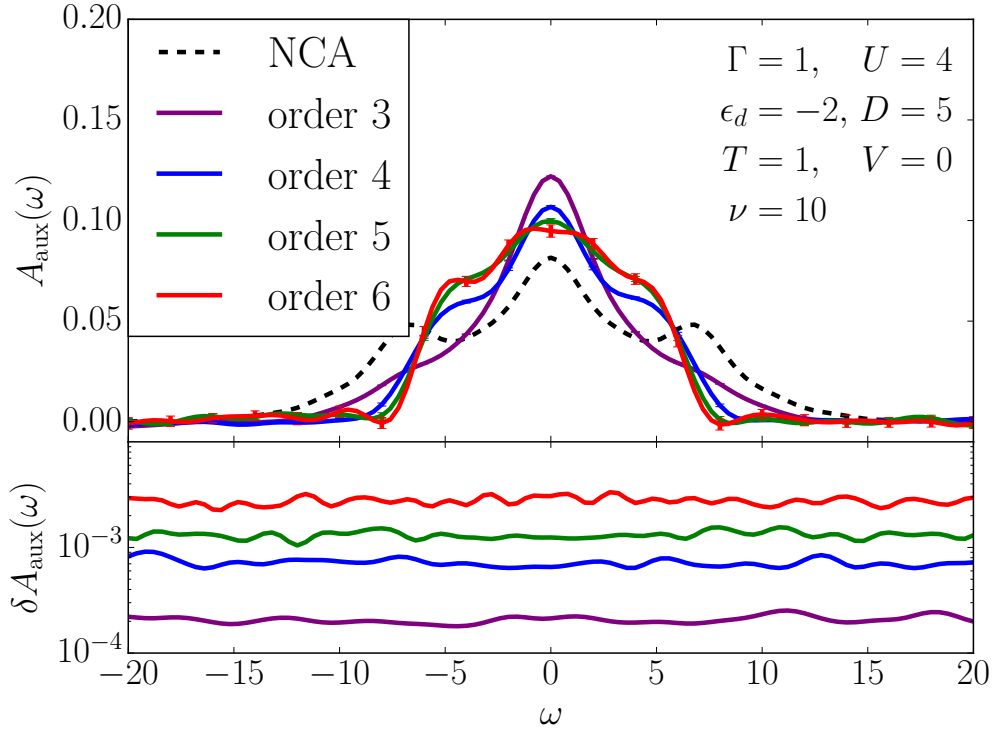
FIGURE 4.14: Top panel: The (half-filling) spectrum at $t = 2.0$ with no applied voltage with $\Gamma = 1$, $U = 4$, $\epsilon_d = -2$, $D = 5$, $T = 1$ and $V = 0$. Bottom panel: error estimate for data shown in the main panel.

even within a low-order NCA approximation, finer details such as the precise location of the peaks or their height and width clearly require analysis with more precise methods.

In conclusion, we have generalized the inchworm quantum Monte Carlo method to the full forward–backward–imaginary Keldysh contour. We have also introduced a scheme to measure currents, Green's functions, and spectral functions in inchworm QMC. Our formalism for measuring these quantities is directly applicable to inchworm calculations on the forward–backward Keldysh contour, but the addition of the imaginary contour allows us to begin the simulation from a correlated equilibrium initial condition. The method is numerically exact when all diagrams to all orders are considered. It is controlled if a sequence of results truncated to gradually increasing diagram orders is considered, and in particular
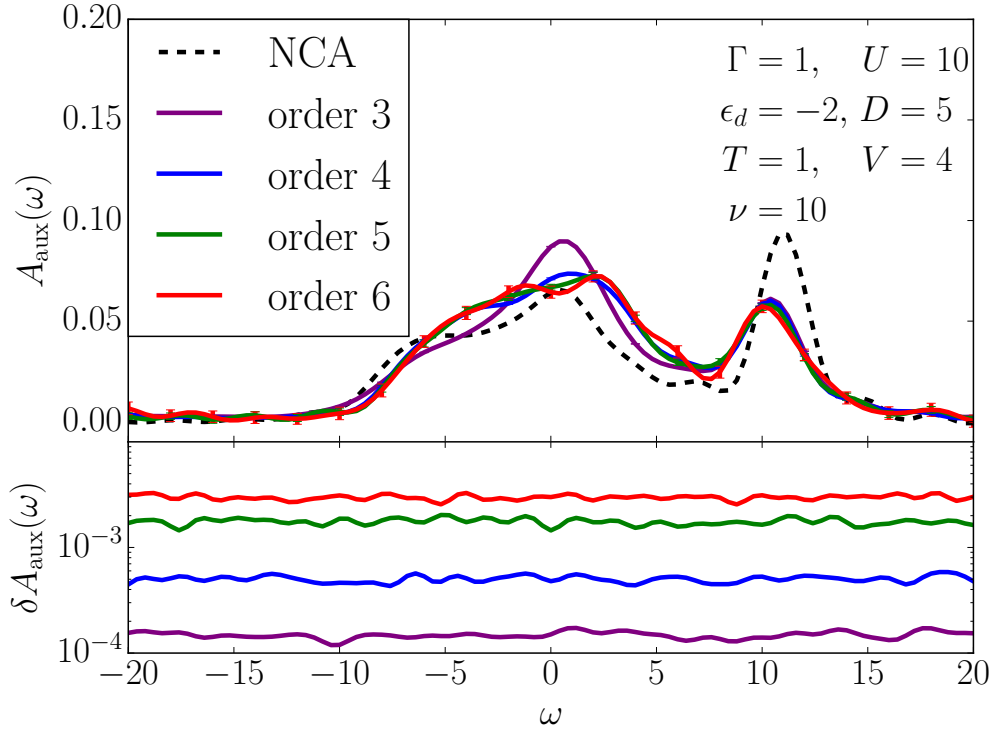
FIGURE 4.15: Top panel: Spectral function away from half filling at $t = 2.0$ after a voltage quench with $\Gamma = 1$, $U = 10$, $\epsilon_d = -2$, $D = 5$, $T = 1$ and $V = 4$. Bottom panel: error estimate for data shown in the main panel.

generates non-crossing diagrams when truncated to order one, one-crossing diagrams when truncated to order two, and two-crossing diagrams when truncated to order three. We showed that for the applications considered in this paper, diagrams of order five to seven were sufficient to achieve convergence.

The method makes the simulation of a wide range of problem setups possible: voltage and interaction quenches out of initially thermalized states, perturbations with explicit time-dependence, long-time steady-state setups, and equilibrium problems. It can in particular be used for obtaining spectral functions from the real time data, eliminating the need for the numerically ill-conditioned analytical continuation procedure of imaginary time data.

Inchworm Monte Carlo overcomes the dynamical sign problem in the sense that as t is increased, the effort for reaching longer times increases sub-exponentially. Unlike in the case of the forward–backward contour, we did not always observe

a plateau of the error as a function of time, indicating that the scaling is generally worse than quadratic in time. Several exponential barriers remain in the system: as temperature is lowered, higher orders proliferate and the number of diagrams needed to be considered increases quickly. Similarly, a larger impurity size exponentially increases the size of the local Hilbert space and thereby the cost of simulating the system.

The results shown here illustrate that it is now possible to reliably calculate currents, Green's functions, and spectral functions for equilibrium and nonequilibrium impurity problems with general time dependence, and imply that unbiased impurity solvers, which form a fundamental component for non-equilibrium dynamical mean field theory, are now available.

Chapter 5

Applications of Inchworm DMFT on the Hubbard Model in Equilibrium

In this chapter, we study the repulsive Hubbard Hamiltonian in equilibrium given in Eq. (1.1) by means of the Dynamical Mean Field Theory (DMFT) formulated on the L-shaped Keldysh contour introduced in Sec. 1.3. We employ the Inchworm quantum Monte Carlo solver described in Chapter 4 to obtain a numerically exact solution of the effective single impurity Anderson model. We demonstrate its power here for equilibrium for a testing purpose, because there are a large variety of well-developed methods available for comparison. We restrict ourselves to the case of a half-filled ($\mu = -U/2$) infinite coordination number Bethe lattice, characterized by a semi-elliptical bare density of states

$$D(\epsilon) = \frac{1}{2\pi v^2}\sqrt{4v^2 - \epsilon^2}, \qquad \epsilon < 2v \qquad (5.1)$$

as derived in Sec. 1.4. Throughout this chapter we assume $v_{ij} = v = 1$, and use the hopping amplitude as the unit of energy.

Time-translation invariance of the Hamiltonian in equilibrium implies that the two-time Green's function is only dependent on time differences

$$G(t, t') = G(t - t').$$ (5.2)

The DMFT self-consistency condition thus reads

$$\Delta(t - t') = G(t - t').$$ (5.3)

Here, we consider only the paramagnetic solution of the Hubbard model, as the temperatures being studied are higher than the Néel temperature [111].

In the following, we first briefly introduce the Mott metal-insulator transition and crossover in Sec. 5.1. In Sec. 5.2, we show the results of both real time Green's functions and spectral functions that resolve signatures of metal-insulator crossovers. We also demonstrate the convergence of the algorithms used in our calculations in Sec. 5.3.

5.1 Mott metal-insulator transition and crossover region

One of the most fascinating phenomena of strongly correlated electron systems is the interaction-induced metal-insulator transition. Such a transition is fundamentally different from filling-induced transitions between metals and band insulators since it cannot be understood in terms of effectively noninteracting electrons. This mechanism is not substantially different from the band theory picture, and the insulating state is viewed as a consequence of a band gap opening at the Fermi surface [112].

Fig. 5.1 (work from [5]) shows the phase diagram of the half-filled paramagnetic Hubbard model with semi-elliptic DOS in the Bethe lattice, obtained using DMFT methods with equilibrium QMC solver [5]. Since the Fermi liquid metal
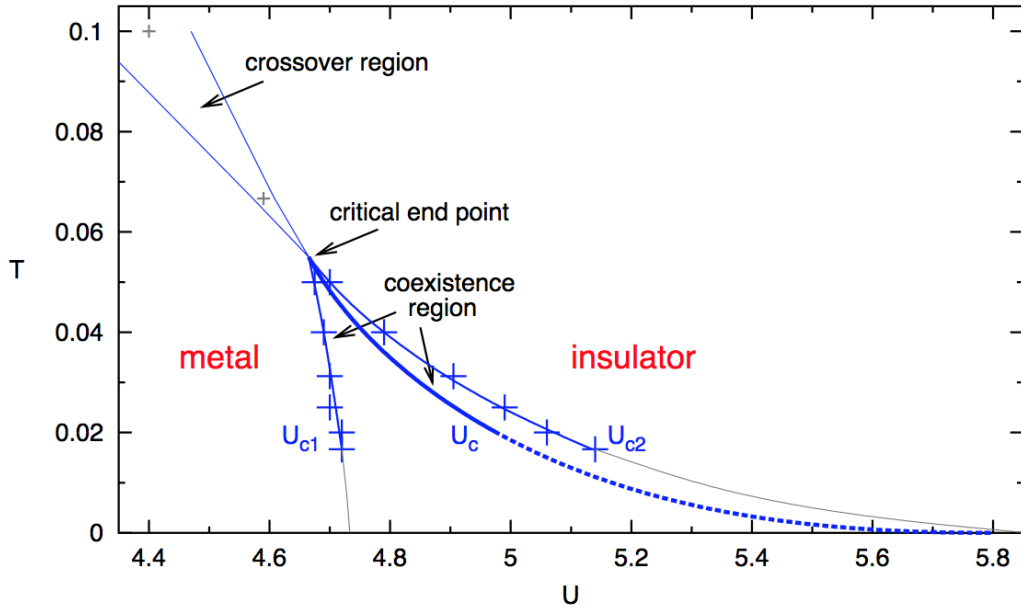
FIGURE 5.1: Mott metal-insulator transition phase diagram. Critical end point T_c, crossover region at higher temperature $T > T_c$, and coexistence region at lower $T < T_c$ between U_{c1}, U_{c2} are shown. The figure is a work from [5].

and the paramagnetic Mott insulator do not differ on symmetry grounds, these two phases can coexist in a finite range of parameter space. Indeed, there is such a metal-insulator coexistence region leading to a finite temperature first-order phase transition line [20, 113, 114], with U_{c1} and U_{c2} as the lower and upper edges of the coexistence region. Experimentally, an appreciable drop of resistivity is seen as the system is driven though such a finite temperature Mott transition, which separates the Mott insulating state and the metallic (Fermi liquid) state [23]. Similarly as in standard liquid-gas systems, the coexistence region, and the associated first-order line, terminate at the critical end-point at $T = T_c$. Therefore, at very low temperature $T < T_c$, this model features a first-order metal-insulator transition. For $T > T_c$, the phase transition vanishes, however, the evolution from metal to insulator as a function of U occurs as a smooth crossover. Interesting implications can be found in this region and a recent work [115] established that this intermediate metal-insulator crossover region shows all the features expected in a quantum critical regime, including the
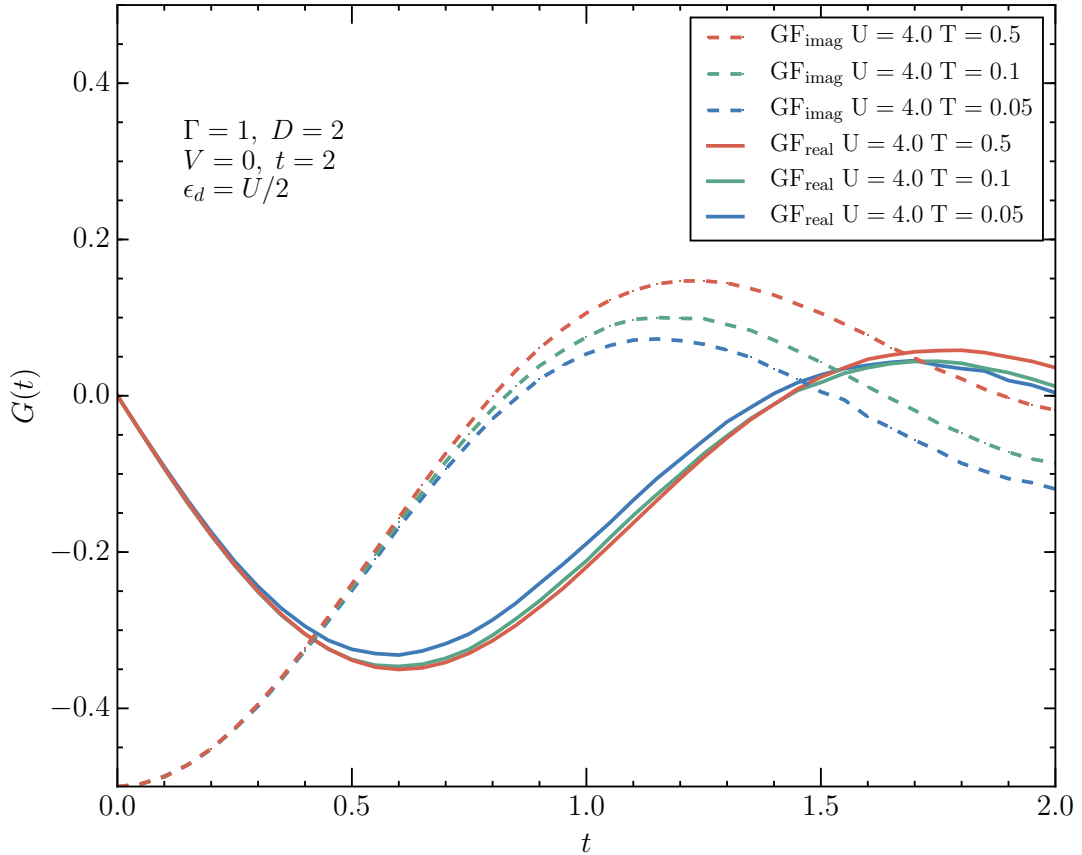
FIGURE 5.2: The real and imaginary parts of the converged real time DMFT Green's function $G(t)$, where $t \in [0, t_{\max}]$ with $t_{\max} = 2$, with $\Gamma = 1$, $U = 4$, $\epsilon_d = -2$, $D = 2$ and $V = 0$ at temperatures $T = 0.5$, $T = 0.1$ and $T = 0.05$.

characteristic scaling behavior for the family of resistivity curves. In the following section, we focus on the crossover region and show the explicit gap opening in the density of states, obtained from the real-time solver.

5.2 Results

5.2.1 Real-time Green's functions

Fig. 5.2 shows the converged Green's functions $G(t)$ with $\Gamma = 1$, $U = 4$, $\epsilon_d = -2$, $D = 2$ and $V = 0$ at temperatures $T = 0.5$, $T = 0.1$ and $T = 0.05$. Later in Fig. 5.4, we can see that the change at long times in the imaginary parts of
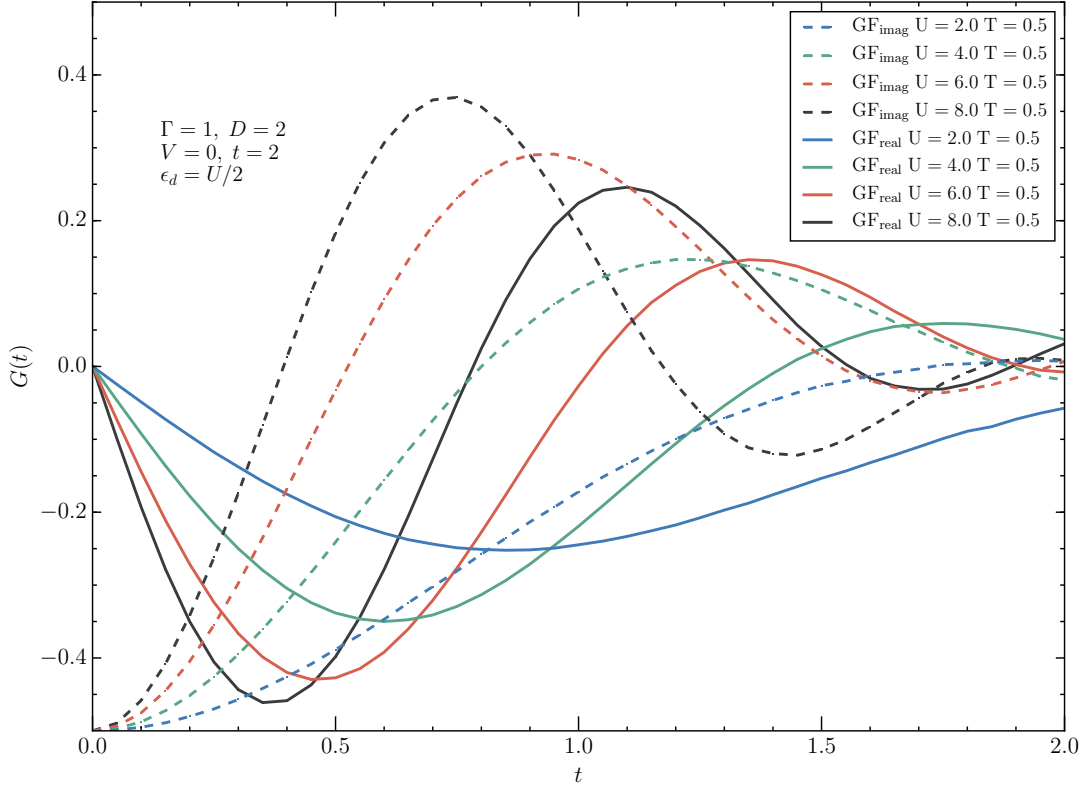
FIGURE 5.3: The real and imaginary parts of the converged real time DMFT Green's function $G(t)$, where $t \in [0, t_{\max}]$ with $t_{\max} = 2$, with $\Gamma = 1$, $D = 2$, $T = 0.5$ and $V = 0$ at on-site interaction strengths $U = 2$, $U = 4$, $U = 6$ and $U = 8$.

$G(t)$ corresponds to the formation of a quasi-particle peak as the temperature is lowered.

Fig. 5.3 shows the converged Green's functions $G(t)$ with $\Gamma = 1$, $D = 2$, $T = 0.5$ and $V = 0$ at on-site interaction strengths $U = 2$, $U = 4$, $U = 6$ and $U = 8$. Later in Fig. 5.5, we can see that the change in the amplitude and the damping rate of real time Green's functions corresponds to the opening of the gap in the density of states in the metal-insulator crossover region, as the on-site interaction strength increases.

5.2.2 Spectral functions

Fig. 5.4 shows the converged spectral functions $A(\omega)$ with $\Gamma = 1$, $U = 4$, $\epsilon_d = -2$, $D = 2$ and $V = 0$ at temperatures $T = 0.5$, $T = 0.1$ and $T = 0.05$. The spectral
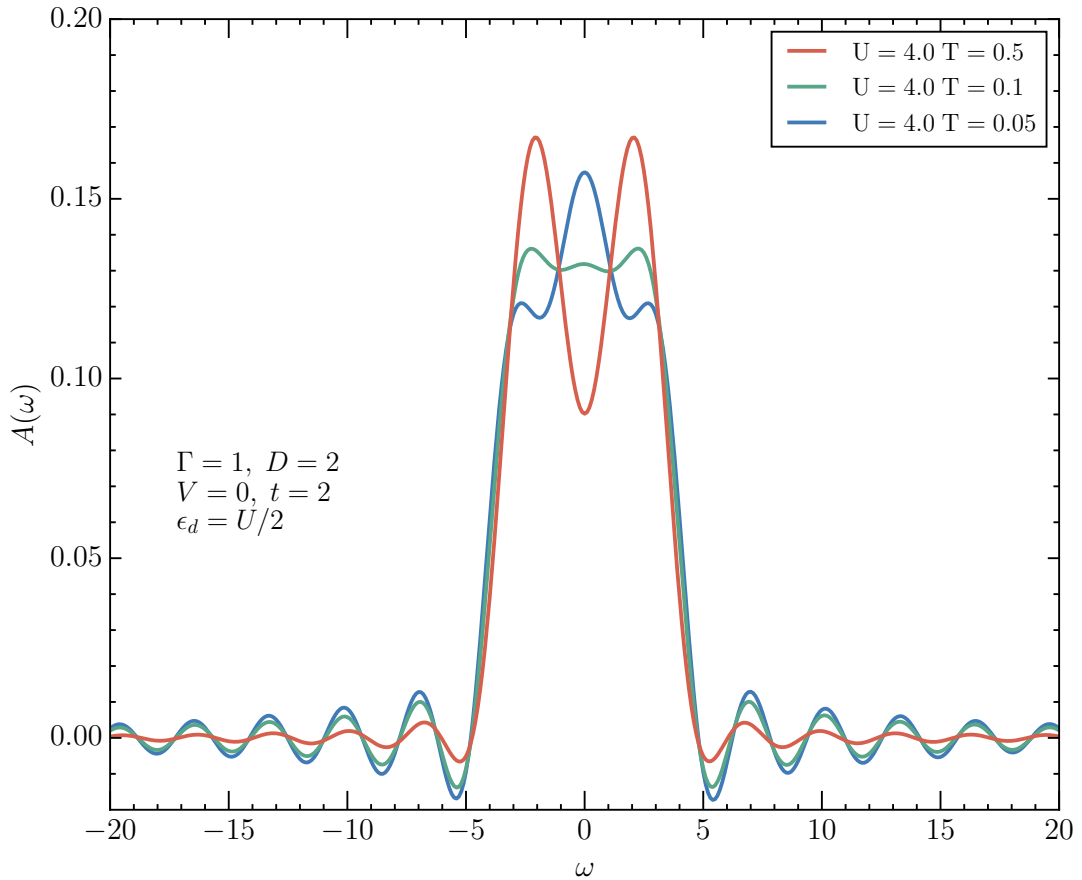
FIGURE 5.4: The converged DMFT spectral function $A(\omega)$ obtained by directly performing the Fourier transform on the real time Green's function with a cutoff at $t_{\max} = 2$, with $\Gamma = 1$, $U = 4$, $\epsilon_d = -2$, $D = 2$ and $V = 0$ at temperatures $T = 0.5$, $T = 0.1$ and $T = 0.05$. This figure indicates the formation of the quasi-particle peak as the temperature is lowered. The oscillation on both sides of the tails is an artificial effect due to the finite time cutoff of the Fourier transform, and will disappear as the simulation time $t_{\max}$ is extended.

functions are obtained by direct Fourier transforms (Sec. 3.3.4) of the real time Green's functions $G(t)$ as plotted in Fig. 5.2, where $t \in [0, t_{\max}]$ with $t_{\max} = 2$. The figure illustrates the formation of the quasi-particle peak as the temperature is lowered.

Fig. 5.5 shows the converged spectral functions $A(\omega)$ with $\Gamma = 1$, $D = 2$, $T = 0.5$ and $V = 0$ at on-site interaction strengths $U = 2$, $U = 4$, $U = 6$ and $U = 8$. The spectral functions are obtained by direct Fourier transforms (Sec. 3.3.4) of the real time Green's functions $G(t)$ as plotted in Fig. 5.3, where $t \in [0, t_{\max}]$ with $t_{\max} = 2$. As the on-site interaction strength increases, a gap opening in
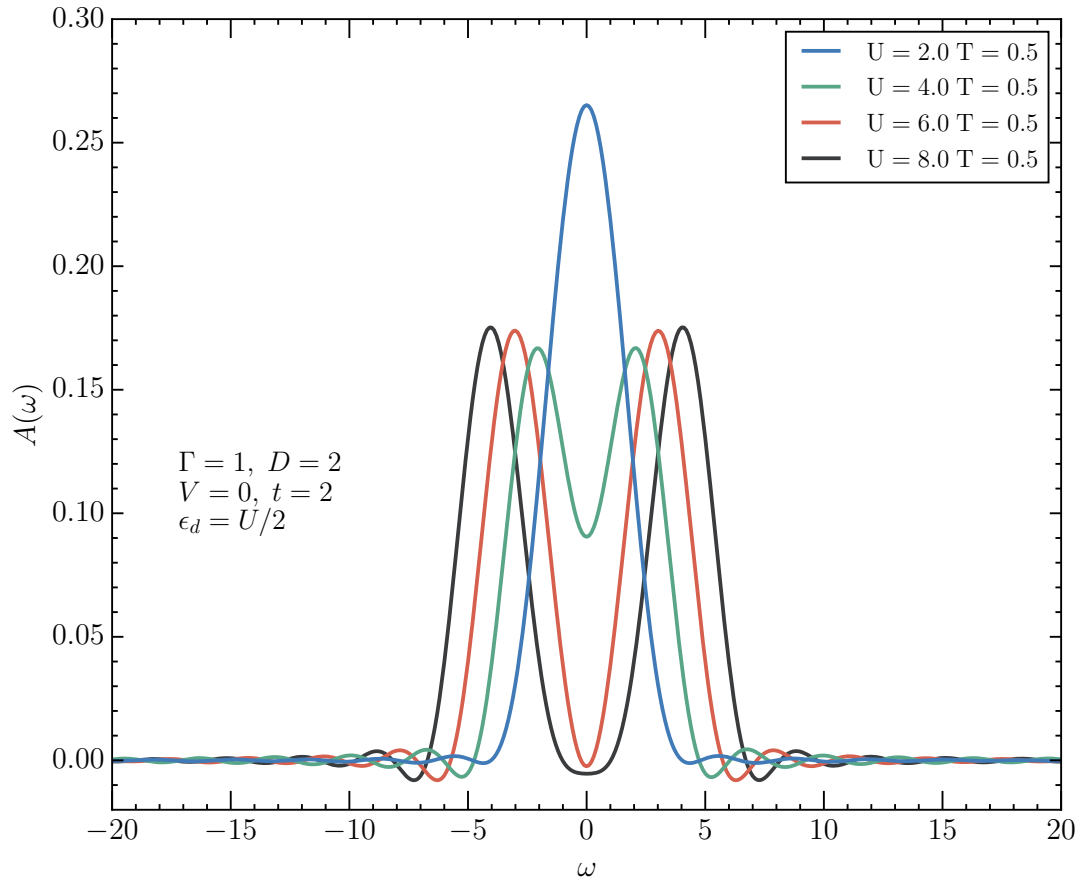
FIGURE 5.5: The converged DMFT spectral function $A(\omega)$ obtained by directly performing the Fourier transform on the real time Green's function with a cutoff at $t_{\max} = 2$ with $\Gamma = 1$, $D = 2$, $T = 0.5$ and $V = 0$ at on-site interaction strengths $U = 2$, $U = 4$, $U = 6$ and $U = 8$. This figure demonstrates the metal-insulator crossover as the on-site interaction strength increases. The oscillation on both sides of the tails is an artificial effect due to the finite time cutoff of the Fourier transform at $t_{\max}$, and disappears as the simulation time $t_{\max}$ is extended.

the density of states is seen indicating the metal-insulator crossover. Thus the metal-to-insulator crossover observed in real time indeed corresponds to metallic and insulating behavior in the spectral function.
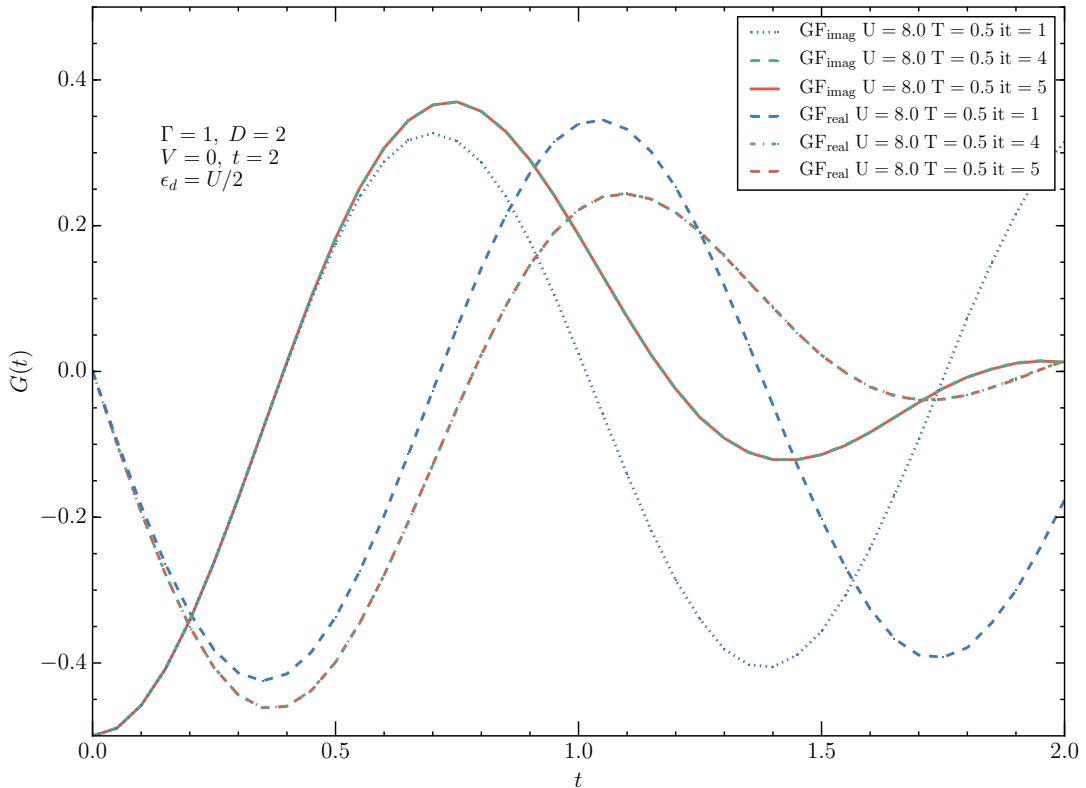
FIGURE 5.6: The real and imaginary parts of the DMFT Green's function $G(t)$ as a function of real time t, where $t \in [0, t_{\max}]$ with $t_{\max} = 2$. Parameters are $\Gamma = 1$, $U = 8$, $\epsilon_d = -4$, $D = 2$, $T = 0.5$ and $V = 0$. Shown are DMFT iterations $1, 4$ and 5. Iterations 4 and 5 are indistinguishable within our noise, which indicates the DMFT self-consistent loop is converged.

5.3   Convergence of the algorithms

5.3.1   DMFT self-consistency loop

Starting with the semi-elliptic density of states and far away from phase transitions, the non-equilibrium DMFT self-consistent loop converges quickly and a solution is achieved within about 2–5 iterations at high temperatures. Fig. 5.6 and Fig. 5.7 show the Green's function $G(t)$ and the spectral function $A(\omega)$ at various iterations with parameters $\Gamma = 1$, $U = 8$, $\epsilon_d = -4$, $D = 2$, $T = 0.5$ and $V = 0$. The spectral function is obtained by a direct Fourier transform of the real time Green's function $G(t)$, where $t \in [0, t_{\max}]$ with $t_{\max} = 2$ as in Fig. 5.6.
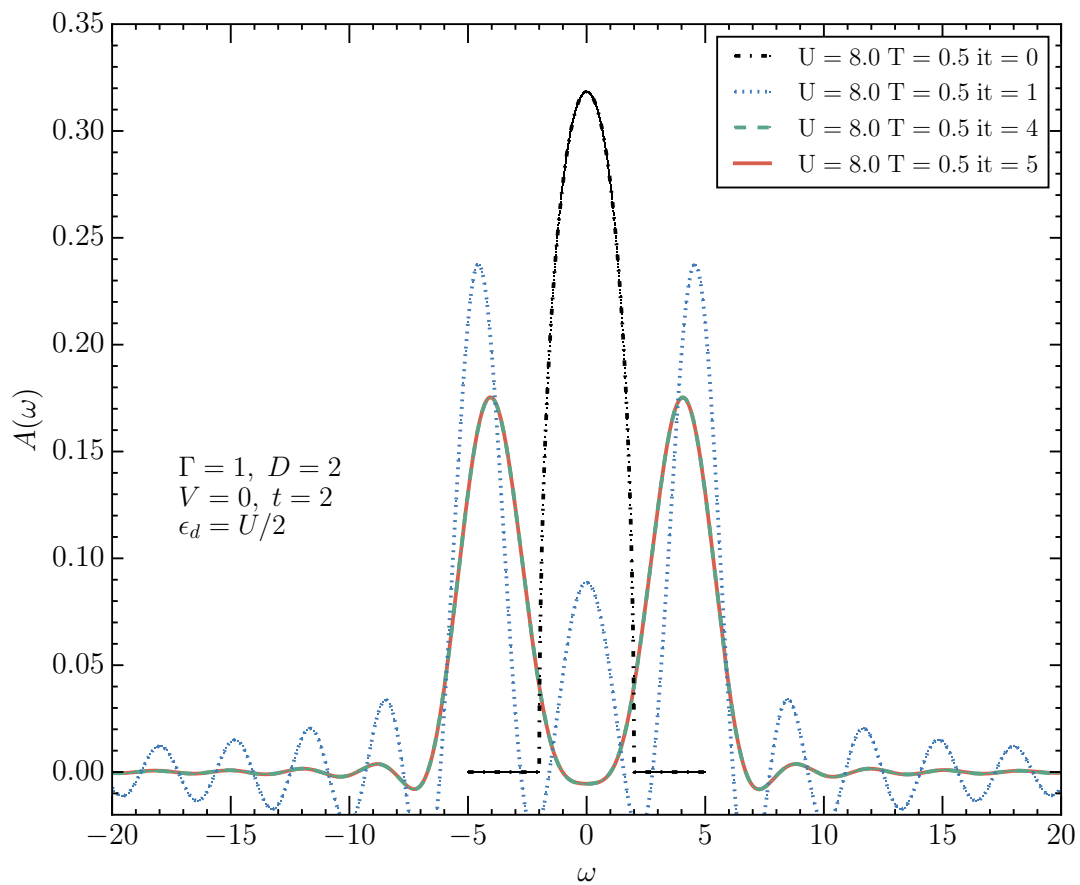
FIGURE 5.7: The convergence of the DMFT spectral function $A(\omega)$ by directly performing the Fourier transform on the real time Green's function with a cutoff at $t_{\max} = 2$, with $\Gamma = 1$, $U = 8$, $\epsilon_d = -4$, $D = 2$, $T = 0.5$ and $V = 0$ at DMFT iterations $0, 1, 4$ and 5. The results from iteration 4 and iteration 5 exactly agree with each other, which indicates the DMFT self-consistent loop is converged. The oscillation on both sides of the tails is an artificial effect due to the finite time cutoff of the Fourier transform, and will disappear as the simulation time $t_{\max}$ is extended.

Both parts from iteration 4 and iteration 5 exactly agree with each other, which indicates the DMFT self-consistent loop is converged.

5.3.2   Inchworm order

Fig. 5.8 shows the comparison of the Matsubara Green's function $G(\tau)$ computed by the inchworm nonequilibrium QMC solver and an equilibrium continuous time hybridization expansion (CT-HYB) solver (TRIQS/CTHYB) [6, 7]. They come from a single-shot impurity calculation starting with the semielliptic density of

116
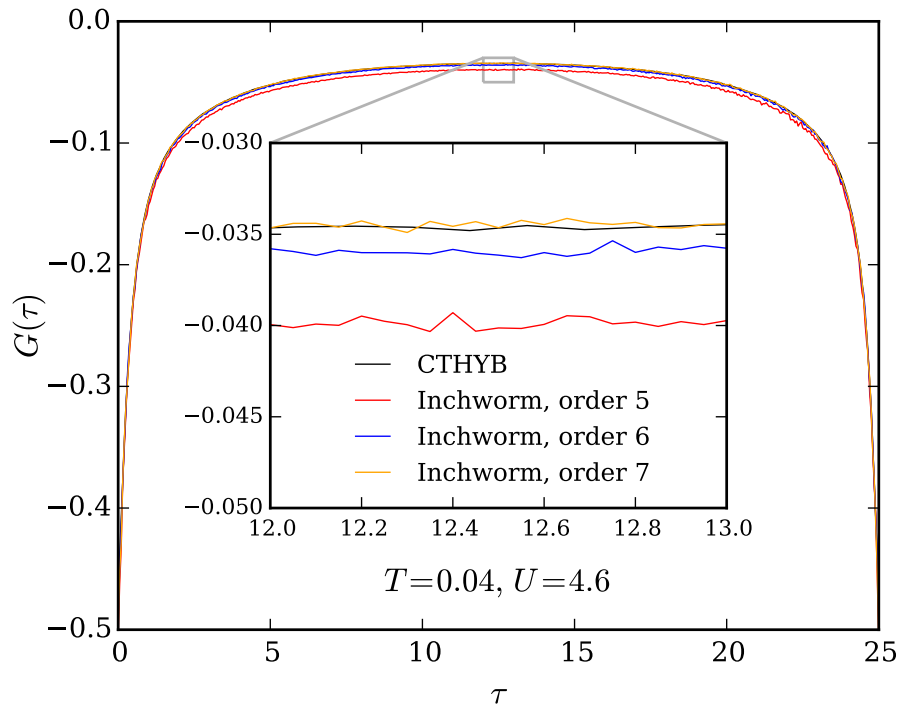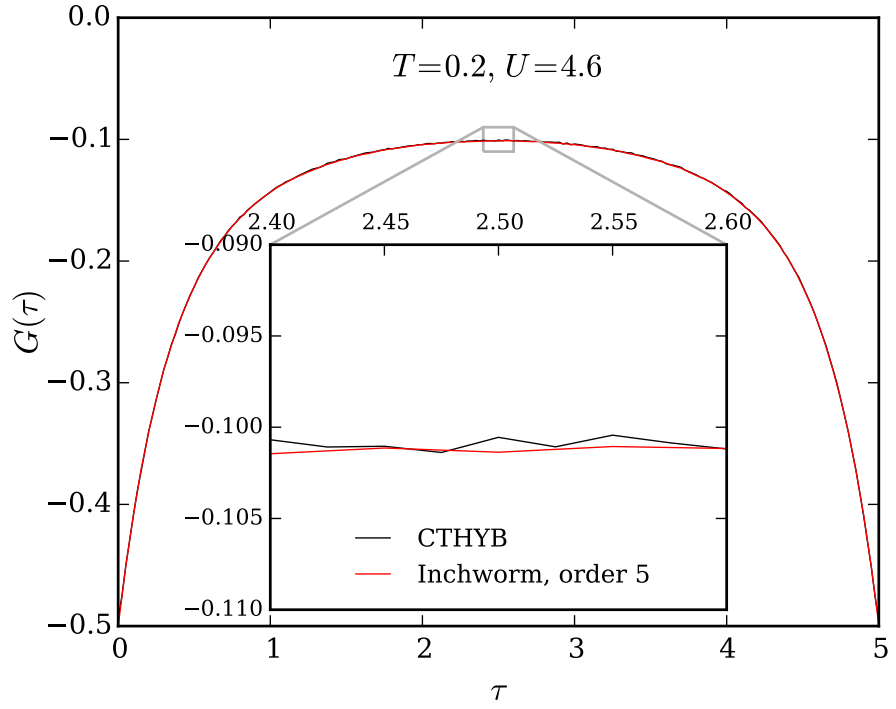
FIGURE 5.8: Matsubara Green's function $G(\tau)$ computed for the impurity model in equilibrium with $\Gamma = 1$, $U = 4.6$, $\epsilon_d = -2.3$ (half-filling), $D = 2$, $V = 0$ at two temperatures and with different inchworm order truncations. Results from an equilibrium hybridization expansion solver (TRIQS/CTHYB [6, 7]) are given as a reference.
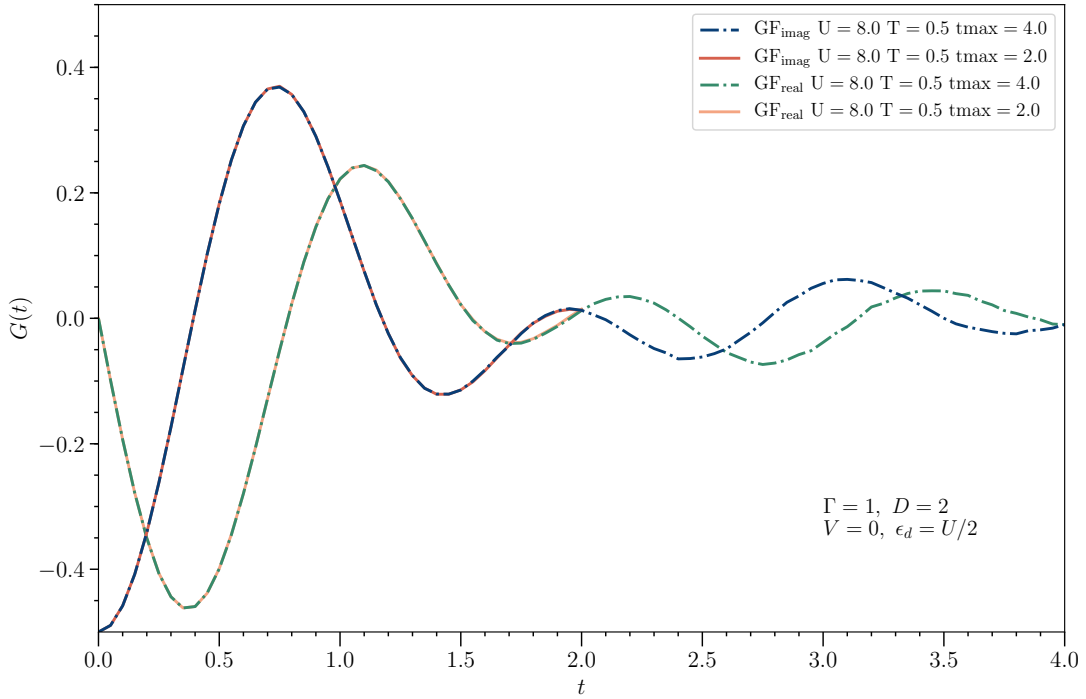
FIGURE 5.9: The converged real and imaginary parts of the DMFT Green's function $G(t)$ as a function of real time t, where $t \in [0, t_{\max}]$ with $t_{\max} = 2$ and $t_{\max} = 4$. Parameters are $\Gamma = 1$, $U = 8$, $\epsilon_d = -4$, $D = 2$, $T = 0.5$ and $V = 0$. Within interval $t \in [0, 2]$, the results are consistent.

states at $\Gamma = 1$, $U = 4.6$, $\epsilon_d = -2.3$ (half-filling), $D = 2$, and $V = 0$. The top panel of Fig. 5.8 demonstrates that at high temperature $T = 0.2$, a maximum-order 5 in the inchworm order truncation is sufficient. Nevertheless, the bottom panel of Fig. 5.8 shows that as the temperature is lowered to $T = 0.04$, an convergence of the inchworm calculations with order truncations set to $5, 6$ and 7 to the equilibrium result is observed. This indicates that a higher order of crossings is indeed essential for obtaining the correct results as the temperature is decreased.

5.3.3 Fourier transform

As mentioned before, the spectral functions shown in this chapter are obtained by direct Fourier transforms of the real-time Green's function data. The cutoff $t_{\max}$ in the Fourier integrals generates noises in spectral functions, for example, the oscillations around zero at the tails, which is called the Nyquist limit in
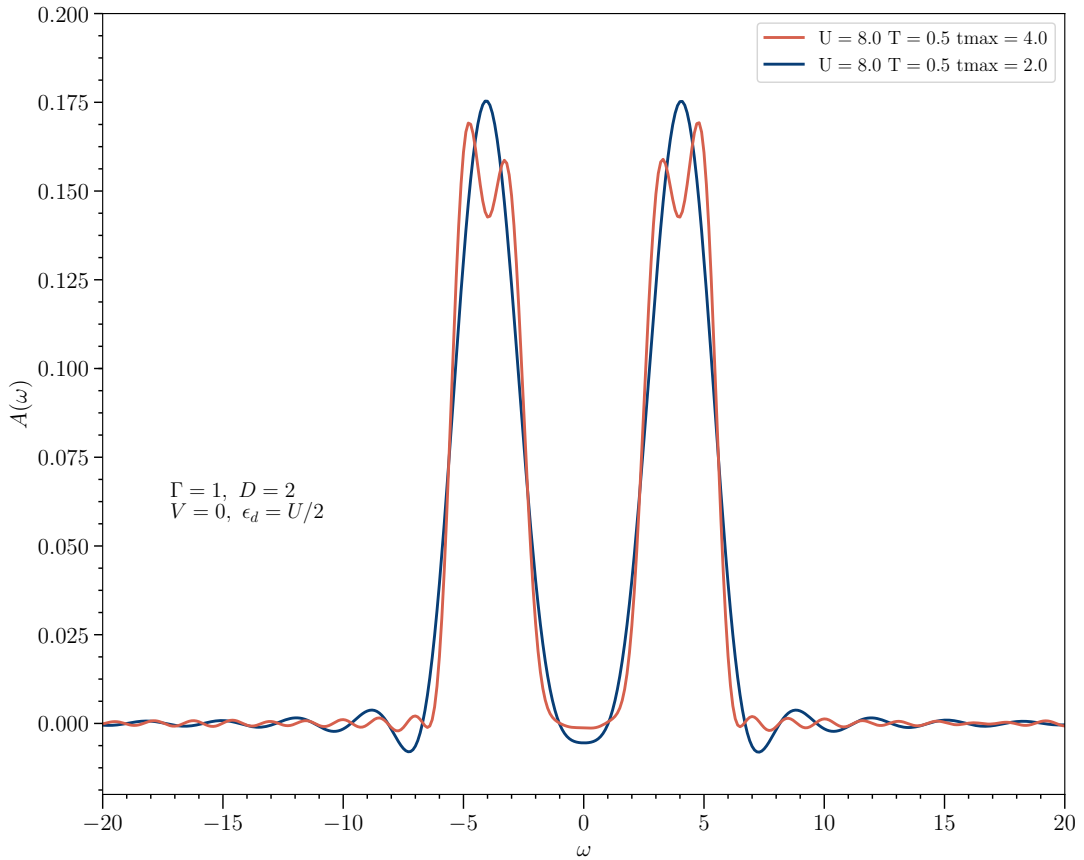
FIGURE 5.10: The converged DMFT spectral function $A(\omega)$ by directly performing the Fourier transform on the real time Green's function with a cutoff at $t_{\max} = 2$ (blue) and $t_{\max} = 4$ (red), with $\Gamma = 1$, $U = 8$, $\epsilon_d = -4$, $D = 2$, $T = 0.5$ and $V = 0$. The oscillations on both sides of the density of states become smaller because the data is extended to $t = 4$ and the resolution is improved so that the fine structures are now seen in the red curve.

the area of discrete signal processing [116]. If a simulation with a longer time limit $t_{\max} = 4$ on the Keldysh contour is executed, as shown in Fig. 5.9, the spectral functions obtained will have reduced oscillations. In addition, because the Nyquist frequency of the longer-time simulation is higher, the resolution of the results becomes better and the fine structures in the density of states can be observed in Fig. 5.10.

In conclusion, we tested our nonequilibrium DMFT methods with the inchworm impurity solvers on the Hubbard model on a infinite dimensional Bethe lattice and demonstrated its power here for equilibrium, where a large variety of well-developed methods are available for comparison. We showed results for real-time

Green's functions and spectral functions independent of analytical continuation techniques. We observed the formation of a quasi-particle peak as the temperature is lowered and the signature of an interaction-driven metal-insulator crossover. In principle, the method can cover the full parameter range of the system. However, so far these calculations have been limited to high temperatures by computation powers. The phase transition is particularly of higher computational time complexity. The reason is twofold: (1) Near the phase transition, the DMFT self-consistency loop requires more iterations to converge; (2) As seen in Sec. 5.3.2, higher orders are necessary as the temperature is lowered. More computation times should be devoted to cross these barriers and explore the full phase diagram, and we will pursue this direction in the future.

Summary

Recent progress on the experimental side of non-equilibrium quantum many-particle physics has stimulated extensive numerical investigation of non-equilibrium phenomena in strongly correlated electron systems, to the point that it is now one of the most active and exciting branches of modern condensed matter physics. Thesse studies provide rich new insights that could not be obtained from the study of equilibrium systems, such as dynamical phase transitions [25], thermalization behavior [117], excitations and relaxations [118] of quantum many-body systems. In this thesis, we study two minimal models that are generally assumed to capture most of the relevant physics in this context – the Hubbard model and the Anderson impurity model.

The Hubbard model is the simplest fermionic lattice model that is believed to contain the the main ingredients to describe strongly interacting electrons in certain types of solids, such as cuprates and organics. The Anderson impurity model is one of the simplest fermionic quantum impurity models. It mimics the behavior of impurities embedded in a host material [16] and also appears as an auxiliary model in the formulation of dynamical mean field theory (DMFT) [20]. In this thesis, we have presented the non-equilibrium formalism of DMFT, which approximates lattice models, for example, the Hubbard model, by impurity models, in this case, the Anderson impurity model, supplied with a self-consistency condition. We have derived the self-consistency condition in the case of a $Z \to \infty$ Bethe lattice, in which DMFT becomes exact.

In this project, we have constructed the non-equilibrium framework of quantum many-body systems, which leads to calculations using the Keldysh formalism. We

have performed explicitly the perturbation theory in case of strong coupling and we introduced semi-analytical approximations for the Anderson impurity model. We have explained the idea of the continuous time Quantum Monte Carlo (CT-QMC) methods and presented a detailed description of this numerical algorithm we developed that is suitable for strong-coupling regimes – the continuous time hybridizaiton expansion (CT-HYB). We have outlined the techniques we took for measurements and showed numerically exact results of the impurity model after a quantum quench from equilibrium. We have presented the behavior of time-dependent currents that are beyond linear response and observed the full dynamics of the system, from equilibrium to steady state, exhibit Kondo behavior at all times.

We have seen that the main problem with the approach lies in the time domain. The bare impurity solvers with non-equilibrium Monte-Carlo fail because the sign problem makes low temperatures and simulating real-time dynamics for long times exponentially hard. To overcome this difficulty, we have adapted a new idea of "Inchworm Algorithm", based on iteratively reusing the information obtained in previous steps to extend the propagation to longer times. The algorithm largely reduces the required order at each simulation and re-scales the exponential challenge to quadratic. We have also introduced a method to compute Greens functions, spectral functions, and currents for inchworm Monte Carlo. In the results part, we have shown that the inchworm solver produced results that are identical to the bare QMC at short times and are able to extend the simulation to longer time propagations with controlled errors.

In this way, the inchworm solver vastly outperforms previous algorithms and overcomes the dynamical sign problem. Its result can be used in the non-equilibrium DMFT loop to produce reasonable outcomes. Within this project, we have tested our algorithms along with the nonequilibrium DMFT formulation to study the one-band Hubbard model in equilibrium on a Bethe lattice. We have seen the results of both real-time Green's functions and spectral functions, which are isolated from analytical continuation techniques, and have resolved signatures

of interaction-driven metal-insulator crossovers. We also demonstrated the fine structures of the Hubbard band when longer-time propagation is simulated.

In conclusion, the results shown in this thesis illustrate that it is now possible to calculate reliable currents, Green's fucntions, and spectral functions for equilibrium and nonequilibrium impurity problems with general time dependence. And we are able to make use of this impurity solver as the key part of the DMFT method to study lattice models, like the Hubbard model. These algorithms dramatically increases the current ability of the theoretical framework to reproduce and understand non-equilibrium electron correlation phenomena. With the main applications listed in Ref. [8], it is now conceivable to predict new behaviors of strongly correlated lattice systems, and this is where this project will progress in the future.

Appendix

Spectral function from auxiliary leads

A convenient method for extracting the spectral functions $A(\omega)$ from non-equilibrium Green's functions $G(t, t')$ comes from considering the current through two auxiliary leads which are weakly coupled to the system only at a predefined frequency ω' [$\Gamma(\omega) = \eta\delta(\omega - \omega')$], where one lead is taken to be full and one to be empty [73]. Using

$$\Delta_\sigma(t, t') = \sum_k \mathcal{V}_k^2 \langle \mathcal{T}_\mathcal{C} c_{\alpha k\sigma}(t) c_{\alpha k\sigma}^\dagger(t') \rangle \tag{4}$$

$$= -i \int d\omega e^{-i\omega(t-t')} \Gamma(\omega) [\theta_\mathcal{C}(t, t') \pm f_\alpha(\omega)] \tag{5}$$

we have the hybridization functions

$$\Delta_{\text{aux}}(t, t') = -i\eta e^{-i\omega'(t-t')} [\theta_\mathcal{C}(t, t') - f_i] \tag{6}$$

where

$$f_i = \begin{cases} 0 : i = 0 \text{ (empty)} \\ 1 : i = 1 \text{ (full)} \end{cases} \tag{7}$$

and η is small. Using equation

$$\langle I_\alpha(t) \rangle = 2\Re \left(\sum_\sigma \int_\mathcal{C} dt' G_\sigma(t', t) \times \Delta_{\alpha\sigma}(t, t') \right) \tag{8}$$

124

to calculate the currents $I_A^{\mathrm{e}}(\omega, t)$, $I_A^{\mathrm{f}}(\omega, t)$ through the empty and full auxiliary leads, we define the object

$$A_{\mathrm{aux}}(\omega, t) = \lim_{\eta \to 0} -\frac{2h}{e\pi\eta} \left[I_A^{\mathrm{f}}(\omega, t) - I_A^{\mathrm{e}}(\omega, t) \right] \tag{9}$$

which reproduces the spectral function $A(\omega, t)$ in steady state [72, 73]. Here, we perform this process as a post processing step on our non-equilibrium Green's functions so that the auxiliary leads are not included in our simulations. In our experience this way of obtaining the spectral information provides results that are more stable than an explicit Fourier transform of the time-dependent Green's function.

Bibliography

[1] Antoine Georges and Gabriel Kotliar. Hubbard model in infinite dimensions. *Phys. Rev. B*, 45:6479–6483, Mar 1992. doi: 10.1103/PhysRevB.45. 6479. URL https://link.aps.org/doi/10.1103/PhysRevB.45.6479.

[2] Neven Barii, Mun K. Chan, Yuan Li, Guichuan Yu, Xudong Zhao, Martin Dressel, Ana Smontara, and Martin Greven. Universal sheet resistance and revised phase diagram of the cuprate high-temperature superconductors. *Proceedings of the National Academy of Sciences*, 110(30):12235–12240, 2013. doi: 10.1073/pnas.1301989110. URL http://www.pnas.org/content/110/30/12235.abstract.

[3] Gabriel Kotliar and Dieter Vollhardt. Strongly correlated materials: Insights from dynamical mean-field theory. *Physics Today*, 57:53, March 2004. doi: http://dx.doi.org/10.1063/1.1712502. URL http://physicstoday.scitation.org/doi/10.1063/1.1712502.

[4] Martin Eckstein, Marcus Kollar, Krzysztof Byczuk, and Dieter Vollhardt. Hopping on the bethe lattice: Exact results for densities of states and dynamical mean-field theory. *Phys. Rev. B*, 71:235119, Jun 2005. doi: 10.1103/PhysRevB.71.235119. URL https://link.aps.org/doi/10.1103/PhysRevB.71.235119.

[5] Nils Blümer. Mott-hubbard metal-insulator transition and optical conductivity in high dimensions. *Thesis*, 1999.

[6] Olivier Parcollet, Michel Ferrero, Thomas Ayral, Hartmut Hafermann, Igor Krivenko, Laura Messio, and Priyanka Seth. Triqs: A toolbox for research

on interacting quantum systems. *Computer Physics Communications*, 196:
398 – 415, 2015. ISSN 0010-4655. doi: http://doi.org/10.1016/j.cpc.2015.
04.023. URL http://www.sciencedirect.com/science/article/pii/
S0010465515001666.

[7] Priyanka Seth, Igor Krivenko, Michel Ferrero, and Olivier Parcollet.
Triqs/cthyb: A continuous-time quantum monte carlo hybridisation ex-
pansion solver for quantum impurity problems. *Computer Physics Com-
munications*, 200:274 – 284, 2016. ISSN 0010-4655. doi: http://doi.org/10.
1016/j.cpc.2015.10.023. URL http://www.sciencedirect.com/science/
article/pii/S001046551500404X.

[8] Hideo Aoki, Naoto Tsuji, Martin Eckstein, Marcus Kollar, Takashi Oka,
and Philipp Werner. Nonequilibrium dynamical mean-field theory and
its applications. *Rev. Mod. Phys.*, 86:779–837, Jun 2014. doi: 10.
1103/RevModPhys.86.779. URL https://link.aps.org/doi/10.1103/
RevModPhys.86.779.

[9] B Schmittmann and R.K.P Zia. Driven diffusive systems. an intro-
duction and recent developments. *Physics Reports*, 301(13):45 – 64,
1998. ISSN 0370-1573. doi: https://doi.org/10.1016/S0370-1573(98)
00005-2. URL http://www.sciencedirect.com/science/article/pii/
S0370157398000052.

[10] Giorgio Parisi. *Slow dynamics of glassy systems*, pages 111–121. Springer
Berlin Heidelberg, Berlin, Heidelberg, 1997. ISBN 978-3-540-69123-5. doi:
10.1007/BFb0104821. URL http://dx.doi.org/10.1007/BFb0104821.

[11] Yoshinori Tokura. Photoinduced phase transition: A tool for generating
a hidden state of matter. *Journal of the Physical Society of Japan*, 75(1):
011001, 2006. doi: 10.1143/JPSJ.75.011001. URL http://dx.doi.org/
10.1143/JPSJ.75.011001.

[12] A. L. Cavalieri, N. Muller, Th. Uphues, V. S. Yakovlev, A. Baltuska,
B. Horvath, B. Schmidt, L. Blumel, R. Holzwarth, S. Hendel, M. Drescher,

U. Kleineberg, P. M. Echenique, R. Kienberger, F. Krausz, and U. Heinzmann. Attosecond spectroscopy in condensed matter. *Nature*, 449(7165): 1029–1032, 10 2007. URL http://dx.doi.org/10.1038/nature06229.

[13] S. Wall, D. Brida, S. R. Clark, H. P. Ehrke, D. Jaksch, A. Ardavan, S. Bonora, H. Uemura, Y. Takahashi, T. Hasegawa, H. Okamoto, G. Cerullo, and A. Cavalleri. Quantum interference between charge excitation paths in a solid-state mott insulator. *Nat Phys*, 7(2):114–118, 02 2011. URL http://dx.doi.org/10.1038/nphys1831.

[14] Christian Gramsch, Karsten Balzer, Martin Eckstein, and Marcus Kollar. Hamiltonian-based impurity solver for nonequilibrium dynamical mean-field theory. *Phys. Rev. B*, 88:235106, Dec 2013. doi: 10.1103/PhysRevB. 88.235106. URL https://link.aps.org/doi/10.1103/PhysRevB.88. 235106.

[15] Immanuel Bloch, Jean Dalibard, and Wilhelm Zwerger. Many-body physics with ultracold gases. *Rev. Mod. Phys.*, 80:885–964, Jul 2008. doi: 10. 1103/RevModPhys.80.885. URL https://link.aps.org/doi/10.1103/ RevModPhys.80.885.

[16] P. W. Anderson. Localized magnetic states in metals. *Phys. Rev.*, 124: 41–53, October 1961. doi: 10.1103/PhysRev.124.41. URL https://link. aps.org/doi/10.1103/PhysRev.124.41.

[17] R. Hanson, L. P. Kouwenhoven, J. R. Petta, S. Tarucha, and L. M. K. Vandersypen. Spins in few-electron quantum dots. *Rev. Mod. Phys.*, 79: 1217–1265, Oct 2007. doi: 10.1103/RevModPhys.79.1217. URL http: //link.aps.org/doi/10.1103/RevModPhys.79.1217.

[18] R Brako and D M Newns. Theory of electronic processes in atom scattering from surfaces. *Reports on Progress in Physics*, 52(6):655, 1989. URL http: //stacks.iop.org/0034-4885/52/i=6/a=001.

[19] David C. Langreth and P. Nordlander. Derivation of a master equation for charge-transfer processes in atom-surface collisions. *Phys. Rev. B*, 43:2541–2557, Feb 1991. doi: 10.1103/PhysRevB.43.2541. URL http://link.aps.org/doi/10.1103/PhysRevB.43.2541.

[20] Antoine Georges, Gabriel Kotliar, Werner Krauth, and Marcelo J. Rozenberg. Dynamical mean-field theory of strongly correlated fermion systems and the limit of infinite dimensions. *Rev. Mod. Phys.*, 68:13–125, Jan 1996. doi: 10.1103/RevModPhys.68.13. URL https://link.aps.org/doi/10.1103/RevModPhys.68.13.

[21] Mark Jarrell and J.E. Gubernatis. Bayesian inference and the analytic continuation of imaginary-time quantum monte carlo data. *Physics Reports*, 269(3):133 – 195, 1996. ISSN 0370-1573. doi: http://dx.doi.org/10.1016/0370-1573(95)00074-7. URL http://www.sciencedirect.com/science/article/pii/0370157395000747.

[22] N F Mott and R Peierls. Discussion of the paper by de boer and verwey. *Proceedings of the Physical Society*, 49(4S):72, 1937. URL http://stacks.iop.org/0959-5309/49/i=4S/a=308.

[23] Masatoshi Imada, Atsushi Fujimori, and Yoshinori Tokura. Metal-insulator transitions. *Rev. Mod. Phys.*, 70:1039–1263, October 1998. doi: 10.1103/RevModPhys.70.1039. URL https://link.aps.org/doi/10.1103/RevModPhys.70.1039.

[24] Elbio Dagotto. Correlated electrons in high-temperature superconductors. *Rev. Mod. Phys.*, 66:763–840, July 1994. doi: 10.1103/RevModPhys.66.763. URL https://link.aps.org/doi/10.1103/RevModPhys.66.763.

[25] S. Iwai, M. Ono, A. Maeda, H. Matsuzaki, H. Kishida, H. Okamoto, and Y. Tokura. Ultrafast optical switching to a metallic state by photoinduced mott transition in a halogen-bridged nickel-chain compound. *Phys. Rev. Lett.*, 91:057401, Jul 2003. doi: 10.1103/PhysRevLett.91.057401. URL https://link.aps.org/doi/10.1103/PhysRevLett.91.057401.

[26] U. Schneider, L. Hackermüller, S. Will, Th. Best, I. Bloch, T. A. Costi, R. W. Helmes, D. Rasch, and A. Rosch. Metallic and insulating phases of repulsively interacting fermions in a 3d optical lattice. *Science*, 322(5907): 1520–1525, 2008. ISSN 0036-8075. doi: 10.1126/science.1165449. URL http://science.sciencemag.org/content/322/5907/1520.

[27] Martin C. Gutzwiller. Effect of correlation on the ferromagnetism of transition metals. *Phys. Rev. Lett.*, 10:159–162, March 1963. doi: 10. 1103/PhysRevLett.10.159. URL https://link.aps.org/doi/10.1103/PhysRevLett.10.159.

[28] Junjiro Kanamori. Electron correlation and ferromagnetism of transition metals. *Progress of Theoretical Physics*, 30(3):275, 1963. doi: 10.1143/PTP.30.275. URL http://dx.doi.org/10.1143/PTP.30.275.

[29] J. Hubbard. Electron correlations in narrow energy bands. *Proceedings of the Royal Society of London A: Mathematical, Physical and Engineering Sciences*, 276(1365):238–257, 1963. ISSN 0080-4630. doi: 10.1098/rspa. 1963.0204. URL http://rspa.royalsocietypublishing.org/content/276/1365/238.

[30] Elliott H. Lieb and F. Y. Wu. Absence of mott transition in an exact solution of the short-range, one-band model in one dimension. *Phys. Rev. Lett.*, 20:1445–1448, June 1968. doi: 10.1103/PhysRevLett.20.1445. URL https://link.aps.org/doi/10.1103/PhysRevLett.20.1445.

[31] Walter Metzner and Dieter Vollhardt. Correlated lattice fermions in $d = \infty$ dimensions. *Phys. Rev. Lett.*, 62:324–327, January 1989. doi: 10. 1103/PhysRevLett.62.324. URL https://link.aps.org/doi/10.1103/PhysRevLett.62.324.

[32] E. Müller-Hartmann. Correlated fermions on a lattice in high dimensions. *Zeitschrift für Physik B Condensed Matter*, 74(4):507–512, 1989. ISSN 1431-584X. doi: 10.1007/BF01311397. URL http://dx.doi.org/10.1007/BF01311397.

[33] G. Kotliar, S. Y. Savrasov, K. Haule, V. S. Oudovenko, O. Parcollet, and C. A. Marianetti. Electronic structure calculations with dynamical mean-field theory. *Rev. Mod. Phys.*, 78:865–951, Aug 2006. doi: 10.1103/RevModPhys.78.865. URL https://link.aps.org/doi/10.1103/RevModPhys.78.865.

[34] P. Schmidt and H. Monien. Nonequilibrium dynamical mean-field theory of a strongly correlated system. February 2002. URL https://arxiv.org/abs/cond-mat/0202046.

[35] J. K. Freericks, V. M. Turkowski, and V. Zlatić. Nonequilibrium dynamical mean-field theory. *Phys. Rev. Lett.*, 97:266408, December 2006. doi: 10.1103/PhysRevLett.97.266408. URL https://link.aps.org/doi/10.1103/PhysRevLett.97.266408.

[36] Martin Eckstein, Marcus Kollar, and Philipp Werner. Thermalization after an interaction quench in the hubbard model. *Phys. Rev. Lett.*, 103:056403, Jul 2009. doi: 10.1103/PhysRevLett.103.056403. URL https://link.aps.org/doi/10.1103/PhysRevLett.103.056403.

[37] Karsten Balzer, F. Alexander Wolf, Ian P. McCulloch, Philipp Werner, and Martin Eckstein. Nonthermal melting of néel order in the hubbard model. *Phys. Rev. X*, 5:031039, Sep 2015. doi: 10.1103/PhysRevX.5.031039. URL https://link.aps.org/doi/10.1103/PhysRevX.5.031039.

[38] L. Perfetti, P. A. Loukakos, M. Lisowski, U. Bovensiepen, H. Berger, S. Biermann, P. S. Cornaglia, A. Georges, and M. Wolf. Time evolution of the electronic structure of $1t-tas_2$ through the insulator-metal transition. *Phys. Rev. Lett.*, 97:067402, Aug 2006. doi: 10.1103/PhysRevLett.97.067402. URL https://link.aps.org/doi/10.1103/PhysRevLett.97.067402.

[39] F. Schmitt, P. S. Kirchmann, U. Bovensiepen, R. G. Moore, L. Rettig, M. Krenz, J.-H. Chu, N. Ru, L. Perfetti, D. H. Lu, M. Wolf, I. R. Fisher, and Z.-X. Shen. Transient electronic structure and melting of a charge

density wave in tbte3. *Science*, 321(5896):1649–1652, 2008. ISSN 0036-8075. doi: 10.1126/science.1160778. URL http://science.sciencemag.org/content/321/5896/1649.

[40] A. Amaricci, C. Weber, M. Capone, and G. Kotliar. Approach to a stationary state in a driven hubbard model coupled to a thermostat. *Phys. Rev. B*, 86:085110, Aug 2012. doi: 10.1103/PhysRevB.86.085110. URL https://link.aps.org/doi/10.1103/PhysRevB.86.085110.

[41] Y. Zhang and J. Callaway. Extended hubbard model in two dimensions. *Phys. Rev. B*, 39:9397–9404, May 1989. doi: 10.1103/PhysRevB.39.9397. URL https://link.aps.org/doi/10.1103/PhysRevB.39.9397.

[42] Hanna Terletska, Tianran Chen, and Emanuel Gull. Charge ordering and correlation effects in the extended hubbard model. *Phys. Rev. B*, 95:115149, Mar 2017. doi: 10.1103/PhysRevB.95.115149. URL https://link.aps.org/doi/10.1103/PhysRevB.95.115149.

[43] R Brako and D M Newns. Slowly varying time-dependent local perturbations in metals: a new approach. *Journal of Physics C: Solid State Physics*, 14(21):3065, 1981. URL http://stacks.iop.org/0022-3719/14/i=21/a=023.

[44] D. Goldhaber-Gordon, Hadas Shtrikman, D. Mahalu, David Abusch-Magder, U. Meirav, and M. A. Kastner. Kondo effect in a single-electron transistor. *Nature*, 391(6663):156–159, 01 1998. URL http://dx.doi.org/10.1038/34373.

[45] D. Goldhaber-Gordon, J. Göres, M. A. Kastner, Hadas Shtrikman, D. Mahalu, and U. Meirav. From the kondo regime to the mixed-valence regime in a single-electron transistor. *Phys. Rev. Lett.*, 81:5225–5228, Dec 1998. doi: 10.1103/PhysRevLett.81.5225. URL https://link.aps.org/doi/10.1103/PhysRevLett.81.5225.

[46] Sara M. Cronenwett, Tjerk H. Oosterkamp, and Leo P. Kouwenhoven. A tunable kondo effect in quantum dots. *Science*, 281(5376):540–544,

1998. ISSN 0036-8075. doi: 10.1126/science.281.5376.540. URL http://science.sciencemag.org/content/281/5376/540.

[47] V. Janiš and D. Vollhardt. Coupling of quantum degrees of freedom in strongly interacting disordered electron systems. *Phys. Rev. B*, 46:15712–15715, Dec 1992. doi: 10.1103/PhysRevB.46.15712. URL https://link.aps.org/doi/10.1103/PhysRevB.46.15712.

[48] Armin Comanac. Dynamical mean field theory of correlated electron systems: New algorithms and applications to local observables. *Thesis*, 2007.

[49] H. Bethe and W. Heitler. On the Stopping of Fast Particles and on the Creation of Positive Electrons. *Proceedings of the Royal Society of London Series A*, 146:83–112, August 1934. doi: 10.1098/rspa.1934.0140.

[50] Gerald D. Mahan. Many-particle physics. 2000. doi: 10.1007/978-1-4757-5714-9. URL http://www.springer.com/us/book/9780306463389.

[51] Harvey Scher and Richard Zallen. Critical density in percolation processes. *The Journal of Chemical Physics*, 53(9):3759–3761, 1970. doi: 10.1063/1.1674565. URL http://dx.doi.org/10.1063/1.1674565.

[52] D. Stauffer and A. Aharony. Introduction to percolation theory. 1994.

[53] E. Boroński and R. M. Nieminen. Electron-positron density-functional theory. *Phys. Rev. B*, 34:3820–3831, Sep 1986. doi: 10.1103/PhysRevB.34.3820. URL https://link.aps.org/doi/10.1103/PhysRevB.34.3820.

[54] M. Ostilli. Cayley trees and bethe lattices: A concise analysis for mathematicians and physicists. *Physica A: Statistical Mechanics and its Applications*, 391(12):3417 – 3423, 2012. ISSN 0378-4371. doi: https://doi.org/10.1016/j.physa.2012.01.038. URL http://www.sciencedirect.com/science/article/pii/S0378437112000647.

[55] Philipp Werner, Takashi Oka, and Andrew J. Millis. Diagrammatic monte carlo simulation of nonequilibrium systems. *Phys. Rev. B*, 79:035320, Jan

2009. doi: 10.1103/PhysRevB.79.035320. URL https://link.aps.org/doi/10.1103/PhysRevB.79.035320.

[56] G. Stefanucci and R. van Leeuwen. Nonequilibrium many-body theory of quantum systems: A modern introduction. 2013. URL https://books.google.com/books?id=6GsrjPFXLDYC.

[57] N. Grewe and H. Keiter. Diagrammatic approach to the intermediate-valence compounds. *Phys. Rev. B*, 24:4420–4444, October 1981. doi: 10.1103/PhysRevB.24.4420. URL https://link.aps.org/doi/10.1103/PhysRevB.24.4420.

[58] Martin Eckstein and Philipp Werner. Nonequilibrium dynamical mean-field calculations based on the noncrossing approximation and its generalizations. *Phys. Rev. B*, 82:115115, Sep 2010. doi: 10.1103/PhysRevB.82.115115. URL https://link.aps.org/doi/10.1103/PhysRevB.82.115115.

[59] T. Pruschke and N. Grewe. The anderson model with finite coulomb repulsion. *Z. Physik B - Condensed Matter*, 74:439, October 1989. URL https://link.springer.com/article/10.1007/BF01311391.

[60] K. Haule, S. Kirchner, J. Kroha, and P. Wölfle. Anderson impurity model at finite coulomb interaction u: Generalized noncrossing approximation. *Phys. Rev. B*, 64:155111, September 2001. doi: 10.1103/PhysRevB.64.155111. URL https://link.aps.org/doi/10.1103/PhysRevB.64.155111.

[61] Michel Caffarel and Werner Krauth. Exact diagonalization approach to correlated fermions in infinite dimensions: Mott transition and superconductivity. *Phys. Rev. Lett.*, 72:1545–1548, Mar 1994. doi: 10.1103/PhysRevLett.72.1545. URL https://link.aps.org/doi/10.1103/PhysRevLett.72.1545.

[62] Karen A. Hallberg. New trends in density matrix renormalization. *Advances in Physics*, 55(5-6):477–526, 2006. doi:

10.1080/00018730600766432. URL http://dx.doi.org/10.1080/00018730600766432.

[63] J. E. Hirsch and R. M. Fye. Monte carlo method for magnetic impurities in metals. *Phys. Rev. Lett.*, 56:2521–2524, Jun 1986. doi: 10.1103/PhysRevLett.56.2521. URL https://link.aps.org/doi/10.1103/PhysRevLett.56.2521.

[64] Emanuel Gull, Andrew J. Millis, Alexander I. Lichtenstein, Alexey N. Rubtsov, Matthias Troyer, and Philipp Werner. Continuous-time monte carlo methods for quantum impurity models. *Rev. Mod. Phys.*, 83:349–404, May 2011. doi: 10.1103/RevModPhys.83.349. URL https://link.aps.org/doi/10.1103/RevModPhys.83.349.

[65] Lothar Mühlbacher and Eran Rabani. Real-time path integral approach to nonequilibrium many-body quantum systems. *Phys. Rev. Lett.*, 100: 176403, May 2008. doi: 10.1103/PhysRevLett.100.176403. URL https://link.aps.org/doi/10.1103/PhysRevLett.100.176403.

[66] Andrey E. Antipov, Qiaoyuan Dong, and Emanuel Gull. Voltage quench dynamics of a kondo system. *Phys. Rev. Lett.*, 116:036801, Jan 2016. doi: 10.1103/PhysRevLett.116.036801. URL http://link.aps.org/doi/10.1103/PhysRevLett.116.036801.

[67] Nicholas Metropolis, Arianna W. Rosenbluth, Marshall N. Rosenbluth, Augusta H. Teller, and Edward Teller. Equation of state calculations by fast computing machines. *The Journal of Chemical Physics*, 21(6):1087–1092, 1953. doi: 10.1063/1.1699114. URL http://dx.doi.org/10.1063/1.1699114.

[68] Philipp Werner and Andrew J. Millis. Hybridization expansion impurity solver: General formulation and application to kondo lattice and two-orbital models. *Phys. Rev. B*, 74:155107, Oct 2006. doi: 10.1103/PhysRevB.74.155107. URL https://link.aps.org/doi/10.1103/PhysRevB.74.155107.

[69] W. K. Hastings. Monte carlo sampling methods using markov chains and their applications. *Biometrika*, 57(1):97–109, 1970. ISSN 00063444. URL http://www.jstor.org/stable/2334940.

[70] Yigal Meir and Ned S. Wingreen. Landauer formula for the current through an interacting electron region. *Phys. Rev. Lett.*, 68:2512–2515, Apr 1992. doi: 10.1103/PhysRevLett.68.2512. URL https://link.aps.org/doi/10.1103/PhysRevLett.68.2512.

[71] Nikolai V. Prokof'ev and Boris V. Svistunov. Polaron problem by diagrammatic quantum monte carlo. *Phys. Rev. Lett.*, 81:2514–2517, Sep 1998. doi: 10.1103/PhysRevLett.81.2514. URL https://link.aps.org/doi/10.1103/PhysRevLett.81.2514.

[72] Guy Cohen, David R. Reichman, Andrew J. Millis, and Emanuel Gull. Green's functions from real-time bold-line monte carlo. *Phys. Rev. B*, 89: 115139, Mar 2014. doi: 10.1103/PhysRevB.89.115139. URL https://link.aps.org/doi/10.1103/PhysRevB.89.115139.

[73] Guy Cohen, Emanuel Gull, David R. Reichman, and Andrew J. Millis. Green's functions from real-time bold-line monte carlo calculations: Spectral properties of the nonequilibrium anderson impurity model. *Phys. Rev. Lett.*, 112:146802, Apr 2014. doi: 10.1103/PhysRevLett.112.146802. URL https://link.aps.org/doi/10.1103/PhysRevLett.112.146802.

[74] Philipp Werner, Armin Comanac, Luca de' Medici, Matthias Troyer, and Andrew J. Millis. Continuous-time solver for quantum impurity models. *Phys. Rev. Lett.*, 97:076405, Aug 2006. doi: 10.1103/PhysRevLett.97.076405. URL https://link.aps.org/doi/10.1103/PhysRevLett.97.076405.

[75] Hiroshi Shinaoka, Yusuke Nomura, Silke Biermann, Matthias Troyer, and Philipp Werner. Negative sign problem in continuous-time quantum monte carlo: Optimal choice of single-particle basis for impurity problems. *Phys.*

Rev. B, 92:195126, Nov 2015. doi: 10.1103/PhysRevB.92.195126. URL https://link.aps.org/doi/10.1103/PhysRevB.92.195126.

[76] Jun Kondo. Resistance Minimum in Dilute Magnetic Alloys. *Prog. Theor. Phys.*, 32(1):37–49, Jul 1964. ISSN 0033-068X. doi: 10.1143/PTP.32.37. URL http://ptp.oxfordjournals.org/cgi/doi/10.1143/PTP.32.37.

[77] T A Costi, A C Hewson, and V Zlatic. Transport coefficients of the Anderson model via the numerical renormalization group. *J. Phys. Condens. Matter*, 6(13):2519–2558, Mar 1994. ISSN 0953-8984. doi: 10.1088/0953-8984/6/13/013. URL http://iopscience.iop.org/0953-8984/6/13/013http://stacks.iop.org/0953-8984/6/i=13/a=013?key=crossref.429b040641facff4e8037c3c696d6e10.

[78] R M Konik, H Saleur, and A. W. W. Ludwig. Transport through Quantum Dots: Analytic Results from Integrability. *Phys. Rev. Lett.*, 87(23):236801, Nov 2001. ISSN 0031-9007. doi: 10.1103/PhysRevLett.87.236801. URL http://link.aps.org/doi/10.1103/PhysRevLett.87.236801.

[79] V. Madhavan. Tunneling into a Single Magnetic Atom: Spectroscopic Evidence of the Kondo Resonance. *Science*, 280(5363):567–569, Apr 1998. ISSN 00368075. doi: 10.1126/science.280.5363.567. URL http://www.sciencemag.org/cgi/doi/10.1126/science.280.5363.567.

[80] Nikolaus Knorr, M Alexander Schneider, Lars Diekhöner, Peter Wahl, and Klaus Kern. Kondo Effect of Single Co Adatoms on Cu Surfaces. *Phys. Rev. Lett.*, 88(9):096804, Feb 2002. ISSN 0031-9007. doi: 10.1103/PhysRevLett.88.096804. URL http://link.aps.org/doi/10.1103/PhysRevLett.88.096804.

[81] Jiwoong Park, Abhay N Pasupathy, Jonas I Goldsmith, Connie Chang, Yuval Yaish, Jason R Petta, Marie Rinkoski, James P Sethna, Héctor D Abruña, Paul L McEuen, and Daniel C Ralph. Coulomb blockade and the Kondo effect in single-atom transistors. *Nature*, 417(6890):722–725,

Jun 2002. ISSN 0028-0836. doi: 10.1038/nature00791. URL http://www.nature.com/doifinder/10.1038/nature00791.

[82] Philipp Gegenwart, Qimiao Si, and Frank Steglich. Quantum criticality in heavy-fermion metals. *Nat. Phys.*, 4(3):186–197, Mar 2008. ISSN 1745-2473. doi: 10.1038/nphys892. URL http://dx.doi.org/10.1038/nphys892http://www.nature.com/doifinder/10.1038/nphys892.

[83] Félicien Schopfer, Christopher Bäuerle, Wilfried Rabaud, and Laurent Saminadayar. Anomalous Temperature Dependence of the Dephasing Time in Mesoscopic Kondo Wires. *Phys. Rev. Lett.*, 90(5):056801, feb 2003. ISSN 0031-9007. doi: 10.1103/PhysRevLett.90.056801. URL http://link.aps.org/doi/10.1103/PhysRevLett.90.056801.

[84] Leo Kouwenhoven and Leonid Glazman. Revival of the Kondo effect. *Phys. World*, 14(1):33–38, 2001. ISSN 09538585.

[85] S De Franceschi, R Hanson, W. G. van der Wiel, J M Elzerman, J J Wijpkema, T Fujisawa, S Tarucha, and L P Kouwenhoven. Out-of-Equilibrium Kondo Effect in a Mesoscopic Device. *Phys. Rev. Lett.*, 89(15):156801, Sep 2002. ISSN 0031-9007. doi: 10.1103/PhysRevLett.89.156801. URL http://link.aps.org/doi/10.1103/PhysRevLett.89.156801.

[86] Kenneth G. Wilson. The renormalization group: Critical phenomena and the Kondo problem. *Rev. Mod. Phys.*, 47(4):773–840, Oct 1975. ISSN 0034-6861. doi: 10.1103/RevModPhys.47.773. URL http://link.aps.org/doi/10.1103/RevModPhys.47.773.

[87] A C Hewson. *The Kondo Problem to Heavy Fermions*. Cambridge University Press, New York, N.Y., 1993.

[88] Ralf Bulla, Theo A. Costi, and Thomas Pruschke. Numerical renormalization group method for quantum impurity systems. *Rev. Mod. Phys.*, 80(2): 395–450, Apr 2008. ISSN 0034-6861. URL http://link.aps.org/doi/10.1103/RevModPhys.80.395.

[89] U. Schollwöck. The density-matrix renormalization group. *Rev. Mod. Phys.*, 77(1):259–315, Apr 2005. ISSN 0034-6861. doi: 10.1103/RevModPhys.77.259. URL http://link.aps.org/doi/10.1103/RevModPhys.77.259.

[90] A. Dirks, S. Schmitt, J. E. Han, F. Anders, P. Werner, and T. Pruschke. Double occupancy and magnetic susceptibility of the anderson impurity model out of equilibrium. *EPL (Europhysics Letters)*, 102(3):37011, 2013. URL http://stacks.iop.org/0295-5075/102/i=3/a=37011.

[91] A. Rosch, J. Paaske, J. Kroha, and P. Wlfle. The kondo effect in non-equilibrium quantum dots: Perturbative renormalization group. *Journal of the Physical Society of Japan*, 74(1):118–126, 2005. doi: 10.1143/JPSJ.74.118. URL http://dx.doi.org/10.1143/JPSJ.74.118.

[92] A. Kaminski, Yu. V. Nazarov, and L. I. Glazman. Universality of the kondo effect in a quantum dot out of equilibrium. *Phys. Rev. B*, 62:8154–8170, Sep 2000. doi: 10.1103/PhysRevB.62.8154. URL https://link.aps.org/doi/10.1103/PhysRevB.62.8154.

[93] Andrey V. Kretinin, Hadas Shtrikman, and Diana Mahalu. Universal line shape of the kondo zero-bias anomaly in a quantum dot. *Phys. Rev. B*, 85:201301, May 2012. doi: 10.1103/PhysRevB.85.201301. URL https://link.aps.org/doi/10.1103/PhysRevB.85.201301.

[94] Andrey V. Kretinin, Hadas Shtrikman, David Goldhaber-Gordon, Markus Hanl, Andreas Weichselbaum, Jan von Delft, Theo Costi, and Diana Mahalu. Spin-$\frac{1}{2}$ kondo effect in an inas nanowire quantum dot: Unitary limit, conductance scaling, and zeeman splitting. *Phys. Rev. B*, 84:245316, Dec 2011. doi: 10.1103/PhysRevB.84.245316. URL https://link.aps.org/doi/10.1103/PhysRevB.84.245316.

[95] Frank Reininghaus, Mikhail Pletyukhov, and Herbert Schoeller. Kondo model in nonequilibrium: Interplay between voltage, temperature, and crossover from weak to strong coupling. *Phys. Rev. B*, 90:085121, Aug

2014. doi: 10.1103/PhysRevB.90.085121. URL https://link.aps.org/doi/10.1103/PhysRevB.90.085121.

[96] C. Latta, F. Haupt, M. Hanl, A. Weichselbaum, M. Claassen, W. Wuester, P. Fallahi, S. Faelt, L. Glazman, J. von Delft, H. E. Tureci, and A. Imamoglu. Quantum quench of kondo correlations in optical absorption. *Nature*, 474(7353):627–630, 06 2011. URL http://dx.doi.org/10.1038/nature10204.

[97] Hakan E. Türeci, M. Hanl, M. Claassen, A. Weichselbaum, T. Hecht, B. Braunecker, A. Govorov, L. Glazman, A. Imamoglu, and J. von Delft. Many-body dynamics of exciton creation in a quantum dot by optical absorption: A quantum quench towards kondo correlations. *Phys. Rev. Lett.*, 106:107402, Mar 2011. doi: 10.1103/PhysRevLett.106.107402. URL https://link.aps.org/doi/10.1103/PhysRevLett.106.107402.

[98] G. Nunes and M. R. Freeman. Picosecond resolution in scanning tunneling microscopy. *Science*, 262(5136):1029–1032, 1993. ISSN 0036-8075. doi: 10.1126/science.262.5136.1029. URL http://science.sciencemag.org/content/262/5136/1029.

[99] Shoji Yoshida, Yuta Aizawa, Zi-han Wang, Ryuji Oshima, Yutaka Mera, Eiji Matsuyama, Haruhiro Oigawa, Osamu Takeuchi, and Hidemi Shigekawa. Probing ultrafast spin dynamics with optical pump-probe scanning tunnelling microscopy. *Nat Nano*, 9(8):588–593, 08 2014. URL http://dx.doi.org/10.1038/nnano.2014.125.

[100] Leandro Tosi, Pablo Roura-Bas, Ana María Llois, and Luis O. Manuel. Effects of vertex corrections on diagrammatic approximations applied to the study of transport through a quantum dot. *Phys. Rev. B*, 83:073301, Feb 2011. doi: 10.1103/PhysRevB.83.073301. URL https://link.aps.org/doi/10.1103/PhysRevB.83.073301.

[101] Yigal Meir, Ned S. Wingreen, and Patrick A. Lee. Low-temperature transport through a quantum dot: The anderson model out of equilibrium. *Phys.*

Rev. Lett., 70:2601–2604, Apr 1993. doi: 10.1103/PhysRevLett.70.2601. URL http://link.aps.org/doi/10.1103/PhysRevLett.70.2601.

[102] Guy Cohen, Emanuel Gull, David R. Reichman, and Andrew J. Millis. Taming the dynamical sign problem in real-time evolution of quantum many-body problems. *Phys. Rev. Lett.*, 115:266802, Dec 2015. doi: 10.1103/PhysRevLett.115.266802. URL https://link.aps.org/doi/10.1103/PhysRevLett.115.266802.

[103] Marco Schiró and Michele Fabrizio. Real-time diagrammatic monte carlo for nonequilibrium quantum transport. *Phys. Rev. B*, 79:153302, Apr 2009. doi: 10.1103/PhysRevB.79.153302. URL https://link.aps.org/doi/10.1103/PhysRevB.79.153302.

[104] Fugao Wang and D. P. Landau. Efficient, multiple-range random walk algorithm to calculate the density of states. *Phys. Rev. Lett.*, 86:2050–2053, Mar 2001. doi: 10.1103/PhysRevLett.86.2050. URL https://link.aps.org/doi/10.1103/PhysRevLett.86.2050.

[105] Fugao Wang and D. P. Landau. Determining the density of states for classical statistical models: A random walk algorithm to produce a flat histogram. *Phys. Rev. E*, 64:056101, Oct 2001. doi: 10.1103/PhysRevE.64.056101. URL https://link.aps.org/doi/10.1103/PhysRevE.64.056101.

[106] Andrey E. Antipov, Qiaoyuan Dong, Joseph Kleinhenz, Guy Cohen, and Emanuel Gull. Currents and green's functions of impurities out of equilibrium: Results from inchworm quantum monte carlo. *Phys. Rev. B*, 95:085144, Feb 2017. doi: 10.1103/PhysRevB.95.085144. URL https://link.aps.org/doi/10.1103/PhysRevB.95.085144.

[107] Matthias Troyer, Stefan Wessel, and Fabien Alet. Flat histogram methods for quantum systems: Algorithms to overcome tunneling problems and calculate the free energy. *Phys. Rev. Lett.*, 90:120201, Mar 2003. doi:

10.1103/PhysRevLett.90.120201. URL https://link.aps.org/doi/10.1103/PhysRevLett.90.120201.

[108] Gang Li, Werner Hanke, Alexei N. Rubtsov, Sebastian Bäse, and Michael Potthoff. Accessing thermodynamics from dynamical cluster-embedding approaches. *Phys. Rev. B*, 80:195118, Nov 2009. doi: 10.1103/PhysRevB.80.195118. URL https://link.aps.org/doi/10.1103/PhysRevB.80.195118.

[109] Sergei Iskakov, Andrey E. Antipov, and Emanuel Gull. Diagrammatic monte carlo for dual fermions. *Phys. Rev. B*, 94:035102, Jul 2016. doi: 10.1103/PhysRevB.94.035102. URL http://link.aps.org/doi/10.1103/PhysRevB.94.035102.

[110] Frithjof B. Anders. Steady-state currents through nanodevices: A scattering-states numerical renormalization-group approach to open quantum systems. *Phys. Rev. Lett.*, 101:066804, Aug 2008. doi: 10.1103/PhysRevLett.101.066804. URL https://link.aps.org/doi/10.1103/PhysRevLett.101.066804.

[111] Philipp Werner, Naoto Tsuji, and Martin Eckstein. Nonthermal symmetry-broken states in the strongly interacting hubbard model. *Phys. Rev. B*, 86:205101, Nov 2012. doi: 10.1103/PhysRevB.86.205101. URL https://link.aps.org/doi/10.1103/PhysRevB.86.205101.

[112] N. F. Mott. Metal-insulator transitions. 1990.

[113] P. Limelette, A. Georges, D. Jérome, P. Wzietek, P. Metcalf, and J. M. Honig. Universality and critical behavior at the mott transition. *Science*, 302(5642):89–92, 2003. ISSN 0036-8075. doi: 10.1126/science.1088386. URL http://science.sciencemag.org/content/302/5642/89.

[114] P. Limelette, P. Wzietek, S. Florens, A. Georges, T. A. Costi, C. Pasquier, D. Jérome, C. Mézière, and P. Batail. Mott transition and transport crossovers in the organic compound $\kappa-(\mathrm{BEDT-TTF})_2\mathrm{Cu[N(CN)}_2]\mathrm{Cl}$.

Phys. Rev. Lett., 91:016401, Jul 2003. doi: 10.1103/PhysRevLett.91.
016401. URL https://link.aps.org/doi/10.1103/PhysRevLett.91.
016401.

[115] H. Terletska, J. Vučičević, D. Tanasković, and V. Dobrosavljević. Quantum
critical transport near the mott transition. *Phys. Rev. Lett.*, 107:026401,
Jul 2011. doi: 10.1103/PhysRevLett.107.026401. URL https://link.
aps.org/doi/10.1103/PhysRevLett.107.026401.

[116] Ronald W. Schafer. Alan V. Oppenheim. Discrete-time signal processing,
third edition . 2010. URL https://www.pearsonhighered.com/program/
Oppenheim-Discrete-Time-Signal-Processing-3rd-Edition/
PGM212808.html.

[117] Anatoli Polkovnikov, Krishnendu Sengupta, Alessandro Silva, and Mukund
Vengalattore. Colloquium. *Rev. Mod. Phys.*, 83:863–883, Aug 2011. doi: 10.
1103/RevModPhys.83.863. URL https://link.aps.org/doi/10.1103/
RevModPhys.83.863.

[118] B. Moritz, A. F. Kemper, M. Sentef, T. P. Devereaux, and J. K. Freer-
icks. Electron-mediated relaxation following ultrafast pumping of strongly
correlated materials: Model evidence of a correlation-tuned crossover be-
tween thermal and nonthermal states. *Phys. Rev. Lett.*, 111:077401, Aug
2013. doi: 10.1103/PhysRevLett.111.077401. URL https://link.aps.
org/doi/10.1103/PhysRevLett.111.077401.